

THE FLORIDA STATE UNIVERSITY
COLLEGE OF ARTS AND SCIENCE

MULTI-GPU SOLUTIONS OF GEOPHYSICAL PDES WITH RADIAL BASIS
FUNCTION-GENERATED FINITE DIFFERENCES

By

EVAN F. BOLLIG

A Dissertation submitted to the
Department of Scientific Computing
in partial fulfillment of the
requirements for the degree of
Doctor of Philosophy

Degree Awarded:
Fall Semester, 2012

Evan F. Bollig defended this dissertation on October 1, 2012.

The members of the supervisory committee were:

Gordon Erlebacher
Professor Directing Thesis

Natasha Flyer
Outside University Representative

Mark Sussman
University Representative

Dennis Slice
Committee Member

Ming Ye
Committee Member

Janet Peterson
Committee Member

The Graduate School has verified and approved the above-named committee members, and certifies that the dissertation has been approved in accordance with the university requirements.

To the one who taught me patience, compassion, and determination. Thank you, mom.

-E

ACKNOWLEDGMENTS

Thank you to my committee.

Drs. David Yuen, Bengt Fornberg, Kiran Katta, Geoff Womeldorf

The students and faculty in DSC.

Special thanks to the DSC Staff.

Thanks as well to the entire team at MSI for computational resources

This research was funded by awards:

TABLE OF CONTENTS

List of Tables	vii
List of Figures	viii
Abstract	xii
1 Introduction	1
1.1 On Parallel/Distributed RBF-FD	4
1.2 On GPU RBF Methods	5
1.3 On Multi-GPU Methods	7
 I Preliminaries	 8
2 RBF Methods for PDEs	9
2.1 Survey of Related Work	10
2.1.1 Global RBF Methods	13
2.1.2 Compactly Support RBFs	15
2.1.3 Local RBF Methods	16
2.2 Comparison of RBF Methods	16
2.2.1 RBF Scattered Data Interpolation	17
2.2.2 Reconstructing Solutions for PDEs	18
2.2.3 PDE Methods	19
2.2.4 Local Methods	22
2.3 Recent Advances in Conditioning	23
 II RBF-FD for HPC Environments	 25
3 Introduction to RBF-FD	26
3.1 Multiple Operators	29
3.2 Differentiation Matrices and Sparse Matrix-Vector Multiply (SpMV)	29
3.3 Weight Operators	31
3.3.1 First and Second Derivatives ($\frac{1}{r} \frac{\partial \phi}{\partial r}, \frac{\partial^2 \phi}{\partial r^2}$)	32
3.3.2 Cartesian Gradient (∇)	32
3.3.3 Cartesian Laplacian (∇^2)	32
3.3.4 Laplace-Beltrami (Δ_S) on the Sphere	33

3.3.5	Constrained Gradient ($P_x \cdot \nabla$) on the Sphere	33
3.3.6	Hyperviscosity Δ^k for Stabilization	34
3.4	RBF-FD Implementation for Time-dependent PDEs	35
3.5	Grids	36
3.6	On Choosing the Right ϵ	39
4	An Alternative Stencil Generation Algorithm for RBF-FD	42
4.1	k -D Tree	43
4.2	A Fixed-Grid Algorithm	46
4.2.1	Fixed-grid Construction	48
4.2.2	Fixed-Grid k -NN	50
4.2.3	Orderings	51
4.2.4	Performance	51
4.2.5	Integer Dilation and Node Reordering	53
4.3	Performance Comparison	53
4.3.1	Future Work	54
4.3.2	Hashing	54
4.4	On Space Filling Curves and Other Orderings	60
4.4.1	Integer Dilation	60
4.5	Conclusions on Stencil Generation	61
5	Numerical Validation	62
5.0.1	Vortex Rollup	62
5.0.2	Solid body rotation	64
5.1	Fragments (integrate above)	68
5.1.1	CFL	69
	Biographical Sketch	79

LIST OF TABLES

2.1	Examples of frequently used RBFs based on [26, 43]. ε is the support parameter. All RBFs have global support. For compact support, enforce a cut-off radius (see Equation 2.1).	11
2.2	RBF interpolation types and properties, assuming a problem with N nodes.	13
2.3	Classification of references based on choice of RBF interpolation types and method for solving PDEs. References may appear in multiple cells according to the breadth of their research.	15
5.1	Values for hyperviscosity and the RBF shape parameter ϵ for vortex roll-up test. .	64
5.2	Values for hyperviscosity and RBF shape parameter for the cosine bell test.	66

LIST OF FIGURES

1.1	Commonly Used Radial Basis Functions (RBFs)	2
2.1	Example RBF shapes from Table 2.1 with parameter $\varepsilon = 1$	11
2.2	The Gaussian (GA) RBF (Table 2.1) with parameter $\varepsilon = 1$ and r in $D = 1, 2$ and 3	12
2.3	RBF interpolation using 15 translates of the Gaussian RBF with $\epsilon = 2$. One RBF is centered at each node in the domain. Linear combinations of these produce an interpolant over the domain passing through known function values.	12
3.1	Examples of stencils computable with RBF-FD	27
3.2	Differentiation matrix D_x is applied explicitly to calculate derivative approximations, $\frac{d}{dx}u(x)$	30
3.3	Quasi-regular nodes with $N = 4096$ maximum determinant (MD) node sets on the unit sphere.	38
3.4	$N = 2562$ icosahedral nodes on the unit sphere.	38
3.5	(Left) $N=100,000$ Spherical Centroidal Voronoi Tessellation nodes. (Right) Close-up of the same $N=100,000$ nodes to illustrate the irregularities in the grid.	39
3.6	Contours for ϵ as a function of \sqrt{N} for stencil sizes $n = 20, 40, 60, 80$ and 100 on the unit sphere. Contours assume near uniform distribution of nodes (e.g., maximum determinant (MD) nodes). Parameters superimposed above each contour provide coefficients for function $\epsilon(\sqrt{N}) = c_1\sqrt{N} - c_2$.	41
4.1	A stencil center in green finds neighboring stencil nodes in blue. Two ball queries are shown as dashed and dash-dot circles to demonstrate the added difficulty of finding the right query radius to obtain the k -nearest neighbors.	43
4.2	An example k -D Tree in 2-Dimensions. Nodes are partitioned with a cyclic dimension splitting rule (i.e., splits occur first in X , then Y , then X , etc.); all splits occur at the median node in each dimension.	45

4.3	Two example space filling curves to linearize the same fixed-grid. Left: Raster-ordering (ijk); Right: Morton-/Z-ordering.	48
4.4	Example effects of node reordering for MD node set $N = 6400$ with $n = 50$. The differentiation matrices are permuted equivalents and roughly 0.78% full. a) Stencils generated based on k -D Tree maintain the original node ordering. b) The reordered node set generated using an $h_n = 10$ fixed-grid condenses non-zeros for improved cache effects.	50
4.5	A stencil generated with k -ANN satisfies the required stencil size, but is not guaranteed to choose the true nearest neighbors.	52
4.6	In order: a) node ordering test cases; b) original ordering of regular grid (raster); c) coarse grid overlay for hash functions ($hnx = 6$); d) example stencil ($n = 31$) spanning multiple Z's; e) spy of DM after orderings. Author's Note: <u>REGENERATE FIGURES WITH RANDOM/HALTON NODES</u>	55
4.7	In order: a) node ordering test cases; b) original ordering of regular grid (raster); c) coarse grid overlay for hash functions ($hnx = 6$); d) example stencil ($n = 31$) spanning multiple Z's; e) spy of DM after orderings.	56
4.8	Querying the $n = 50$ nearest neighbors on a regular grid up to $N = 160^3$ demonstrates the significant gains achieved by our spatially binned neighbor query. While KDTree queries grow as $O(N \log N)$	56
4.9	Querying the $n = 50$ nearest neighbors on a regular grid up to $N = 160^3$ demonstrates the significant gains achieved by our spatially binned neighbor query. While KDTree queries grow as $O(N \log N)$	57
4.10	Querying the $n = 50$ nearest neighbors on a regular grid up to $N = 160^3$ demonstrates the significant gains achieved by our spatially binned neighbor query. While KDTree queries grow as $O(N \log N)$	58
4.11	Generating stencils for increasing subsets of the $N = 1e6$ CVT nodes mesh.	58
4.12	Based on the proper choice of overlay resolution, the hash stencil query can accelerate stencil generation, but the sophistication of the algorithm is low enough that negative impact is more likely. On the other hand, the impact on SpMV performance is always positive with the routine accelerated up to 4.9x faster.	59
4.13	As the coarse grid resolution increases the hashing algorithm achieves both 2x faster than KDTree in stencil generation, with greater than 4x gain in SpMV performance (for free).	59

4.14	In order: a) node ordering test cases; b) original ordering of regular grid (raster); c) coarse grid overlay for hash functions ($hnx = 6$); d) example stencil ($n = 31$) spanning multiple Z's; e) spy of DM after orderings. Author's Note: <u>TODO: Raster on top left. Add RCM ordering to top right.</u>	61
5.1	Eigenvalues of $\text{diag}(\omega(\theta))D_\lambda$ for the vortex roll-up test case for $N = 4096$ nodes, stencil size $n = 101$ and $\epsilon = 3.5$. Left: no hyperviscosity. Right: hyperviscosity enabled with $k = 4$ and $\gamma_c = 40$. Author's Note: <u>color</u>	64
5.2	Vortex roll-up solution at time $t = 10$ using RBF-FD with $N = 10, 201$ and $n = 50$ point stencil. Normalized ℓ_2 error of solution at $t = 10$ is $1.25(10^{-2})$. Author's Note: <u>add initial condition figure</u>	65
5.3	Convergence plot for vortex roll-up at $t = 3$. Author's Note: <u>color</u>	65
5.4	Eigenvalues of (5.4) for the cosine bell test case with $N = 4096$ nodes, stencil size $n = 101$, and $\epsilon = 3.5$. Left: no hyperviscosity. Right: hyperviscosity enabled with $k = 8$ and $\gamma_c = 5 * 10^{-2}$. Eigenvalues are divided by u_0 to remove scaling effects of velocity. Author's Note: <u>color</u>	67
5.5	Cosine bell solution after 10 revolutions with $N = 10201$ nodes and stencil size $n = 101$. Hyperviscosity parameters are $k = 8$, $\gamma_c = 5(10^{-2})$. Author's Note: <u>Insert color figures</u>	67
5.6	Convergence plot for cosine bell advection. Normalized ℓ_2 error at 10 revolutions with hyperviscosity enabled.	68

LIST OF ALGORITHMS

3.1	A High-Level View of RBF-FD	36
4.1	BuildKDTree(P , $depth$)	44
4.2	KNNSearchKDTree(X_q , n , $root$, $depth$)	46
4.3	BuildFixedGrid(P , h_n)	49
4.4	QueryFixedGrid(X_q , n , P , Q)	51

ABSTRACT

Many numerical methods based on Radial Basis Functions (RBFs) are gaining popularity in the geosciences due to their competitive accuracy, functionality on unstructured meshes, and natural extension into higher dimensions. One method in particular, the Radial Basis Function-generated Finite Differences (RBF-FD), has drawn significant attention due to its comparatively low computational complexity versus other RBF methods, high-order accuracy (6th to 10th order is common), and parallel nature.

Similar to classical Finite Differences (FD), RBF-FD computes weighted differences of stencil node values to approximate derivatives at stencil centers. The method differs from classical FD in that the test functions used to calculate the differentiation weights are n -dimensional RBFs rather than one-dimensional polynomials. This allows for generalization to n -dimensional space on completely scattered node layouts.

Although RBF-FD was first proposed nearly a decade ago, it is only now gaining a critical mass to compete against well known competitors in modeling like FD, Finite Volume and Finite Element. To truly contend, RBF-FD must transition from single threaded MATLAB environments to large-scale parallel architectures.

Many HPC systems around the world have made the transition to Graphics Processing Unit (GPU) accelerators as a solution for added parallelism and higher throughput. Some systems offer significantly more GPUs than CPUs. As the problem size, N , grows larger, it behooves us to work on parallel architectures, be it CPUs or GPUs. In addition to demonstrating the ability to scale to hundreds or thousands of compute nodes, this work introduces parallelization strategies that span RBF-FD across multi-GPU clusters. The stability and accuracy of the parallel implementations are tested in explicit and implicit modes to verify correctness.

This work establishes RBF-FD as a contender in the arena of distributed HPC numerical methods.

CHAPTER 1

INTRODUCTION

Many scientific problems of importance can be expressed as a collection of partial differential equations defined for some domain. In order to solve these problems, computational numerical methods are employed on a discretized version of the domain. Traditionally, numerical methods have been *meshed methods*, in that they rely on some underlying grid/lattice to connect discretized points in a well-defined manner. More recently a new class of methods surfaced, called *meshfree methods*, which discard the requirement for connectivity information and operate only on point clouds. Each class of methods offers numerous and often complementary benefits. This work focuses on a recent method that draws inspiration from both meshed and meshfree methods, called *Radial Basis Function-generated Finite Differences (RBF-FD)*.

Author's Note: [this paragraph does not fit well](#) The first task in traditional meshed methods is to generate an underlying grid/mesh. Node placement can be done in a variety of ways including uniform, non-uniform and random (monte carlo) sampling, or through iterative methods like Lloyd's algorithm that generate a regularized sampling of the domain (see e.g., [22]). In addition to choosing nodes, meshed methods require connectivity/adjacency lists to form stencils (e.g., Finite Differences) or elements (e.g., Finite Element Method).

Well balanced meshes play a significant role in isolating nodes and allowing methods to be partitioned for distributed computing.

this implies an added challenge to cover the domain closure with a chosen element type. While these tasks may be straightforward in one- or two-dimensions, the extension into higher dimensions becomes increasingly more cumbersome [60]. Also, it is often the case that methods have limited support for irregular node distributions (e.g., FD)

Ideally, we seek a method defined on arbitrary geometries, that behaves regularly in any dimension, and avoids the cost of mesh generation. The ability to locally refine areas of interest in a practical fashion is also desirable. Fortunately, meshfree methods provide all of these properties: based wholly on a set of independent points in n -dimensional space, there is minimal cost for mesh generation, and refinement is as simple as adding new points where they are needed.

Since their adoption by the mathematics community in the 1980s ([26]), a plethora of meshfree methods have arisen for the solution of partial differential equations (PDEs). For example, smoothed particle hydrodynamics, partition of unity method, element-free Galerkin method and others have been considered for fluid flow problems [12]. A good

survey of meshfree methods can be found in [60].

A subset of meshfree methods of particular interest to the numerical modeling community today revolves around Radial Basis Functions (RBFs). RBFs are a class of radially symmetric functions (i.e., symmetric about a point, x_j , called the *center*) of the form:

$$\phi_j(\mathbf{x}) = \phi(r(\mathbf{x})) \quad (1.1)$$

where the value of the univariate function ϕ is a function of the Euclidean distance from the center point \mathbf{x}_j given by $r(\mathbf{x}) = \|\mathbf{x} - \mathbf{x}_j\|_2 = \sqrt{(x - x_j)^2 + (y - y_j)^2 + (z - z_j)^2}$. Examples of commonly used RBFs are shown in Figure 1.1 (for corresponding equations refer to Table 2.1). RBF methods are based on a superposition of translates of these radially symmetric functions, providing a linearly independent but non-orthogonal basis used to interpolate between nodes in n -dimensional space.

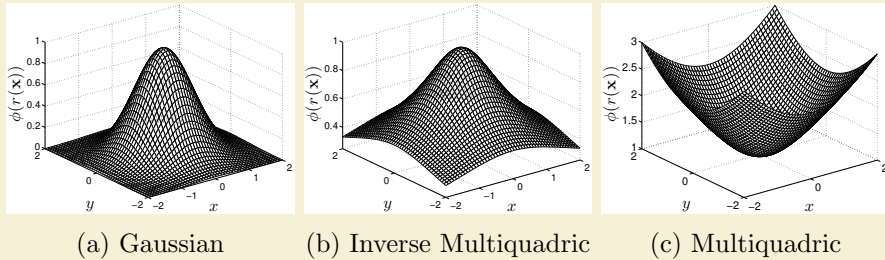


Figure 1.1: Commonly Used Radial Basis Functions (RBFs).

To track the history of RBF methods, one must look back to 1971 and R.L. Hardy’s seminal research on interpolation with multi-quadric basis functions [49]. Solving PDEs with RBFs dates back to 1990 [55, 56]. At the core of all RBF-based PDE methods lies the fundamental problem of approximation/interpolation. Some methods (e.g., global- and compact-RBF methods) apply RBFs to approximate derivatives directly. Others (e.g., RBF-generated Finite Differences) leverage the basis functions to generate stencil weights for finite-difference approximations of derivatives.

As “meshless” methods, RBF methods excel at solving problems that require geometric flexibility with scattered node layouts in d -dimensional space. They naturally extend into higher dimensions without significant increase in programming complexity [32, 100]. In addition to competitive accuracy and convergence compared with other state-of-the-art methods [29, 30, 32, 33, 100], they also boast stability for large time steps.

While most of the literature surrounding RBFs for PDEs involves collocation (see Chapter 2), trends have shifted to place RBF-FD top of the list in the community today. RBF-FD is a hybrid of RBF scattered data interpolation and classical Finite Difference (FD). It shares many of the benefits from other RBF methods, like the ability to handle scattered node layouts in any dimension, as well as high-order accurate solutions. Likewise, RBF-FD exhibits many benefits akin to classical FD including compact stencils for localized derivative approximation, and low computational complexity.

The idea behind classical FD is to express derivatives at a single node (center) as a weighted combination/difference of solution values from a small neighborhood (i.e., a stencil) around the center. Common approximations such as upwind differencing, center differ-

encing, and other higher order approximations are of this form. In similar fashion, RBF-FD combines solutions values based on stencils, but it does so in a more generalized sense than standard FD. For example, classical FD is typically restricted to regular meshes and often symmetric stencils in practice with the same set of weights for each stencil. Weights can be derived from polynomial expansion and obtained in 1D by solving a Vandermonde interpolation matrix [39]. Higher dimension FD stencils are composed from combinations of 1D formulas applied to each dimension. This implies restrictions on the shape/layout of stencils. In contrast to this, RBF-FD is designed for stencils with irregular node placement and can easily provide a unique set of weights for each stencil with no restrictions on stencil shape.

The concept of RBF-FD was first introduced in 2000 [88], but it took another few years for the method to really get a start ([78], [87], [99] and [11]). Introduced over a decade ago, the method is only recently showing signs that it has obtained the critical-mass following necessary for the method's use in large-scale scientific models. At the onset of this work, most of the literature considered RBF-FD for problem sizes up to a few thousand nodes; at most tens of thousands of nodes. Similar to most RBF methods, RBF-FD is predominantly implemented within small-scale, serial computing environments. Under most circumstances the community at large continues investigation and extension development within MATLAB.

The goal of this dissertation is to scale RBF-FD solutions on high resolution meshes across high performance clusters, and to lead the way for its adoption within HPC and supercomputing circles. Chapter ?? focuses on the problem of distributing RBF-FD across independent compute nodes, and demonstrates the scalability of RBF-FD on over a thousand processors. As part of the push to HPC, leveraging Graphics Processing Units (GPUs) for computation is considered critical. GPUs, introduced in Chapter ??, are many-core accelerators capable of general purpose, embarrassingly parallel computations. Accelerators represent the latest trend in HPC, where compute nodes are commonly supplemented by one or more accessory boards for offload parallel tasks. Chapter ?? continues the discussion of RBF-FD on GPUs by tackling the problem of spanning a GPU cluster with an algorithm for overlapping communication and computation to hide the latency in data transfer between accelerators. Our effort leads the way for RBF-FD applicationss in an age when compute nodes with attached accelerator boards are considered key to breaching the exascale computing barrier [4].

The layout of this document is as follows. This chapter continues with a survey of work related on parallelizing RBF-FD, targeting the GPU, and spanning a multi-GPU cluster. Chapter 2 provides a historical survey of RBF methods as a backdrop to present RBF-FD in Chapter 3. Chapter 4 introduces a novel, fast algorithm for generating RBF-FD stencils as a faster alternative to the k -D Tree algorithm widely in use by the RBF community. In Chapter ??, the first scalable implementation of RBF-FD to span one thousand processors is described in detail. Chapter ?? continues with the challenge of offloading computation to GPUs, and Chapter ?? expands the discussion to a multi-GPU cluster. Chapter ?? verifies the parallel RBF-FD implementation with both explicit and implicit solutions to geophysical problems. Finally, this document concludes with a summary of results and discussion of future directions in Chapter ??.

Author's Note: [TODO: iterate through remainder of this chapter again](#)

1.1 On Parallel/Distributed RBF-FD

Parallel implementations of RBF methods rely on domain decomposition. Depending on the implementation, domain decomposition not only accelerates solution procedures, but can decrease the ill-conditioning that plague all global RBF methods [21]. The ill-conditioning is reduced if each domain is treated as a separate RBF domain, and the boundary update is treated separately. Domain decomposition methods for RBFs were introduced by Beatson et al. [5] in the year 2000 as a way to increase problem sizes into the millions of nodes.

This work leverages a domain decomposition, but not for the purpose of conditioning. Instead the focus is on decomposing the domain in order to scale RBF-FD across more than a thousand CPU cores of an HPC cluster. Add to this the twist of incorporating a novel implementation on the GPU with overlapping communication and computation. This combination is unmatched in related work. However, RBF methods do have a bit of history of parallel implementations.

In 2007, Divo and Kassab [21] used a domain decomposition method with artificial sub-domain boundaries for their implementation of a local collocation method [21]. The sub-domains are processed independently, with derivative values at artificial boundary points averaged to maintain global consistency of physical values. Their implementation was designed for a 36 node cluster, but benchmarks and scalability tests are not provided.

However, research on the parallelization of RBF algorithms to solve PDEs on multiple CPU/GPU architectures is essentially non-existent. We have found three studies that have addressed this topic, none of which implement RBF-FD but rather take the avenue of domain decomposition for global RBFs (similar to a spectral element approach). In [21], Divo and Kassab introduce subdomains with artificial boundaries that are processed independently. Their implementation was designed for a 36 node cluster, but benchmarks and scalability tests are not provided. Kosec and Šarler [57] parallelize coupled heat transfer and fluid flow models using OpenMP on a single workstation with one dual-core processor. They achieved a speedup factor of 1.85x over serial execution, although there were no results from scaling tests. Yokota, Barba and Knepley [105] apply a restrictive additive Schwarz domain decomposition to parallelize global RBF interpolation of more than 50 million nodes on 1024 CPU processors.

Kosec and Šarler [57] have the only known (to our knowledge) OpenMP implementation for RBFs. The authors parallelize coupled heat transfer and fluid flow problems on a single workstation. The application involves the local RBF collocation method, explicit time-stepping and Neumann boundary conditions. A speedup factor of 1.85x over serial execution was achieved by executing on two CPU cores; no further results from scaling tests were provided.

Stevens et al. [84] mention a parallel implementation under development, but no document is available at this time.

Perhaps the most competitive parallel implementation of RBFs is the PetRBF [105] branch of PETSc [?]. The authors of PetRBF (also developers for PETSc) have implemented a highly scalable, efficient RBF interpolation method based on compact RBFs (i.e., they operate on sparse matrices). The authors demonstrate efficient weak scaling of PetRBF across 1024 processes on a Blue Gene/L, and strong scaling up to 128 processes

on the same hardware. Additionally, strong scaling was tested on a Cray XT4. On the Blue Gene/L, PetRBF is demonstrated to achieve an impressive 74% parallel weak scaling efficiency on 1024 processes (operating on over 50 million points), and 84% strong scaling efficiency for 128 processes. For the Cray XT4, strong scaling tops out at 36% for 128 processes, a respectable number—and similar to observed results for our own code on 128 processes.

Parallelization of RBF-FD is achieved at two levels. First, the physical domain of the problem is partitioned into overlapping subdomains, each handled by a different MPI process. All CPUs operate independently to compute/load RBF-FD stencil weights, run diagnostic tests and perform other initialization tasks. A CPU computes only weights corresponding to stencils centered in the interior of its partition. After initialization, CPUs continue concurrently to solve the PDE. Communication barriers ensure that the CPUs execute in lockstep to maintain consistent solution values in regions where partitions overlap. The second level of parallelization offloads time-stepping of the PDE to the GPU. Evaluation of the right hand side of Equation (3.14) is data-parallel: the solution derivative at each stencil center is evaluated independently of the other stencils. This maps well to the GPU, offering decent speedup even in unoptimized kernels. Although the stencil weight calculation is also data-parallel, we assume that in this context that the weights are precomputed and loaded once from disk during the initialization phase.

1.2 On GPU RBF Methods

With regard to the latter, there is some research on leveraging RBFs on GPUs in the fields of visualization [17, 92], surface reconstruction [10, 16], and neural networks [8].

Only Schmidt et al. [77] have accelerated a global RBF method for PDEs on the GPU. Their MATLAB implementation applies global RBFs to solve the linearized shallow water equations utilizing the AccelerEyes Jacket [2] library to target a single GPU.

GPUs were introduced in 80's see master's thesis.

Originally GPUs were designed as parallel rasterizing units. They had limited logic control in contrast to the serial CPUs and their advanced branching and looping logic.

Gradually new and complex logic was added to the GPU to produce the shader languages that allowed developers to customize specific parts of the rendering pipeline. This allowed scientific problems such as the diffusion equation cite Lore and others to be solved in process of rendering. In other words, the GPU was tricked into computing.

The year 2006 brought the modern age of GPU computing with the introduction of CUDA from NVidia. The high level language allowed scientists to leverage the GPU as a parallel accelerator without all of the overhead of setting up graphics contexts and tricking the hardware into computing. Memory management is still the developer's responsibility, but compiler transforms generic C/Fortran code to GPU instruction set.

Scientific Computing has seen a widespread adoption of GPGPU because of the goal to get to "exa-scale" computing, which may only be possible in the near future with the help of GPU accelerators [4].

NVidia is not the only company involved in many core parallel accelerators. Other groups like AMD and Intel have been increasing the number of cores as well. The end effect

is a hybridization where CPUs look similar to GPUs and vice-versa.

Until 2009, the hardware distinction required that developers target parallelism on CPUs and GPUs using different languages. Then the OpenCL standard was drafted and implemented. OpenCL is a parallel language that strives to provide functional portability rather than performance.

We focus on the OpenCL language within this dissertation with confidence that hardware will change frequently. In fact, every 18 months [cite](#) shows a new release of GPU hardware, manycore CPU hardware and extensions to parallel languages. But if hardware is constantly changing, then we need to focus on a high level implementation that allows portability. We need a language like OpenCL to carry our implementations into the future regardless of what hardware and which company survive.

Related work on RBFs and GPUs is sparse. In 2009, Schmidt et al. [76, 77] implemented a global RBF method for Tsunami simulation on the GPU using the AccelerEyes Jacket [2] add-on for MATLAB. Jacket provides a MATLAB interface to data structures and routines that internally call to the NVidia CUDA API. Their model was based on a single large dense matrix solve, and with the help of Jacket the authors were able to achieve approximately 7x speedup over the standard MATLAB solution on the then current generation of the MacBook Pro laptop. The authors compared the laptop CPU (processor details not specified) to the built-in NVidia GeForce 8600M GT GPU. Schmidt et al.’s implementation was the first contribution to the RBF community to leverage accelerators. The results were significant and promising, but no further contributions were made on the topic.

While both Schmidt et al.’s method and the method presented here are based on RBFs, the two problems are only distantly related when it comes to implementation on the GPU. Dense matrix operations have a high computational complexity, are considered ideal (or near to) by linear algebra libraries like BLAS [?] and LAPACK [3], and were demonstrated to fit well on GPUs from the onset of General Purpose GPU (GPGPU) Computing. In fact, NVidia included CUBLAS [?] (a GPU based BLAS library for their hardware) with their initial public release of the game-changing CUDA development kit in 2006. In stark contrast to this, sparse matrix operations have minimal computational complexity and are less than ideal for the GPU.

Earlier this year (2013), Cuomo et al. [18] implemented RBF-interpolation on the GPU for surface reconstruction. Their implementation utilizes PetRBF [105], and new built-in extensions that allow GPU access within PETSc. PETSc internally wraps the CUSP project [?] for sparse matrix algebra on the GPU. With the help of these libraries, Cuomo et al. solve and apply sparse interpolation systems on the GPU for up to three million nodes on an NVidia Fermi C1060 GPU (4GB). They compare results to a single core CPU implementation on an Intel i7-940 CPU and demonstrate that the GPU accelerate their solutions between 6x and 25x. Unfortunately, the authors do not show evidence of scaling the interpolation across multiple GPUs; so while evidence exists that PetRBF now has full GPU support, it remains to be seen how well the code can scale in GPU mode.

1.3 On Multi-GPU Methods

Multi-GPU Jacobi iteration for Navier stokes flow in cavity [http://scholarworks.
boisestate.edu/cgi/viewcontent.cgi?article=1003&context=mecheng_facpubs](http://scholarworks.boisestate.edu/cgi/viewcontent.cgi?article=1003&context=mecheng_facpubs)
Thibault et al. have multiple works on Multi-GPU and overlapping comm and comp.

Part I

Preliminaries

CHAPTER 2

RBF METHODS FOR PDES

The process of solving partial differential equations (PDEs) using radial basis functions (RBFs) dates back to 1990 [55, 56]. However, at the core of all RBF methods lies the fundamental problem of approximation/interpolation. Some methods (e.g., global- and compact-RBF methods) apply RBFs to approximate derivatives directly. Others (e.g., RBF-generated Finite Differences) leverage the basis functions to generate weights for finite-differencing stencils, utilizing the weights in turn to approximate derivatives. Regardless, to track the history of RBF methods, one must look back to 1971 and R.L. Hardy’s seminal research on interpolation with multi-quadric basis functions [49].

As “meshless” methods, RBF methods excel at solving problems that require geometric flexibility with scattered node layouts in d -dimensional space. They naturally extend into higher dimensions without significant increase in programming complexity [32, 100]. In addition to competitive accuracy and convergence compared with other state-of-the-art methods [29, 30, 32, 33, 100], they also boast stability for large time steps.

This chapter is dedicated to summarizing the four-decade history of RBF methods leading up to the development of the RBF-generated Finite Differences (RBF-FD) method. Beginning with a brief introduction to RBFs and a historical survey, related methods are into classified into three types: global, compact, and local methods. Following this, the general approximation problem is introduced, with a look at the core of all three method classifications: RBF scattered-data interpolation.

Like most numerical methods, RBFs come with certain limitations. For example, RBF interpolation is—in general—not a well-posed problem, so it requires careful choice of positive definite or conditionally positive definite basis functions [26, 52]. The example 2D RBFs presented in Figure 1.1 are infinitely smooth and satisfy the (conditional) positive definite requirements.

Infinitely smooth RBFs depend on a shape or support parameter ϵ that controls the width of the function. The functional form of the shape function becomes $\phi(\epsilon r)$. Decreasing ϵ increases the support of the RBF and in most cases, the accuracy of the interpolation, but worsens the conditioning of the RBF interpolation problem [75]. The conditioning of the system also dramatically degrades as the number of nodes in the problem increases. Fortunately, recent algorithms such as Contour-Padé [36] and RBF-QR [38, 42] allow for numerically stable computation of interpolants in the nearly flat RBF regime (i.e., $\epsilon \rightarrow 0$) where high accuracy has been observed [43, 59].

Historically, the most common way to leverage RBFs for PDE solutions is in a global interpolation sense. That is, the value of a function value or any of its derivatives at a node location is a linear combination of all the function values over the *entire* domain, just as in a pseudospectral method. If using infinitely smooth RBFs, this can lead to spectral (exponential) convergence of the RBF interpolant for smooth data [37].

Three global RBF collocation methods are presented here: Kansa’s method, Fasshauer’s method and Direct collocation. Additionally, the RBF-pseudospectral (RBF-PS) method is shown as an extension to fit global RBF methods into the framework of lower complexity pseudo-spectral methods.

This survey of RBF PDE methods frames the context in which RBF-FD was developed, and illustrates both the benefits and pitfalls inherited from its predecessors.

2.1 Survey of Related Work

In Radial Basis Function methods, radially symmetric functions provide a non-orthogonal basis used to interpolate between nodes of a point cloud. RBFs are univariate and a function of distance from a center point defined in \mathbb{R}^d , so they easily extend into higher dimensions without significant change in programming complexity. Examples of commonly used RBFs from the literature are provided in Table 2.1; 2D representations of the same functions can be found in Figure 2.1. Figure 2.2 illustrates the radial symmetry of RBFs—in this case, a Gaussian RBF—in the first three dimensions.

RBF methods are based on a superposition of translates of these radially symmetric functions, providing a linearly independent but non-orthogonal basis used to interpolate between nodes in d -dimensional space. The interpolation problem—referred to as *RBF scattered data interpolation*—seeks the unknown coefficients, $\mathbf{c} = \{c_j\}$, that satisfy:

$$\sum_{j=1}^N \phi_j(r(\mathbf{x})) c_j = f(\mathbf{x}),$$

where $\phi_j(r(\mathbf{x}))$ is an RBF centered at $\{\mathbf{x}_j\}_{j=1}^n$. In theory the radial coordinate, $r(\mathbf{x})$, could be any distance metric, but is most often assumed to be $r(\mathbf{x}) = \|\mathbf{x} - \mathbf{x}_j\|_2$ (i.e., Euclidean distance), as it is here. The coefficients \mathbf{c} result in a smooth interpolant that collocates sample values $f(\mathbf{x}_j)$. An example of RBF interpolation in 2D using 15 Gaussians is shown in Figure 2.3.

RBFs have been shown in some cases to have exponential convergence for function approximation [26]. It is also possible to reformulate RBF methods as pseudospectral methods that have generated solutions to ill-posed problems for which Chebyshev-based and other pseudospectral methods fail [24]. However, as with all methods, RBFs come with certain limitations. For example, RBF interpolation is—in general—not a well-posed problem, so it requires careful choice of positive definite or conditionally positive definite basis functions (see [26, 52] for details).

RBFs depend on a shape or support parameter ϵ that controls the width of the function. The functional form of the shape function becomes $\phi(\epsilon r(\mathbf{x}))$. For simplicity in what follows, the notation $\phi_j(\mathbf{x})$ implies $\phi(\epsilon \|\mathbf{x} - \mathbf{x}_j\|_2)$. Decreasing ϵ increases the support of the RBF and

Name	Abbrev.	Formula	Order (m)
Multiquadric	MQ	$\sqrt{1 + (\varepsilon r)^2}$	1
Inverse Multiquadric	IMQ	$\frac{1}{\sqrt{1+(\varepsilon r)^2}}$	0
Gaussian	GA	$e^{-(\varepsilon r)^2}$	0
Thin Plate Splines	TPS	$r^2 \ln r $	2
Wendland (C^2)	W2	$(1 - \varepsilon r)^4(4\varepsilon r + 1)$	0

Table 2.1: Examples of frequently used RBFs based on [26, 43]. ε is the support parameter. All RBFs have global support. For compact support, enforce a cut-off radius (see Equation 2.1).

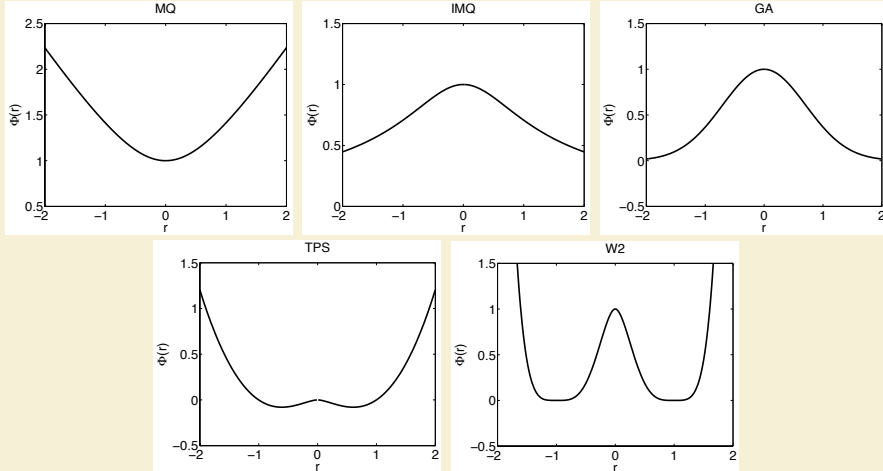


Figure 2.1: Example RBF shapes from Table 2.1 with parameter $\varepsilon = 1$.

in most cases, the accuracy of the interpolation, but worsens the conditioning of the RBF interpolation problem [75]. This inverse relationship is widely known as the *Uncertainty Relation* [52, 75]. Fortunately, recent algorithms such as Contour-Padé [36] and RBF-QR [38, 42] allow for numerically stable computation of interpolants in the nearly flat RBF regime (i.e., $\epsilon \rightarrow 0$) where high accuracy has been observed [43, 59].

RBF methods for interpolation first appeared in 1971 with Hardy's seminal research on multiquadratics [49]. In his 1982 survey of scattered data interpolation methods [44], Franke rated multiquadratics first-in-class against 28 other methods (3 of which were RBFs) [44]. Many other RBFs, including those presented in Table 2.1 have been applied in literature, but for PDEs in particular, few can rival the attention received by multiquadratics. Recently, however, Gaussian RBFs are on the rise due to recent advances in eigenvalue stabilization and new methods for investigating the $\epsilon \rightarrow 0$ regime (see e.g., [38, 39]).

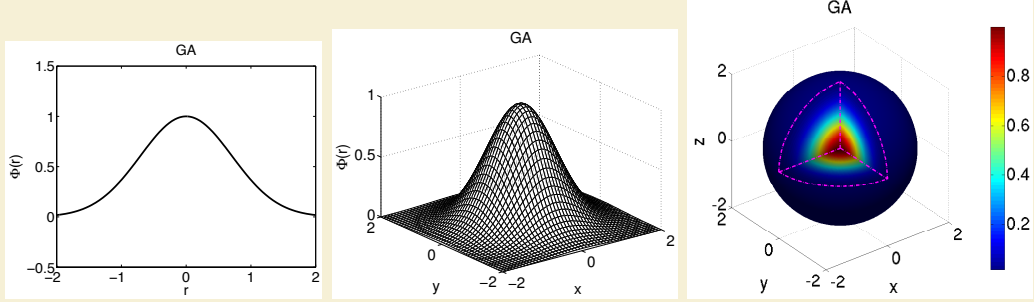


Figure 2.2: The Gaussian (GA) RBF (Table 2.1) with parameter $\epsilon = 1$ and r in $D = 1, 2$ and 3 .

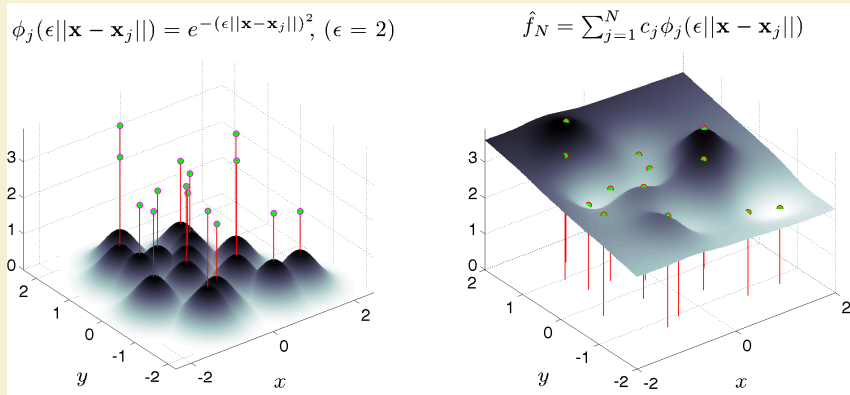


Figure 2.3: RBF interpolation using 15 translates of the Gaussian RBF with $\epsilon = 2$. One RBF is centered at each node in the domain. Linear combinations of these produce an interpolant over the domain passing through known function values.

By 1990, the understanding of the scientific community regarding RBFs was sufficiently developed for collocating PDEs [55, 56]. PDE collocation seeks a solution of the form

$$(\mathcal{L}u)(x_i) = \sum_{j=1}^N \phi_j(x_i) c_j = f(x_i)$$

where \mathcal{L} is, in general, a nonlinear differential operator acting on $u(x)$. The solution $u(x)$ is expressed as a linear combination of N basis functions $\phi_j(x)$, not necessarily RBFs:

$$u(x) = \sum_{i=1}^N \phi_j(x) c_j$$

As in the problem of RBF scattered data interpolation, $\mathbf{c} = \{c_j\}$ is the unknown coefficient vector. Under the assumption that \mathcal{L} is a linear operator, one can collocate the differential equation. Alternatively, individual derivative operators can be expressed as linear combinations of the unknowns u_j (leading to the RBF-FD methods). In all cases, a linear system

Interpolation Type	Dense/Sparse A	Dim(A) ($N_S \ll N$)	# of A^{-1}	RBF Support
Global	Dense	$N \times N$	1	Global
Compact	Sparse	$N \times N$	1	Compact
Local	Dense	$N_S \times N_S$	N	Global/Compact

Table 2.2: RBF interpolation types and properties, assuming a problem with N nodes.

of equations arises, with different degrees of sparsity, dependent on the chosen basis functions and how the various constraints are enforced. While $\phi_j(x)$ is restricted to RBFs in this context, note that spectral methods, finite-element or spectral-element methods can be formulated in similar fashion with alternative basis functions. Of course, u can be a vector of unknown variables (\mathbf{c} then becomes a matrix).

Table 2.3 classifies references according to their choice of collocation method and RBF interpolation type. There are three main categories of RBF interpolation listed in Table 2.2. The first is *Global* in the case that a single, large ($N \times N$) and dense matrix corresponding to globally supported RBFs is inverted; second, *Compact* if compactly supported RBFs are used to produce a single, large, but *sparse* matrix; and third, *Local* if compactly supported RBFs are used to produce many small but dense matrices with one corresponding to each collocation point. In all three cases the matrices are symmetric and with the correct choice of RBF they are at least conditionally positive definite. The final row of Table 2.3 considers literature on the RBF-FD method and is discussed in depth in Chapter 3.

We note that three types of collocation occur throughout the RBF literature: Kansa's unsymmetric collocation method [55, 56], Fasshauer's symmetric collocation method [25], and the Direct collocation method [28].

We now turn to discussion of the benefits and shortcomings of each RBF method, before covering derivation of the methods.

2.1.1 Global RBF Methods

Kansa's method [55, 56] (a.k.a. unsymmetric collocation) was the first RBF method for PDEs, and is still the most frequently used method. The idea behind Kansa's method is that an approximate solution to the PDE can be found by finding an interpolant which satisfies the differential operator with zero residual at a set of *collocation points* (these coincide with the RBF centers). To find the interpolant, the differential equation is formulated as a two block (unsymmetric) linear system with: 1) the approximation of values at boundary points with boundary data only, and 2) the approximation of interior points by directly applying the differential operator. It was shown in [25, 50] that the unsymmetric linear system produced by Kansa's method does not guarantee non-singularity; although it is also noted that in practice singularities are rare encounters [59].

The second alternative for RBF collocation, is based on Hermite scattered data interpolation (see [102]). The so-called *Fasshauer* or *Symmetric Collocation* method ([25])

performs a change of basis for the interpolant by directly applying the differential operator to the RBFs. It then collocates using the same approach as Kansa's method [59, 82]. The resulting block structure of the linear system is symmetric and guaranteed to be non-singular [25]. In comparison to Kansa's method, the disadvantages of Fasshauer's method include: a) requirement of higher order differentiability of the basis functions (to satisfy double application of the differential operator) and b) the linear system is larger and more complex to form [26]. As [50] points out, the possible existence of a singularity in Kansa's method is not enough to justify the added difficulties of using Fasshauer's method.

The last collocation method, *Direct Collocation*, was introduced by Fedoseyev, Friedman and Kansa [28] and satisfies the differential operator on the interior and the boundary. Larsson and Fornberg [59] observe that this third method has a matrix structure similar to that found in Kansa's method; however, it is noted that the dimensions of the matrix blocks for each method differ. This is due to collocation constraints added for the differential operator applied to the boundary. Aside from the survey on RBF collocation presented by Larsson and Fornberg [59], no related work was found that applied, or investigated, this method further.

Both Kansa's method and Fasshauer's methods were shown in [24] to fit well in the generalized framework of pseudo-spectral methods with a subtle change in algorithm. While collocation methods explicitly compute the coefficients for a continuous derivative approximation, their alternates, referred to in literature as RBF-pseudospectral (RBF-PS) methods, never explicitly compute the interpolant coefficients. Instead, a differentiation matrix (DM) is assembled and used to approximate derivates at the collocation points only [27]. Since most computational models are simply concerned with the solution at collocation points, the change to assemble DMs as in RBF-PS is organic.

Following the evolution of the RBF-PS algorithm, applications of global RBFs in the classic collocation sense (i.e., without the RBF-PS DMs) become impractical. This statement stems from the algorithmic complexity of each method. Global RBF methods result in full matrices [26]. The global collocation methods then scale on the order of $O(N^3)$ floating point operations (FLOPs) to solve for weighting coefficients on a given node layout, plus $O(N^2)$ to apply the weights for derivatives. If time-stepping is required, global collocation methods must recompute the time-dependent coefficients with additional cost dominated by $O(N^3)$ operations. RBF-PS methods have similar requirements for $O(N^3)$ operations to assemble the differentiation matrix and $O(N^2)$ to apply for derivatives. However, by avoiding time-dependent coefficients, the differentiation matrix application at each time-step is only $O(N^2)$ operations. As an aside, the $O(N^3)$ complexity for each method—typically due to an LU-decomposition, with subsequent forward- and back-solves—could be reduced. While not in mainstream use by the RBF community, [65] correctly points out that iterative solvers could be employed for $O(N^2)$ complexity.

Hon et al. [51] employed Kansa's method to solve shallow water equations for Typhoon simulation. In [33], Flyer and Wright employed RBF-PS (Kansa method) for the solution of shallow water equations on a sphere. Their results show that RBFs allow for longer time steps with spectral accuracy. The survey [29] by Flyer and Fornberg showcases RBF-PS (Kansa's method) out-performing some of the best available methods in geosciences, namely: Finite Volume, Spectral Elements, Double Fourier, and Spherical Harmonics. When applied to problems such as transport on the sphere [32], shallow water

	RBF Interpolation Type		
Method	Global (Dense)	Compact (Sparse Global)	Local
Kansa's Method	[24, 29, 32, 33, 36, 43, 44, 50, 51, 55, 56, 59, 66, 77, 100]	[43, 91]	[21, 57, 89, 90]
Fasshauer's Method	[24, 25, 59]	[63]	[82, 83, 84]
Direct Collocation	[28, 59]		[11, 12, 19, 30, 31, 38, 39, 78, 79, 98, 99, 101]
RBF-FD	N/A	N/A	

Table 2.3: Classification of references based on choice of RBF interpolation types and method for solving PDEs. References may appear in multiple cells according to the breadth of their research.

equations [33], and 3D mantle convection [100], RBF-PS consistently required fewer time steps, and a fraction of the nodes for similar accuracy [29].

2.1.2 Compactly Support RBFs

Thus far, all cases of collocation and interpolation mentioned have assumed globally supported RBFs. While global RBFs are well-studied and have nice properties, a major limitation is the large, dense system that must be solved. One alternative to global support is to use a set of compactly supported RBFs (CSRBFs) that are defined as:

$$\phi(r) = \begin{cases} \varphi(r) & r \in [0, 1] \\ 0 & r > 1 \end{cases} \quad (2.1)$$

where a cut-off radius is defined past which the RBF (in this case $\varphi(r)$) has no influence on the interpolant. Note that the radius can be scaled to fit a desired support. Methods that leverage CSRBFs produce a global interpolation matrix that is *sparse* and therefore results in a system that is more efficiently assembled and solved with smaller memory requirements [26]. The actual complexity estimate of the CSRBF method depends on the sparsity of the problem as well as the ordering of the assembled system. Assuming $n \ll N$ where n represents the number of nodes in support, [106] lists the complexity as dominated by $O(N)$ for properly structured systems within MATLAB, and the investigation in [65] found $O(N^{1.5})$ consistent with the estimate provided by their choice of general sparse solver package. A multi-level CSRBF method, introduced by Fasshauer [26], collocates solutions over multiple grid refinements to achieve reduced $O(N)$ complexity, but the method is plagued by poor convergence. It is also worth noting that in the context of CSRBFs, analogues to Kansa's

method and Fasshauer's method are known by the names *radial point interpolation method (RPIM)* [91] and *radial point interpolation collocation method (RPICM)* [63], respectively. A more thorough survey of CSRBF history can be found in [26, 52].

CSRBFs have attracted a lot of attention in applications. For example, in the field of dynamic surface and image deformation, compact support allows for local transformations which do not induce global deformation (see e.g., [15, 61, 103]).

2.1.3 Local RBF Methods

Around 2005, Šarler and Vertnik [89, 90] demonstrated that if compactly supported RBFs are chosen, the traditional global collocation matrix from Kansa's method, can be avoided altogether in favor of small localized collocation matrices defined for each node. Local collocation still faces possible ill-conditioning and singularities like global collocation, but make it easier to distribute computation across parallel systems. Also, the smaller linear systems can be solved with less conditioning issues. In [90], the authors consider 2D diffusion problems. Divo and Kassab [21] employ the method for Poisson-like PDEs including fluid flow and heat transfer. Kosec and Šarler [57] apply the same technique to solve coupled heat transfer and fluid flow problems.

In similar fashion, Stevens et al. [84] introduced a local version of Fasshauer's method called *local Hermitian interpolation*. The authors have applied their method to 3D soil problems based on transient Richards' equations [82, 83, 84].

2.2 Comparison of RBF Methods

We now detail RBF methods for PDEs leading up to the derivation of RBF-FD.

Following [66], consider a PDE expressed in terms of a (linear) differential operator, \mathcal{L} :

$$\begin{aligned}\mathcal{L}u &= f && \text{on } \Omega \\ u &= g && \text{on } \Gamma\end{aligned}$$

where Ω is the interior of the physical domain, Γ is the boundary of Ω and f, g are known explicitly. In the case of a non-linear differential operator, a Newton's iteration, or some other method, can be used to linearize the problem (see e.g., [101]); of course, this increases the complexity of a single time step. Then, the unknown solution, u , which produces the observations on the right hand side can be approximated by an interpolant function u_ϕ expressed as a linear combination of radial basis functions, $\{\phi_j(x) = \phi(\|x - x_j\|)\}_{j=1}^N$, and polynomial functions $\{P_l(x)\}_{l=1}^M$:

$$u_\phi(x) = \sum_{j=1}^N \phi_j(x) c_j + \sum_{l=1}^M P_l(x) d_l, \quad P_l(x) \in \Pi_p^d \quad (2.2)$$

where $\phi_j(x) = \|x - x_j\|_2$ (Euclidean distance). The second sum represents a linear combination of polynomials that enforces zero approximation error when $u(x)$ is a polynomial of degree less than or equal to p . The variable d is the problem dimension (i.e., $u_\phi(x) \in \mathbb{R}^d$). To eliminate degrees of freedom for well-posedness, p should be greater than or equal to the

order of the chosen RBF (see Table 2.1) [52]. Note that Equation 2.2 is evaluated at $\{x_j\}_{j=1}^N$ data points through which the interpolant is required to pass with zero residual. The x_j 's are known as *collocation points* (a.k.a. trial points), taken as the RBF centers. The test points, x , usually coincide with collocation points, although this is not a requirement.

To clarify the role of the polynomial part in Equation 2.2, it is necessary to put aside the PDE for the moment and consider only the problem of *scattered data interpolation* with Radial Basis Functions.

2.2.1 RBF Scattered Data Interpolation

Borrowing notation from [26, 52], we seek an interpolant of the form

$$f(x) = \sum_{j=1}^N \phi_j(x) c_j$$

where $f(x)$ is expressed as a scalar product between the unknown coefficient weights c_j and the radial basis functions $\phi_j(x)$.

To obtain the unknown coefficients, c_j , form a linear system in terms of the N RBF centers:

$$\begin{aligned} f(x) &= \sum_{j=1}^N c_j \phi_j(x) \quad \text{for } x = \{x_j\}_{j=1}^N \\ (\mathbf{f}) &= [\phi] (\mathbf{c}) \end{aligned}$$

The invertibility of this system depends on the choice of RBF, so one typically chooses a function that is positive definite to avoid issues. It has been shown (see [26, 52]) that some choices of RBFs (e.g. multiquadratics and thin-plate splines [50]) are not positive definite and therefore there is no guarantee that the approximation is well-posed. A sufficient condition for well-posedness is that the matrix be *conditionally positive definite*. In [26], Fasshauer demonstrates that conditional positive definiteness is guaranteed when Equation 2.2 exactly reproduces functions of degree less than or equal m . For RBF scattered data interpolation in one dimension, this can be achieved by adding a polynomial of order m with $M = \binom{m+1}{1}$ terms (e.g., x^0, x^1, \dots, x^m). In \mathbb{R}^d , $M = \binom{m+d}{d}$ [52], giving

$$\begin{aligned} \sum_{j=1}^N c_j \phi_j(x) + \sum_{l=1}^M d_l P_l(x) &= f(x), \quad P_l(x) \in \Pi_m^d \\ [\phi \ P] \begin{pmatrix} \mathbf{c} \\ \mathbf{d} \end{pmatrix} &= (\mathbf{f}) \end{aligned} \tag{2.3}$$

where the second summation (referred to as *interpolation conditions* [52]) ensures the minimum degree of the interpolant. Refer to Table 2.1 for a short list of recommended RBFs and minimally required orders of m . This document prefers the Gaussian RBF. Notice, in Equation 2.3, that the interpolation conditions add M new degrees of freedom, so M additional constraints are necessary to square the system. In this case:

$$\sum_{j=1}^N c_j P_l(x_j) = 0, \quad l = 1, \dots, M$$

or

$$P^T c = 0. \quad (2.4)$$

It is now possible again to write the interpolation problem as a complete linear system using Equations 2.3 and 2.4:

$$\underbrace{\begin{bmatrix} \phi & P \\ P^T & 0 \end{bmatrix}}_A \begin{pmatrix} c \\ d \end{pmatrix} = \begin{pmatrix} f \\ 0 \end{pmatrix} \quad (2.5)$$

Equation 2.5—typically a dense system except in the case of RBFs with compact support—can be solved efficiently via standard methods like LU-decomposition. With the coefficients, the interpolant can be sampled at any test points, $\{x_i\}_{i=1}^n$, by substitution into Equation 2.3:

$$\begin{aligned} f(x_i) &= \sum_{j=1}^N c_j \phi_j(x_i) + \sum_{l=1}^M d_l P_l(x_i) \\ &= \underbrace{\begin{bmatrix} \phi & P \end{bmatrix}}_B \begin{pmatrix} c \\ d \end{pmatrix} \Big|_{x=x_i} \end{aligned} \quad (2.6)$$

2.2.2 Reconstructing Solutions for PDEs

In the next few subsections, collocation equations are considered based on this general form:

$$\begin{aligned} \mathcal{L}u_\phi(x) &= f(x) && \text{on } \Omega \\ \mathcal{B}u_\phi(x) &= g(x) && \text{on } \Gamma \end{aligned}$$

where the methods presented below will apply the differential operators, \mathcal{L} and \mathcal{B} , to different choices of u_ϕ and different sets of collocation points. In many applications \mathcal{L} is chosen as a differential operator (e.g., $\frac{\partial}{\partial x}$, ∇ , ∇^2) and $\mathcal{B} = I$ (i.e. identity operator for Dirichlet boundary conditions) for PDEs. For RBF scattered data interpolation, $\mathcal{L} = I$. There are also applications where \mathcal{L} is a convolution operator (see e.g., [9, 10]) capable of smoothing/de-noising a surface reconstructed from point clouds.

For all the methods that follow a linear system is generated:

$$A_{\mathcal{L}} \begin{pmatrix} c \\ d \end{pmatrix} = \begin{pmatrix} f \\ 0 \end{pmatrix}$$

$$\begin{pmatrix} c \\ d \end{pmatrix} = A_{\mathcal{L}}^{-1} \begin{pmatrix} f \\ 0 \end{pmatrix}$$

where matrix $A_{\mathcal{L}}$ depends on the choice of collocation method.

Once the linear system is solved, the value $u(x)$ is reconstructed at the test points following Equation 2.6:

$$\begin{aligned} u(x) &\approx [\phi \quad P] \begin{pmatrix} c \\ d \end{pmatrix} \Big|_{x=x_i} \\ &\approx BA_{\mathcal{L}}^{-1} \begin{pmatrix} f \\ 0 \end{pmatrix} \end{aligned} \quad (2.7)$$

Likewise, to obtain differential quantities,

$$\begin{aligned} \mathcal{L}u(x) &\approx [\phi_{\mathcal{L}} \quad P_{\mathcal{L}}] \begin{pmatrix} c \\ d \end{pmatrix} \Big|_{x=x_i} \\ &\approx B_{\mathcal{L}}A_{\mathcal{L}}^{-1} \begin{pmatrix} f \\ 0 \end{pmatrix} \end{aligned}$$

2.2.3 PDE Methods

Now, since $u_{\phi}(x)$ from Equation 2.2 cannot (in general) satisfy the PDE everywhere, the PDE is enforced at a set of collocation points, which are distributed over both the interior and the boundary. Again, these points do not necessarily coincide with the RBF centers, but it is convenient for this to be true in practice. Also, for each of the methods the choice of RBF can be either global, resulting in a large dense system, or compact, resulting in a large sparse system.

Kansa's Method. The first global RBF method for PDEs, *Kansa's method* [55, 56], collocates the solution through known values on the boundary, while constraining the interpolant to satisfy the PDE operator on the interior. This is equivalent to choosing u_{ϕ} according to Equation 2.2. The resulting system is given by [66]; assuming that \mathcal{L} is a linear operator,

$$\mathcal{L}u_{\phi}(x_i) = \sum_{j=1}^N c_j \mathcal{L}\phi_j(x_i) + \sum_{l=1}^M d_l \mathcal{L}P_l(x_i) = f(x_i) \quad i = 1, \dots, n_I \quad (2.8)$$

$$\mathcal{B}u_{\phi}(x_i) = \sum_{j=1}^N c_j \mathcal{B}\phi_j(x_i) + \sum_{l=1}^M d_l \mathcal{B}P_l(x_i) = g(x_i) \quad i = n_I + 1, \dots, n \quad (2.9)$$

$$\sum_{j=1}^N c_j P_l(x_j) = 0 \quad l = 1, \dots, M \quad (2.10)$$

where n_I are the number of interior collocation points, with the number of boundary collocation points equal to $n - n_I$. First, observe that the differential operators are applied directly to the RBFs inside summations, rather than first solving the scattered data interpolation problem and then applying the operator to the interpolant. Second, since the basis functions are known analytically, it is possible (although sometimes painful) to derive $\mathcal{L}\phi$ (refer to [26] for RBF derivative tables); the same is true for the polynomials P_l .

We can now reformulate Kansa's method as the linear system:

$$\underbrace{\begin{bmatrix} \phi_{\mathcal{L}} & P_{\mathcal{L}} \\ \phi_{\mathcal{B}} & P_{\mathcal{B}} \\ P^T & 0 \end{bmatrix}}_{A_{\mathcal{L}}} \begin{pmatrix} c \\ d \end{pmatrix} = \begin{pmatrix} f \\ g \\ 0 \end{pmatrix} \quad (2.11)$$

where $\phi_{\mathcal{L}} = \mathcal{L}\phi$, $P_{\mathcal{L}} = \mathcal{L}P$ are the interior components (Equation 2.8), $\phi_{\mathcal{B}}$ and $P_{\mathcal{B}}$ are the boundary components (Equation 2.9), and $P^T = [P_{\mathcal{L}}^T \ P_{\mathcal{B}}^T]$ are constraints for both interior and boundary polynomial parts (Equation 2.10). From Equation 2.11 it should be clear why Kansa's method is also known as the *Unsymmetric* collocation method.

Recall that the matrix in Equation 2.11 has no guarantee of non-singularity [25]; however, singularities are rare in practice [59].

Fasshauer's Method. *Fasshauer's method* [25] addresses the problem of singularity in Kansa's method by assuming the interpolation to be Hermite. That is, it requires higher differentiability of the basis functions (they must be at least C^k -continuous if \mathcal{L} is of order k). Leveraging this assumption, Fasshauer's method chooses:

$$u_{\phi}(x_i) = \sum_{j=1}^{N_I} c_j \mathcal{L}\phi_j(x_i) + \sum_{j=N_I+1}^N c_j \mathcal{B}\phi_j(x_i) + \sum_{l=1}^M d_l P_l(x_i) \quad (2.12)$$

as the interpolant passing through collocation points. Note N_I is used here to specify the number of RBF centers in the interior of Ω . Here the interpolant is similar to Equation 2.2, but a change of basis functions is used for the expansion: $\mathcal{L}\phi_j(x)$ on the interior and $\mathcal{B}\phi_j(x)$ on the boundary.

Substituting Equation 2.12 into Equations 2.8-2.10 gives

$$\begin{aligned} \sum_{j=1}^{N_I} c_j \mathcal{L}^2 \phi_j(x_i) + \sum_{j=N_I+1}^N c_j \mathcal{L}\mathcal{B}\phi_j(x_i) + \sum_{l=1}^M d_l \mathcal{L}P_l(x_i) &= f(x_i) \quad i = 1, \dots, n_I \\ \sum_{j=1}^{N_I} c_j \mathcal{B}\mathcal{L}\phi_j(x_i) + \sum_{j=N_I+1}^N c_j \mathcal{B}^2 \phi_j(x_i) + \sum_{l=1}^M d_l \mathcal{B}P_l(x_i) &= g(x_i) \quad i = n_I + 1, \dots, n \\ \sum_{j=1}^{N_I} c_j \mathcal{L}P_l(x_j) + \sum_{j=N_I+1}^N c_j \mathcal{B}P_l(x_j) &= 0 \quad l = 1, \dots, M \end{aligned} \quad (2.13)$$

which becomes the following:

$$\underbrace{\begin{bmatrix} \phi_{\mathcal{LL}} & \phi_{\mathcal{LB}} & P_{\mathcal{L}} \\ \phi_{\mathcal{BL}} & \phi_{\mathcal{BB}} & P_{\mathcal{B}} \\ P_{\mathcal{L}}^T & P_{\mathcal{B}}^T & 0 \end{bmatrix}}_{A_{\mathcal{L}}} \begin{pmatrix} c \\ d \end{pmatrix} = \begin{pmatrix} f \\ g \\ 0 \end{pmatrix} \quad (2.14)$$

Note that $\phi_{\mathcal{LL}}$ represents the first summation in Equation 2.13.

The symmetry of Fasshauer's (*symmetric collocation*) method is apparent in Equation 2.14. Likewise, it is clear that the symmetric method requires more storage and computation to solve compared to Kansa's method. However, based on the assumption that collocation points coincide with RBF centers, the symmetry reduces storage requirements by half.

Direct Collocation. In *Direct collocation* (see [28, 59], the interpolant is chosen as Equation 2.2 (the same as Kansa's method). However, the Direct method collocates both the interior and boundary operators at the boundary points:

$$\begin{aligned} \sum_{j=1}^N c_j \mathcal{L} \phi_j(x_i) + \sum_{l=1}^M d_l \mathcal{L} P_l(x_i) &= f(x_i) \quad i = 1, \dots, n \\ \sum_{j=1}^N c_j \mathcal{B} \phi_j(x_i) + \sum_{l=1}^M d_l \mathcal{B} P_l(x_i) &= g(x_i) \quad i = 1, \dots, n_B = n - n_I \\ \sum_{j=1}^N c_j P_l(x_j) &= 0 \quad l = 1, \dots, M \end{aligned} \quad (2.15)$$

Reformulating as a linear system provides:

$$\begin{bmatrix} \phi_{\mathcal{L}} & P_{\mathcal{L}} \\ \phi_{\mathcal{B}} & P_{\mathcal{B}} \\ P^T & 0 \end{bmatrix} \begin{pmatrix} c \\ d \end{pmatrix} = \begin{pmatrix} f \\ g \\ 0 \end{pmatrix} \quad (2.16)$$

While the final system in Equation 2.16 is structured the same as Kansa's method (Equation 2.11), careful inspection of the index i in Equations 2.8 and 2.15 reveals that Direct collocation produces a larger system.

RBF-PS. The extension of global collocation to traditional pseudo-spectral form was introduced by Fasshauer in [24]. Dubbed RBF-PS, the method utilizes the same logic from Kansa's and Fasshauer's collocation methods to form matrix $A_{\mathcal{L}}$ (i.e., $A_{\mathcal{L}}$ can be either Equation 2.11 or 2.14). However, RBF-PS subtly assumes the solution, $u(x)$, is only required at collocation points (i.e., $\{x_i\} = \{x_c\}$) [24, 26]. Then, extending Equation 2.7, RBF-PS gives:

$$\begin{aligned} u(x) &= (BA_{\mathcal{L}}^{-1}) \begin{pmatrix} f \\ 0 \end{pmatrix} \\ &= D_{\mathcal{L}}^T \begin{pmatrix} f \\ 0 \end{pmatrix}. \end{aligned} \quad (2.17)$$

where $D_{\mathcal{L}}$ is a discrete differentiation matrix (DM) for the operator \mathcal{L} . Here, $D_{\mathcal{L}}$ is independent of the function $f(x)$ and is assembled by solving the system:

$$D_{\mathcal{L}} = A_{\mathcal{L}}^{-T} B^T \quad (2.18)$$

An LU-decomposition ($O(N^3)$) in preprocessing with forward- and back-solves ($O(N^2)$) are fitting to efficiently solve the multiple RHS system [26, 100].

Since matrix $D_{\mathcal{L}}$ is independent of functions $u(x)$ and $f(x)$, the matrix requires update only if the RBF centers move—a compelling benefit for time-dependent problems on stationary nodes. The complexity of RBF-PS for time-dependent solutions is then reduced to a matrix-vector multiply ($O(N^2)$) for each time-step. In contrast, classic RBF collocation methods also construct LU factors of $A_{\mathcal{L}}^{-1}$ in preprocessing, but delay application of forward- and back-solves to acquire time-dependent weighting coefficients at each time-step. This is then followed by the pre-multiply of B (i.e., additional $O(N^2)$) to complete the time-step.

2.2.4 Local Methods

Another trend in RBF methods is to use compact support to produce local linear systems defined at each collocation point. Examples of this include [89, 90] for Kansa’s method, [82, 83, 84] for Fasshauer’s method. To our knowledge no one has considered local Direct collocation. Also, instead of specifying a cut-off radius for RBF support, some authors specify the exact stencil size (i.e., number of neighboring points to include); see e.g., [21, 82].

After observing the general structure of the symmetric and unsymmetric collocation methods above, it is necessary only to present the symmetric (i.e. Fasshauer’s) local method and note that in the unsymmetric case certain blocks will be zero allowing the system to shrink.

The formula for the interpolant local to the (k)-th collocation point (i.e., RBF center) is given by:

$$u_{\phi}^{(k)}(x_i) = \sum_{j(k)=1}^{N_I} c_j^{(k)} \mathcal{L}\phi_j(x_i) + \sum_{j(k)=N_I+1}^{N_S} c_j^{(k)} \mathcal{B}\phi_j(x_i) + \sum_{l=1}^M d_l^{(k)} P_l(x_i)$$

where N_S represents the number of points that defines the local stencil; N is possibly a function of the cut-off radius in the RBF, N_I is the number of interior stencil points (those points of the stencil that lie in the interior of Ω). The index j is a function of the stencil center k allowing the system to include a local neighborhood of stencil points.

This results in a linear system with similar structure to the global collocation problem, but the dimensions are much smaller:

$$\underbrace{\begin{bmatrix} \phi_{\mathcal{L}\mathcal{L}} & \phi_{\mathcal{L}\mathcal{B}} & P_{\mathcal{L}} \\ \phi_{\mathcal{B}\mathcal{L}} & \phi_{\mathcal{B}\mathcal{B}} & P_{\mathcal{B}} \\ P_{\mathcal{L}}^T & P_{\mathcal{B}}^T & 0 \end{bmatrix}}_{A_{\mathcal{L}}} \begin{pmatrix} c^{(k)} \\ d^{(k)} \end{pmatrix} = \begin{pmatrix} f \\ g \\ 0 \end{pmatrix} \quad (2.19)$$

Solving this system gives an interpolant locally defined around the stencil center. Note that approximating the PDE solution $u(x)$ requires finding the stencil center nearest x , then using the local interpolant for that stencil. Since interpolation is local (i.e., $c_j^{(k)}$ ’s are unique to each RBF center), reconstructing the derivatives with Equation 2.8 is limited to an inner product for each center rather than the matrix-vector grouping possible with global RBFs. This approach decomposes the problem into smaller and more manageable parts. However, because the interpolants are local, there is no notion of global continuity/smoothness of the solution.

2.3 Recent Advances in Conditioning

The most limiting factor in the success of RBF methods has not been the complexity of the methods, nor the task of approximating derivatives. Rather, it is the support parameter, ϵ , and the dilemma one faces in the *Uncertainty Relation* [75]. Recall that as $\epsilon \rightarrow 0$, ill-conditioning of the RBF interpolation matrices increases, but so too does the approximation accuracy—that is, assuming a stable solution can be found. Likewise, as the number of collocation points increases, the range of ϵ for which the linear system has acceptable conditioning narrows. In [38], the authors observe that much of the literature on RBF methods seek to find optimal values of the support parameter ϵ for the highest accuracy in applications. Occasionally the optimal values lie within a range of acceptable conditioning to solve the linear systems directly (a.k.a. RBF-Direct solutions). More often, one must compromise between the accuracy loss for large ϵ and accuracy loss in RBF-Direct solutions due to lower values of ϵ . Many attempts to express the optimal ϵ as a function of problem size have also been thwarted as the impact on the optimal ϵ values in the face of small node perturbations is still not fully understood. This makes refinements a challenge to manage.

In an effort to overcome limitations due to conditioning, Fornberg and Wright [36] presented the *Contour-Padé* algorithm, which allows for numerically stable computation of highly accurate interpolants with nearly flat RBFs (i.e., $\epsilon \rightarrow 0$). Larsson and Fornberg [59] applied the algorithm to all three methods of collocation (Kansa's, Fasshauer's and Direct Collocation) with considerable gain in accuracy over solutions from classical second-order FD and a pseudospectral method. The Contour-Padé algorithm is not overly competitive due to the fact that it only supports fewer than a hundred in 2D and slightly more in 3D [41].

The *RBF-QR* method, was later introduced by Fornberg and Piret [42] in context of a sphere to let $\epsilon \rightarrow 0$ for a few thousand nodes. It was later extended to general 1D, 2D and 3D problems in [38]. The RBF-QR method uses a truncated expansion of RBFs in terms of spherical harmonics or Chebyshev polynomials and leverages QR factorization to create a new well-conditioned set of basis functions to reproduce the original RBF space. The well-conditioned basis set allows stable solution independent of the value ϵ . The cost of the method is demonstrated to increase as ϵ increases. Benchmarks in [38] show that double precision RBF-QR is between 3x-7x slower than RBF-Direct for the same values of ϵ . Fornberg, Larsson and Flyer [38] successfully implemented the 2D method in less than 100 lines of MATLAB code and apply RBF-QR to problems with 6000 quasi-uniform nodes and globally supported RBFs.

Between Contour-Padé and RBF-QR, global RBF methods overcame many conditioning issues for small to mid-sized problems. The lack of support for large problem sizes is discouraging, but it leads to an argument in favor of local methods like RBF-FD, which decrease the problem size to fit nicely within the scope of stable methods.

Most recently, Fornberg et al. [41] introduced a new method called RBF-GA, which performs a similar change of basis as RBF-QR, but the method avoids truncated infinite expansions by expressing the new basis functions in terms of an incomplete Gamma function. Unlike RBF-QR, this method is limited to Gaussian basis functions only. Benchmarks provided in [41] rank stable methods for RBFs from fastest to slowest as: RBF-Direct,

RBF-GA, and then RBF-QR. RBF-GA is also effective for a small number of nodes: a few hundred in 2D, and at least 500 in 3D. Unlike RBF-QR, which performs a change of basis on the interpolating matrix only, the RBF-GA method requires a complicated change of basis for the RHS as well [41].

Part II

RBF-FD for HPC Environments

CHAPTER 3

INTRODUCTION TO RBF-FD

RBF-generated Finite Differences (RBF-FD) were first introduced by Tolstykh in 2000 [88], but it was the simultaneous, yet independent, efforts in [78], [87], [99] and [11] that gave the method its real start.

The RBF-FD method is similar in concept to classical finite-differences (FD), in that derivatives of a function $u(x)$ are approximated by weighted combinations of n function values in a small neighborhood around a single *center* node, x_c . That is:

$$\mathcal{L}u(x) \Big|_{x=x_c} \approx \sum_{j=1}^n c_j u(x_j) \quad (3.1)$$

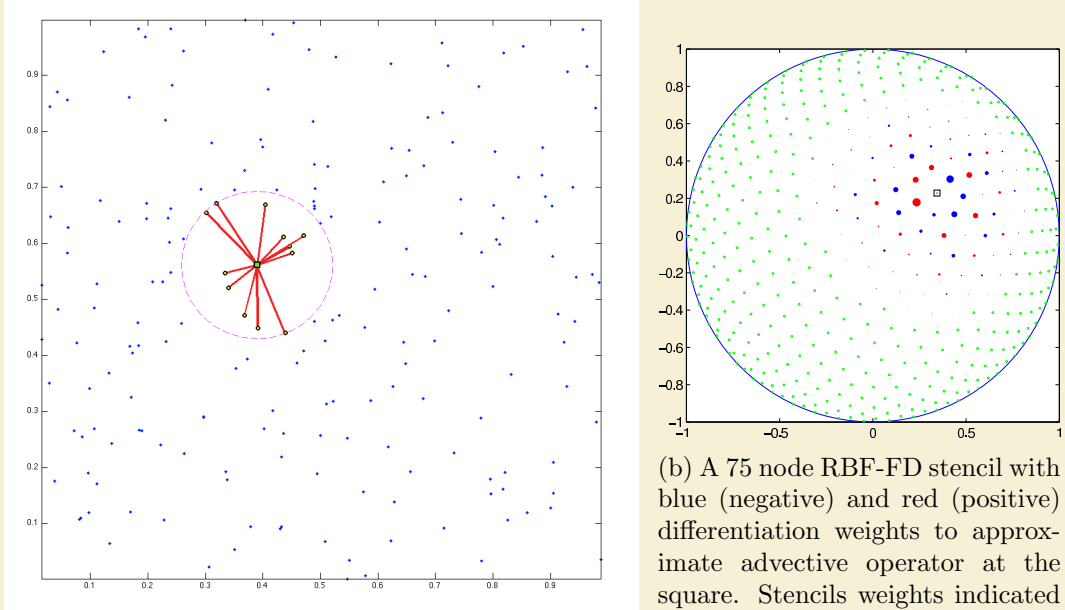
where $\mathcal{L}u$ again represents a differential operator on $u(x)$ (e.g., $\mathcal{L} = \frac{\partial}{\partial x}$). Here the n nodes are known as a *stencil* with size n . The c_j are *stencil weights*. In practice stencils include the center, x_c , plus the $n - 1$ nearest neighboring nodes. The definition of “nearest” can depend the choice of distance metric, but in all discussions to follow it is assumed to be Euclidean distance ($\|x - x_c\|_2$).

Figure 3.1 provides two examples of RBF-FD stencils. A single stencil of size $n = 13$ is depicted in Figure 3.1a within a domain of random points. The center, x_c , is represented by a green square, with 12 neighbors connected via red edges. The purple circle—the minimum covering circle for the stencil—illustrates that the 12 nearest neighbors are selected. Figure 3.1b presents a larger stencil ($n = 75$) on the unit sphere with red and blue disks surrounding the square center. Green disks are nodes outside of the stencil. Radii and color of the disks indicate magnitude and alternating sign of the weights, c_j .

Following [39], weights for a 1-D classical-FD stencil can be obtained by solving a Vandermonde system,

$$\begin{bmatrix} 1 & 1 & \cdots & 1 \\ x_1 & x_2 & \cdots & x_n \\ x_1^2 & x_2^2 & \cdots & x_n^2 \\ \vdots & \ddots & \ddots & \vdots \\ x_1^{n-1} & x_2^{n-1} & \cdots & x_n^{n-1} \end{bmatrix} \begin{pmatrix} c_1 \\ c_2 \\ c_3 \\ \vdots \\ c_n \end{pmatrix} = \begin{pmatrix} \mathcal{L}1|_{x=x_c} \\ \mathcal{L}x|_{x=x_c} \\ \mathcal{L}x^2|_{x=x_c} \\ \vdots \\ \mathcal{L}x^{n-1}|_{x=x_c} \end{pmatrix}, \quad (3.2)$$

where the the x_j are assumed to be distinct for guaranteed nonsingularity. In higher dimensions, multivariate polynomials dissolve the guaranteed nonsingularity of the Vandermonde



(a) A 13 node RBF-FD stencil of randomly distributed nodes. The stencil centered at the green square contains the 12 nearest neighbors contained within the minimum covering circle drawn in purple.

(b) A 75 node RBF-FD stencil with blue (negative) and red (positive) differentiation weights to approximate advective operator at the square. Stencils weights indicated by scale of disk radii. (Image courtesy of Bengt Fornberg and Natasha Flyer)

Figure 3.1: Examples of stencils computable with RBF-FD

system, so FD stencils are typically composed by adding weights from individual spatial directions.

In contrast to Equation 3.2, RBF-FD weights arise by enforcing that they be exact within the space spanned by the RBFs that are centered at stencil nodes (i.e., $\phi_j(x) = \phi(\epsilon\|x - x_j\|_2)$; an RBF centered at x_j). This amounts to replacing each polynomial basis function $\{1, x, x^2, \dots, x^{n-1}\}$ in Equation 3.2 with a d -dimensional RBF, $\phi_j(x)$, which allows for nonsingularity in d -dimensions on irregular node placements. Various studies [31, 34, 39, 101] show that better accuracy is achieved when the interpolant can exactly reproduce a constant, p_0 , such that

$$\mathcal{L}\phi_i(x) |_{x=x_c} = \sum_{j=1}^n c_j \phi_j(x_i) + c_{n+1} p_0 \quad \text{for } i = 1, 2, \dots, n$$

with $\mathcal{L}\phi_i$ provided by analytically applying the differential operator to the RBF. Assuming

$p_0 = 1$, the constraint $\sum_{i=1}^n c_i = \mathcal{L}p_0|_{x=x_c} = 0$ completes the system:

$$\begin{bmatrix} \phi_1(x_1) & \phi_2(x_1) & \cdots & \phi_n(x_1) & 1 \\ \phi_1(x_2) & \phi_2(x_2) & \cdots & \phi_n(x_2) & 1 \\ \vdots & \ddots & \ddots & \vdots & \vdots \\ \phi_1(x_n) & \phi_2(x_n) & \cdots & \phi_n(x_n) & 1 \\ 1 & 1 & \cdots & 1 & 0 \end{bmatrix} \begin{pmatrix} c_1 \\ c_2 \\ \vdots \\ c_n \\ c_{n+1} \end{pmatrix} = \begin{pmatrix} \mathcal{L}\phi_1(x)|_{x=x_c} \\ \mathcal{L}\phi_2(x)|_{x=x_c} \\ \vdots \\ \mathcal{L}\phi_n(x)|_{x=x_c} \\ 0 \end{pmatrix} \quad (3.3)$$

$$\begin{bmatrix} \phi & P \\ P^T & 0 \end{bmatrix} \begin{pmatrix} c_{\mathcal{L}} \\ d_{\mathcal{L}} \end{pmatrix} = \begin{pmatrix} \phi_{\mathcal{L}} \\ 0 \end{pmatrix}.$$

The resulting structure of Equation 3.3 is the same structure found in RBF scattered data interpolation (see Equation 2.5). As with other RBF methods, the choice of \mathcal{L} can be any linear operator. If \mathcal{L} is the identity operator, then the above procedure leads to RBF-FD weights for interpolation. If $\mathcal{L} = \frac{\partial}{\partial x}$, one obtains the weights to approximate the first derivative in x . Refer to [26] for a table of commonly used RBF derivatives. Section 3.3 provides a list of derivatives used in this work.

The small $(n+1) \times (n+1)$ system in Equation 3.3 is dense, and is easily solved at a cost of $O(n^3)$ floating point operations (FLOPs) using direct methods like LU-decomposition. The resulting stencil weights, $c_{\mathcal{L}} = \{c_j\}_{j=1}^n$ can be substituted into Equation 3.1 for the derivative approximation at x_c . Coefficient c_{n+1} ($d_{\mathcal{L}} = c_{n+1}$), included in the solution of Equation 3.3, is of no use and discarded once the system has been solved.

Based on the choice of support parameter, ϵ , the Equation 3.3 may suffer problems with conditioning. In such cases, stable methods for solving the system like Contour–Padé [99], RBF-QR [19, 38], or RBF-GA [41] may be preferred.

RBF-FD shares many advantages with global RBF methods. For example, the ability to function without an underlying mesh, easily extend to higher dimensions, and (in some cases) stability for large time steps. Unfortunately, spectral accuracy is lost due to the local nature of this stencil method. Other advantages of RBF-FD include low computational complexity together with high-order accuracy (6th to 10th order accuracy is common). As in classical FD methods, increasing the stencil size, n , increases the order accuracy of approximations. While not a panacea for PDEs, RBF-FD is simple to code, feature rich, and powerful in its ability to avoid singularities introduced by coordinate systems that might negatively impact other methods (see e.g., [32, 39]).

Author's Note: [Expand these reference descriptions](#)

RBF-FD have been successfully employed for a variety of problems including Hamilton-Jacobi equations [11], convection-diffusion problems [12, 82], incompressible Navier-Stokes equations [13, 78], transport on the sphere [39], and the shallow water equations [31]. Shu et al. [79] compared the RBF-FD method to Least Squares FD (LSFD) in context of 2D incompressible viscous cavity flow, and found that under similar conditions, the RBF-FD method was more accurate than LSFD, but the solution required more iterations of an iterative solver. RBF-FD was applied to Poisson's equation in [98]. Chandhini and Sanyasiraju [12] studied it in context of 1D and 2D, linear and non-linear, convection-diffusion equations, demonstrating solutions that are non-oscillatory for high Reynolds number, with improved accuracy over classical FD. An application to Hamilton-Jacobi problems [11], and 2D linear and non-linear PDEs including Navier-Stokes equations [78] have all been considered.

3.1 Multiple Operators

In many cases, multiple derivatives (e.g., $\mathcal{L} = \nabla^2, \frac{\partial}{\partial x}, \frac{\partial}{\partial y}$, etc.) are required at stencil centers. This is common, for example, when solving coupled PDEs. For RBF-FD, acquiring weights for each additional operator can be both straight-forward and computationally efficient. For each change of differential operator, observe that only the RHS of Equation 3.3 is modified. Thus, new operators amount to extending Equation 3.3 to solve

$$\begin{bmatrix} \phi & P \\ P^T & 0 \end{bmatrix} \begin{bmatrix} c_{\nabla^2} & c_x & c_y & \cdots \\ d_{\nabla^2} & d_x & d_y & \cdots \end{bmatrix} = \begin{bmatrix} \phi_{\nabla^2} & \phi_x & \phi_y & \cdots \\ 0 & 0 & 0 & \cdots \end{bmatrix}. \quad (3.4)$$

where multiple sets of weights (c_{∇}, c_x, c_y) are obtained simultaneously. This dense, symmetric, multiple RHS linear system is considered ideal by linear algebra packages. Many highly optimized routines exist to solve Equation 3.4 (e.g., LAPACK “dgesv”) [3].

3.2 Differentiation Matrices and Sparse Matrix-Vector Multiply (SpMV)

Typically, one needs derivatives at every node in the discretized domain to solve PDEs. To achieve this with RBF-FD, stencils are generated around every node in the domain. Stencils need not have the same size (n), but this is assumed here for simplicity in discussion, and is most common in literature. Furthermore, the number of stencils need not match the number of nodes in the domain, but this is also assumed. The small system solve in Equation 3.3 or 3.4 is repeated N times—once for each stencil—to obtain a total of $N \times n$ stencil weights per operator.

For PDEs, it is common practice to assemble a *differentiation matrix* (DM); a discrete representation of the PDE operator on the domain. Given the set of nodes in the domain, $\{x_k\}_{k=1}^N$, the c -th row of the DM represents the discrete PDE operator for the stencil centered at node x_c with stencil nodes $\{x_j\}_{j=1}^n$:

$$\begin{aligned} \mathcal{L}u(x) &\approx D_{\mathcal{L}}u \\ D_{\mathcal{L}}^{(c,k)} &= \begin{cases} c_j & x_k = x_j \\ 0 & x_k \neq x_j \end{cases} \end{aligned}$$

where (c, k) represents the (row, column) index of $D_{\mathcal{L}}$ and vector $u = \{u(x_k)\}_{k=1}^N$. Equation 3.1 can be rewritten as:

$$\mathcal{L}u(x) |_{x=x_c} \approx D_{\mathcal{L}}^{(c)}u .$$

DMs are utilized in both explicit and implicit modes. Here explicit implies evaluating the matrix-vector multiply to get derivative values, u' , from explicitly known vector of solution values u :

$$u' = D_{\mathcal{L}}u \quad (3.5)$$

whereas implicit solves for unknown u :

$$D_{\mathcal{L}}u = f \quad (3.6)$$

Note that the non-zeros in $D_{\mathcal{L}}$ are independent of the values in u . Approximating \mathcal{L} over any function reduces to sampling the function values at nodes $\{x_k\}_{k=1}^N$ and performing a matrix-vector multiply.

An example RBF-FD DM is illustrated in Figure 3.2. In this example, assume operator $\mathcal{L} = \frac{\partial}{\partial x}$ is approximated at all N stencil centers of an arbitrary domain. RBF-FD weights assemble the rows of the differentiation matrix, D_x . On each row, weights are indicated by blue dots. The sparsity of rows reflects the subset of $\{x_k\}_{k=1}^N$ included in corresponding stencils of size n . A mapping is assumed to exist that translates non-consecutive indices, k , to consecutive indices, j , and vice-versa. On the right hand side, discrete derivative values $\frac{du}{dx}$ are approximated at all stencil centers.

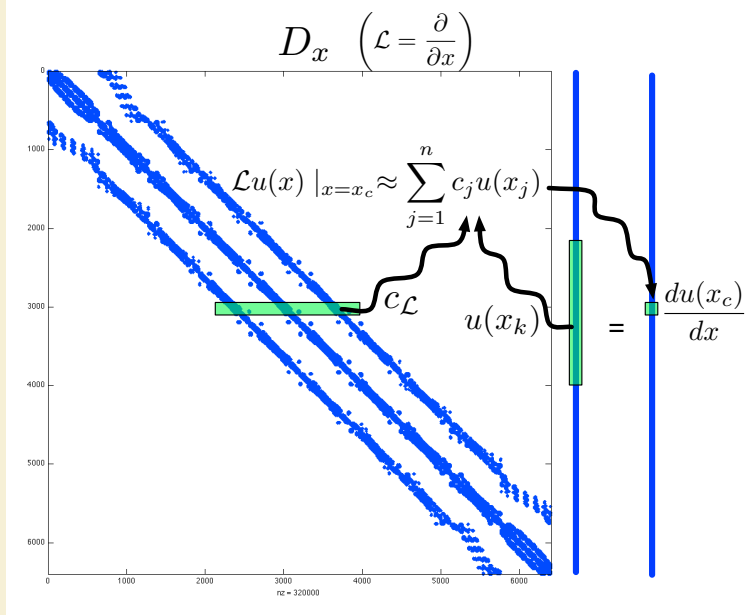


Figure 3.2: Differentiation matrix D_x is applied explicitly to calculate derivative approximations, $\frac{d}{dx}u(x)$.

Differentiation matrices are assembled at a cost of $O(n^3N)$ FLOPs. However, since the goal of RBF-FD is to keep stencils small ($n \ll N$), the cost of assembly scales as $O(N)$. Furthermore, RBF-FD weights are independent of function values ($u(x)$) and rely only on stencil node locations. The implications of this are as profound as in the context RBF-PS for time-dependent PDEs: the stencil weights are constant so long as the nodes are stationary. Thus, the DM assembly is part of a one-time preprocessing step.

For simple PDEs one often assembles a single DM to represent the operator for the entire differential equation, but RBF-FD allows flexibility in how operators are handled. Rather than a single DM, with weights from a new operator on the RHS of Equation 3.4, one may approximate the operator based on lower order derivatives. Consider for example,

the 2-D Laplacian operator, $\nabla^2 = \frac{\partial^2}{\partial x^2} + \frac{\partial^2}{\partial y^2}$:

$$\nabla^2 u \approx D_{\nabla^2} u$$

which can be expanded as:

$$\nabla^2 u \approx (D_{x^2} + D_{y^2}) u = D_{x^2} u + D_{y^2} u .$$

where either a single DM is composed by adding two lower order DMs, or the lower order DMs are directly multiplied against the vector u . Another option applies even lower order operators:

$$\nabla^2 u \approx D_x D_x u + D_y D_y u . \quad (3.7)$$

The choice of how the operators are approximated depends on the PDE and can be influenced by system memory limitations. For example, assume a coupled system of equations in 2-D where operators ∇ and ∇^2 are required. Then, Equation 3.4 is assembled and solved for the operators $\{\frac{\partial}{\partial x}, \frac{\partial}{\partial y}, \nabla^2\}$, with each DM stored in memory. This process is sufficient assuming all DMs fit adequately in the memory available. As an alternative, one may solve Equation 3.4 for operators $\{\frac{\partial}{\partial x}, \frac{\partial}{\partial y}\}$, reproduce ∇^2 with Equation 3.7, and reduce memory usage by 30%. On top of memory savings, this concept of composing DMs based on lower order operators extends to cases where PDEs require complex operators that are sufficiently difficult to apply to RBFs when deriving a new RHS for Equation 3.4.

The sparsity exhibited by the DM in Figure 3.2 is typical for RBF-FD. Consider that a problem size of $N = 10,000$ nodes and stencil size $n = 31$ is only 0.31% full (i.e., 99.79% of the matrix elements are zeros), and the percentage continues to decrease as N increases. Contrary to initial appearance, RBF-FD DMs like Figure 3.2 are not symmetric. This is true for two reasons: a) a stencil is generated based on $n - 1$ nearest neighbors to a center with no guarantee that any of the stencil nodes will include the center in their stencils; and b) even if the stencil connectivity were symmetric, each row of the DM contains a distinct set of weights that are a function of independent stencils. The only way to guarantee a symmetric system is to ensure all stencils are shaped the same, with the same number of nodes and node distribution relative to the center, plus all stencil nodes must have a bijective relationship (i.e., if A is connected to B , then B connects to A).

Best practices dictate that the DMs be stored in some type of compressed sparse storage that retains only non-zeros and their corresponding indices in memory. Note that with DMs stored as sparse representations, the matrix-vector multiply operation is distinguished as a *sparse matrix-vector multiply* (SpMV). SpMVs avoid unnecessary operations by only multiplying the nonzero elements of the matrix matched to corresponding values in the vector. The actual algorithm for SpMV depends on the choice of sparse storage. Chapter ?? demonstrates the pivotal role that sparse formats play in the performance of SpMV, and thus RBF-FD.

3.3 Weight Operators

In the course of this work a variety of operators are tested to solve PDEs. This section enumerates the operators and their corresponding equations for the RHS of Equation 3.3.

Whenever possible the general form of $\mathcal{L}\phi$ is provided; otherwise the Gaussian RBF ($\phi(r) = e^{-(\epsilon r)^2}$) is assumed.

3.3.1 First and Second Derivatives ($\frac{1}{r} \frac{\partial \phi}{\partial r}, \frac{\partial^2 \phi}{\partial r^2}$)

The following are used in subsequent derivatives:

$$\frac{1}{r} \frac{d}{dr} \phi(r) = -2\epsilon^2 \phi(r) \quad (3.8)$$

$$\frac{\partial^2 \phi}{\partial r^2} = \epsilon^2 (-2 + 4(\epsilon r)^2) \phi(r) \quad (3.9)$$

3.3.2 Cartesian Gradient (∇)

The first derivatives in Cartesian coordinates ($\frac{\partial}{\partial x}, \frac{\partial}{\partial y}, \frac{\partial}{\partial z}$) are produced via the chain rule:

$$\begin{aligned} \frac{\partial \phi}{\partial x} &= \frac{\partial r}{\partial x} \frac{\partial \phi}{\partial r} = \frac{(x - x_j)}{r} \frac{\partial \phi}{\partial r} \\ \frac{\partial \phi}{\partial y} &= \frac{\partial r}{\partial y} \frac{\partial \phi}{\partial r} = \frac{(y - y_j)}{r} \frac{\partial \phi}{\partial r} \\ \frac{\partial \phi}{\partial z} &= \frac{\partial r}{\partial z} \frac{\partial \phi}{\partial r} = \frac{(z - z_j)}{r} \frac{\partial \phi}{\partial r} \end{aligned}$$

where $\frac{\partial \phi}{\partial r}$ for the Gaussian RBFs is given in Equation 3.8.

3.3.3 Cartesian Laplacian (∇^2)

Fasshauer [26] provides the general form of ∇^2 in 2D as:

$$\nabla^2 = \frac{\partial^2}{\partial r^2} \phi(r) + \frac{1}{r} \frac{\partial}{\partial r} \phi(r)$$

For Gaussian RBFs in particular we have the following operators:

- 1D:

$$\nabla^2 = \epsilon^2 (-2 + 4(\epsilon r)^2) \phi(r)$$

- 2D:

$$\nabla^2 = \epsilon^2 (-4 + 4(\epsilon r)^2) \phi(r)$$

- 3D:

$$\nabla^2 = \epsilon^2 (-6 + 4(\epsilon r)^2) \phi(r)$$

which all fit $\nabla^2 = \frac{\partial^2}{\partial r^2} \phi(r) + \frac{d-1}{r} \frac{\partial}{\partial r} \phi(r)$ for dimension d .

3.3.4 Laplace-Beltrami (Δ_S) on the Sphere

The ∇^2 operator can be represented in spherical polar coordinates for \mathbb{R}^3 as:

$$\nabla^2 = \underbrace{\frac{1}{r} \frac{\partial}{\partial r} \left(r^2 \frac{\partial}{\partial r} \right)}_{\text{radial}} + \underbrace{\frac{1}{r^2} \Delta_S}_{\text{angular}},$$

where Δ_S is the Laplace-Beltrami operator—i.e., the Laplacian operator constrained to the surface of the sphere. This form nicely illustrates the separation of components into radial and angular terms.

In the case of PDEs solved on the unit sphere, there is no radial term, resulting in:

$$\nabla^2 \equiv \Delta_S. \quad (3.10)$$

Although this originated in the spherical coordinate system, [100] gives the Laplace-Beltrami operator as

$$\Delta_S = \frac{1}{4} \left[(4 - r^2) \frac{\partial^2 \phi}{\partial r^2} + \frac{4 - 3r^2}{r} \frac{\partial \phi}{\partial r} \right],$$

where r is the Euclidean distance between nodes of an RBF-FD stencil and is independent of our choice of coordinate system.

3.3.5 Constrained Gradient ($P_x \cdot \nabla$) on the Sphere

Following [31, 33], the gradient operator can be constrained to the sphere with this projection matrix:

$$P = I - \mathbf{x}\mathbf{x}^T = \begin{pmatrix} (1 - x_1^2) & -x_1x_2 & -x_1x_3 \\ -x_1x_2 & (1 - x_2^2) & -x_2x_3 \\ -x_1x_3 & -x_2x_3 & (1 - x_3^2) \end{pmatrix} = \begin{pmatrix} P_{x_1} \\ P_{x_2} \\ P_{x_3} \end{pmatrix} \quad (3.11)$$

where \mathbf{x} is the unit normal at the stencil center.

The direct method of computing RBF-FD weights for the projected gradient for $\mathbf{P} \cdot \nabla$ comes from [33]. First, let $\mathbf{x} = (x_1, x_2, x_3)$ be the stencil center Cartesian coordinates, and $\mathbf{x}_k = (x_{1,k}, x_{2,k}, x_{3,k})$ be the coordinates of an RBF-FD stencil node.

Using the chain rule, and assumption that

$$r(\mathbf{x}_k - \mathbf{x}) = \|\mathbf{x}_k - \mathbf{x}\| = \sqrt{(x_{1,k} - x_1)^2 + (x_{2,k} - x_2)^2 + (x_{3,k} - x_3)^2},$$

the unprojected gradient of ϕ becomes

$$\nabla \phi(r(\mathbf{x}_k - \mathbf{x})) = \frac{\partial r}{\partial \mathbf{x}} \frac{\partial}{\partial r} \phi(r(\mathbf{x}_k - \mathbf{x})) = -(\mathbf{x}_k - \mathbf{x}) \frac{1}{r(\mathbf{x}_k - \mathbf{x})} \frac{\partial}{\partial r} \phi(r(\mathbf{x}_k - \mathbf{x})).$$

Applying the projection matrix gives

$$\begin{aligned}
\mathbf{P} \nabla \phi(r(\mathbf{x}_k - \mathbf{x})) &= -(\mathbf{P} \cdot \mathbf{x}_k - \mathbf{P} \cdot \mathbf{x}) \frac{1}{r(\mathbf{x}_k - \mathbf{x})} \frac{\partial}{\partial r} \phi(r(\mathbf{x}_k - \mathbf{x})) \\
&= -(\mathbf{P} \cdot \mathbf{x}_k - 0) \frac{1}{r(\mathbf{x}_k - \mathbf{x})} \frac{\partial}{\partial r} \phi(r(\mathbf{x}_k - \mathbf{x})) \\
&= -(I - \mathbf{x}\mathbf{x}^T)(\mathbf{x}_k) \frac{1}{r(\mathbf{x}_k - \mathbf{x})} \frac{\partial}{\partial r} \phi(r(\mathbf{x}_k - \mathbf{x})) \\
&= \begin{pmatrix} x_1 \mathbf{x}^T \mathbf{x}_k - x_{1,k} \\ x_2 \mathbf{x}^T \mathbf{x}_k - x_{2,k} \\ x_3 \mathbf{x}^T \mathbf{x}_k - x_{3,k} \end{pmatrix} \frac{1}{r(\mathbf{x}_k - \mathbf{x})} \frac{\partial}{\partial r} \phi(r(\mathbf{x}_k - \mathbf{x}))
\end{aligned}$$

Thus, weights for $P_x \cdot \nabla$ can be computed directly by using these three operators on the RHS in Equation 3.3:

$$\begin{aligned}
P \frac{\partial}{\partial x_1} &= (x_1 \mathbf{x}^T \mathbf{x}_k - x_{1,k}) \frac{1}{r(\mathbf{x}_k - \mathbf{x})} \frac{\partial}{\partial r} \phi(r(\mathbf{x}_k - \mathbf{x}))|_{\mathbf{x}=\mathbf{x}_j} \\
P \frac{\partial}{\partial x_2} &= (x_2 \mathbf{x}^T \mathbf{x}_k - x_{2,k}) \frac{1}{r(\mathbf{x}_k - \mathbf{x})} \frac{\partial}{\partial r} \phi(r(\mathbf{x}_k - \mathbf{x}))|_{\mathbf{x}=\mathbf{x}_j} \\
P \frac{\partial}{\partial x_3} &= (x_3 \mathbf{x}^T \mathbf{x}_k - x_{3,k}) \frac{1}{r(\mathbf{x}_k - \mathbf{x})} \frac{\partial}{\partial r} \phi(r(\mathbf{x}_k - \mathbf{x}))|_{\mathbf{x}=\mathbf{x}_j}
\end{aligned}$$

3.3.6 Hyperviscosity Δ^k for Stabilization

The hyperviscosity filter for stabilization is introduced in [39] and was included in our previous investigations in [7]. When explicitly solving hyperbolic equations, differentiation matrices encode convective operators of the form

$$D = \alpha \frac{\partial}{\partial \lambda} + \beta \frac{\partial}{\partial \theta} \quad (3.12)$$

The convective operator, discretized through RBF-FD, has eigenvalues in the right half-plane causing the method to be unstable [31, 39]. Stabilization of the RBF-FD method is achieved through the application of a hyperviscosity filter to Equation (3.12) [39]. By using Gaussian RBFs, $\phi(r) = e^{-(\epsilon r)^2}$, the hyperviscosity (a high order Laplacian operator) simplifies to

$$\Delta^k \phi(r) = \epsilon^{2k} p_k(r) \phi(r) \quad (3.13)$$

where k is the order of the Laplacian and $p_k(r)$ are multiples of generalized Laguerre polynomials that are generated recursively ([39]):

$$\begin{cases} p_0(r) = 1, \\ p_1(r) = 4(\epsilon r)^2 - 2d, \\ p_k(r) = 4((\epsilon r)^2 - 2(k-1) - \frac{d}{2})p_{k-1}(r) - 8(k-1)(2(k-1)-2+d)p_{k-2}(r), \quad k = 2, 3, \dots \end{cases}$$

where d is the dimension. The application of hyperviscosity in Chapter ??, utilizes the operator as a filter to shift eigenvalues and stabilize advection equations on the surface of

the unit sphere. In that case, $d = 2$ can be assumed because individual RBF-FD stencils are viewed as (nearly) lying on a plane. A word of caution: for small N , the diameter of the stencil may not be sufficiently small compared to the radius of the sphere, and hyperviscosity might not work as advertised.

In the case of parabolic and hyperbolic PDEs, hyperviscosity is added as a filter to the right hand side of the evaluation. For example, at the continuous level, the equation solved takes the form

$$\frac{\partial u}{\partial t} = -\mathcal{L}u + Hu, \quad (3.14)$$

where \mathcal{L} is the PDE operator, and H is the hyperviscosity filter operator. Applying hyperviscosity shifts all the eigenvalues of L (the discrete form of \mathcal{L}) to the left half of the complex plane. This shift is controlled by k , the order of the Laplacian, and a scaling parameter γ_c , defined by

$$H = \gamma \Delta^k = \gamma_c N^{-k} \Delta^k.$$

It was found in [31], and verified in our own application, that $\gamma = \gamma_c N^{-k}$ provides stability and good accuracy as a function of N on the unit sphere. It also ensures that the viscosity vanishes as $N \rightarrow \infty$ [31]. In general, the larger the stencil size, the higher the order of the Laplacian required as a filter. This is attributed to the fact that, for convective operators, larger stencils treat a wider range of modes accurately. As a result, the hyperviscosity operator should preserve as much of that range as possible. The parameter γ_c must also be chosen with care and its sign depends on k (for k even, γ_c will be negative and for k odd, it will be positive). If γ_c is too large, the eigenvalues move outside the stability domain of our time-stepping scheme and/or eigenvalues corresponding to lower physical modes are not left intact, reducing the accuracy of our approximation. If γ_c is too small, eigenvalues remain in the right half-plane [31, 39].

Tuned parameters for hyperviscosity are provided in Chapter ??.

3.4 RBF-FD Implementation for Time-dependent PDEs

This section considers at a high level how one leverages RBF-FD to solve PDEs. To simplify in the discussion, consult Algorithm 3.1, which is split into two phases: preprocessing and application. The same processes would be The complexity of each phase can vary based the algorithms utilized for each task.

The Preprocessing phase encompasses tasks such as grid setup/generation, stencil generation and stencil weight calculations. As output the phase produces one or more DMs. Note that Preprocessing is a one time cost: grids, stencils, and DMs can be loaded from disk on subsequent runs to effectively bypass the all cost in this phase.

The algorithm starts by loading/generating a grid. RBF-FD requires only node coordinates, and in some cases an indication of whether nodes are on a boundary. Information on mesh edges/connectivity is optional, but could be used to bypass stencil generation. The QueryNeighbors step forms stencils and constructs a directed adjacency matrix that indicates the connectivity of stencils. Either the grid or the adjacency matrix can be partitioned (see Chapter ??) for distribution across multiple processors in the DecomposeDomain step. Finally, one or more processors operate independently to compute weights and assemble

Algorithm 3.1 A High-Level View of RBF-FD

Preprocessing:

```
{ $x$ } $_{j=1}^N$  = GenerateGrid()
for  $j = 1$  to  $N$  do
    Stencil { $S_{j,i}$ } $_{i=1}^n$  = QueryNeighbors( $x_j$ )
end for
{ $x$ } $_{j=1}^{N_p}$  = DecomposeDomain( $D_{\mathcal{L}}$ , { $x$ } $_{j=1}^N$ )
for  $j = 1$  to  $N_p$  do
    { $w_{j,i}$ } $_{i=1}^n$  = SolveForWeights({ $S_j$ })
     $D_{\mathcal{L}}^{(j)}$  = AssembleDM({ $w_j$ })
end for
```

Application:

```
 $t = t_{min}$ 
while  $t < t_{max}$  do
    { $u'$ } = SolvePDE( $D_{\mathcal{L}}$ , { $u$ })
    { $u$ } = UpdateSolution({ $u$ }, { $u'$ },  $\Delta t$ )
     $t += \Delta t$ 
end while
```

local DMs. The assumption in this work is that grids do not evolve in time, so DMs remain constant for the duration of the phase 2 (Application). In the event of moving nodes, weight calculation and DM assembly would move into the second phase and the method would become a Lagrangian particle method (e.g., [?]).

Once in the Application phase, the constructed DMs are applied to solve a PDE either explicitly (e.g., Equation 3.5) or implicitly (e.g., Equation 3.6). In the case of time-dependent PDEs, RBF-FD is applied the same as any classical FD method with a time-stepping scheme (represented by UpdateSolution). Examples of valid time-schemes include Runge-Kutta, Adams-Bashforth, and Crank Nicholson methods among many others. Based on the choice of time-scheme, one frequently needs multiple iterations through SolvePDE to assemble intermediate solutions that are weighted and combined in the the UpdateSolution step.

In general the performance of RBF-FD hinges on the cost of SolvePDE. This is especially true for time-dependent PDEs where an increase in grid resolution results in proportional increase in the number time-steps to satisfy the CFL condition [?]. Chapter 4 demonstrates that choosing the right algorithms for preprocessing tasks can also directly impact performance SpMV. Beyond this, the choice of stencils and accuracy of weights can impact the overall accuracy of approximation, stability and conditioning of the method. As each of these properties improve, the overall time to solution can decrease thanks to larger stable time-steps, smaller required grid size, and faster convergence.

3.5 Grids

RBF-FD has no requirement for structured grids, or need for a well-refined mesh/lattice to define and limit connectivity between nodes. It functions the same on existing meshes

and randomly generated point clouds; although, the actual node placement can impact accuracy of the method. This functional portability on domains of any shape, dimension, and granularity is a major selling point, and something often out of reach for other methods.

- scattered nodes
 - place samples where they are necessary, not where the grid requires
 - maximize the representation of nodes and minimize interpolation error
 - higher order accuracy than standard

The RBF-FD implementation presented in this work is verified and benchmarked on a number of grids. The following grids are chosen for two reasons: a) to easily construct refinements in 2D/3D for consistent benchmarking and convergence studies, and b) to verify solutions against existing methods. All grids mentioned here are available for public download (see [6]).

Regular Grid. For basic debugging and benchmarking purposes the most natural choice is to start with a regular or Cartesian grid. Equally spaced nodes in multiple dimensions are simple to generate. Additionally, refinements—for scaling benchmarks and convergence tests—are direct subsamples.

In theory, RBF-FD functions the same whether nodes are uniformly spaced or random. However, regular grids do not fully exercise advantages that RBF-FD has over other methods with its ability to operate on scattered nodes. For this reason regular grids are only used here for benchmarking purposes and range in size from $N = 10^3$ to $N = 160^3 = 4,096,000$ nodes.

Maximum Determinant Nodes. Chapter ?? applies RBF-FD to solve PDEs on the unit sphere. For consistency with respect to related investigations (e.g., [35, 39, 42]), the Maximum Determinant (MD) node sets [81, 97] are chosen.

MD node sets were originally utilized by the RBF community due to their success in spherical harmonics interpolation [42]. For spherical harmonics, the seemingly irregular node distributions achieve an order of magnitude higher accuracy compared to regular looking node distributions (i.e., minimum energy nodes) [97]. In similar fashion, RBF methods have been shown to benefit from a subtle irregularity in node locations on the sphere due to the tendency in RBF interpolation to reproduce spherical harmonics interpolants when $\epsilon \rightarrow 0$ [42].

The MD node files are available for download on the authors' web site [96], and range in size from $N = 4$ up to $N=27,556$ nodes on the sphere. Figure 3.3 plots the $N = 4096$ node set to illustrate the irregularity in distribution. Node sets greater than $N=27,556$ are not available. Unlike regular grids, each MD node set is a refinement of the sphere, but not a subdivision, so extending beyond $N=27,556$ nodes would require complete regeneration.

Icosahedral Nodes on the Sphere. Figure 3.4 shows Icosahedral nodes on the sphere. Icosahedral grids are nearly homogenous and isotropic, and have been in use since the 1960s [71]. The grids originate as an icosahedron which is refined by subdividing edges equally and projecting back onto the unit sphere. The direct subdivisions imply that tests on icosahedral grids are true refinements of previous grids (in contrast to MD-nodes). This work tests Icosahedral grids with $N=42$ up to $N=163842$ (i.e., the first through 7th refinements).

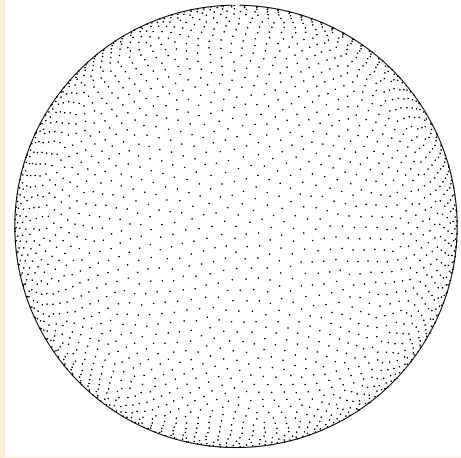


Figure 3.3: Quasi-regular nodes with $N = 4096$ maximum determinant (MD) node sets on the unit sphere.

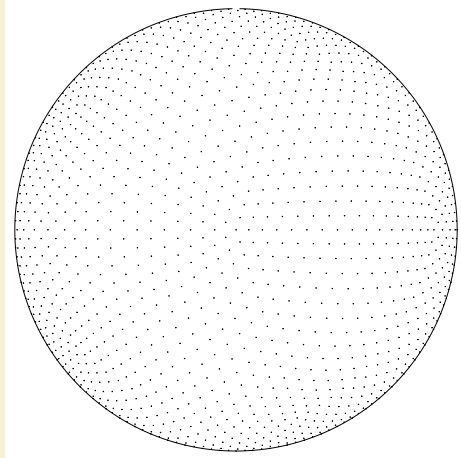


Figure 3.4: $N = 2562$ icosahedral nodes on the unit sphere.

Centroidal Voronoi Tessellations. On the sphere, MD nodes suffice for verification against related work on small to mid size grids (i.e., 30,000 nodes), and Icosahedral grid subdivisions allow for scaling tests and slightly larger mid-sized problems (i.e., 160,000). However, the objective is to scale RBF-FD to large problem sizes that can justify the need for HPC. For this, approximately regular grids on the sphere on the order of millions of nodes are needed. To this end, Spherical Centroidal Voronoi Tessellations (SCVTs) are leveraged to generate high resolution, approximately regular node distributions on the sphere [23, 95].

The process to generate SCVTs involves constructing a Voronoi diagram, computing the mass centroids for each Voronoi partition, and updating node locations to the mass centroids projected onto the sphere. After a number of iterations, the nodes converge to nearly coincide with the projected mass centroids, and the resulting distribution is a SCVT. SCVTs come with a sense of “optimality” in node locations due to energy minimizing

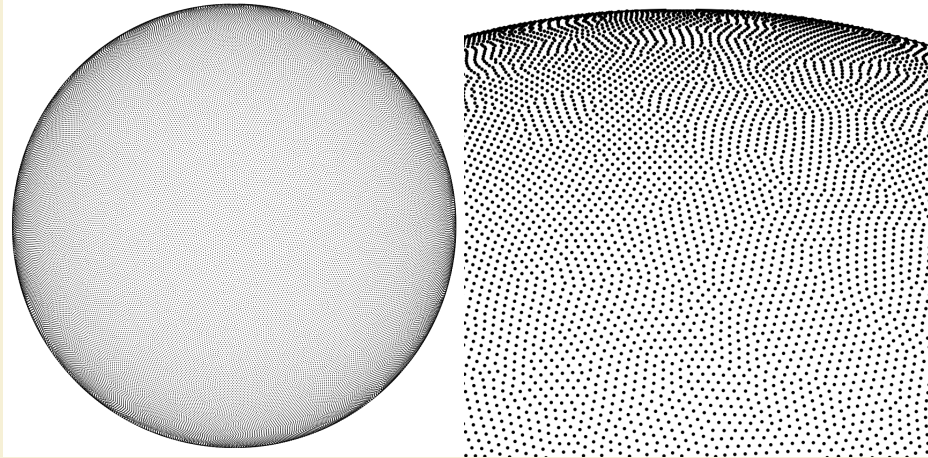


Figure 3.5: (Left) $N=100,000$ Spherical Centroidal Voronoi Tessellation nodes. (Right) Close-up of the same $N=100,000$ nodes to illustrate the irregularities in the grid.

properties (see [23]). In most large-scale applications, the iteration in SCVT generation is a probabilistic Lloyd’s algorithm, with integrals computed through random sampling [23, 95]. While SCVTs in theory converge to a near isotropic node distribution, the probabilistic nature of the centroid calculation introduces irregularities reminiscent of MD nodes.

Figure 3.5 provides an example SCVT grid with $N=100,000$ nodes. On the left, the full sphere; on the right, a close-up of the same node set. The close-up perspective clearly demonstrates the random artifacts/scarring of irregularly distributed nodes. For benchmarking purposes we use node sets $N=100,000$, $N=500,000$ and $N=1,000,000$ generated by the SCVT library from [95].

3.6 On Choosing the Right ϵ

If solving for RBF-Direct weights directly (i.e., inverting Equation 3.3 directly), one must balance the choice of ϵ to avoid ill-conditioning but achieve a reasonable accuracy for the weights. Numerous attempts exist in literature to provide “good” functions for ϵ based on node spacing (h), stencil size (n), and total number of nodes in the domain (N). No fool-proof method exists for RBF-Direct—the “optimal” (in most cases this reads: “acceptable”) value of ϵ depends on the node distribution and varies by application.

This work utilizes a moderately reliable method, proposed in [31], for choosing ϵ . The method expresses ϵ as a function of the grid resolution, N , and the desired mean condition number for Equation 3.3, $\bar{\kappa}_A = \frac{1}{N} \sum_{i=1}^N (\kappa_A)$. Here κ_A is the condition number of the interpolation matrix from Equation 3.3.

The tiles of Figure 3.6 illustrate a number of contours generated in MATLAB. Each contour is numbered according to $\log_{10} \bar{\kappa}_A$. Data was generated by uniformly sampling parameter spaces on ϵ and \sqrt{N} for the MD node-sets. For each $\sqrt{N} = \{40, \dots, 100\}$, in steps of 10, the code makes a sweep through $\epsilon = \{1, \dots, 10\}$ in steps of 0.5 and assembles N RBF-FD interpolation matrices. A call to MATLAB’s “cond()” routine evaluates κ_A for each matrix. The resulting values of $\bar{\kappa}_A$ produce remarkably linear contours, with slopes

that fan out from the ϵ axis. Note that κ_A depends on the stencil size, n , as evidenced by shifting contour fans for $n = 20, 40, 60, 80$, and 100 . The simultaneous increase in slope and decreasing separation between contours leaves little “wiggle” room in guessing ϵ under RBF-Direct.

Regression slope and intercept parameters (c_1 and c_2) are superimposed in Figure 3.6 to aid others in choosing ϵ in new applications. These parameters reproduce contours as $\epsilon(\sqrt{N}) = c_1\sqrt{N} - c_2$. The authors of [31] find condition numbers on the order 10^{10} to 10^{12} to function well for competitive accuracy compared to other methods in literature; the method begins to degrade on large grids (i.e., $N > 1e5$). Similar observations are made in Chapter ??.

Stable weight algorithms like Contour-Padé [99], RBF-QR [19, 38, 42], and RBF-GA [41] can allow RBF-FD to scale beyond the limits of RBF-Direct and will be included in future investigation.

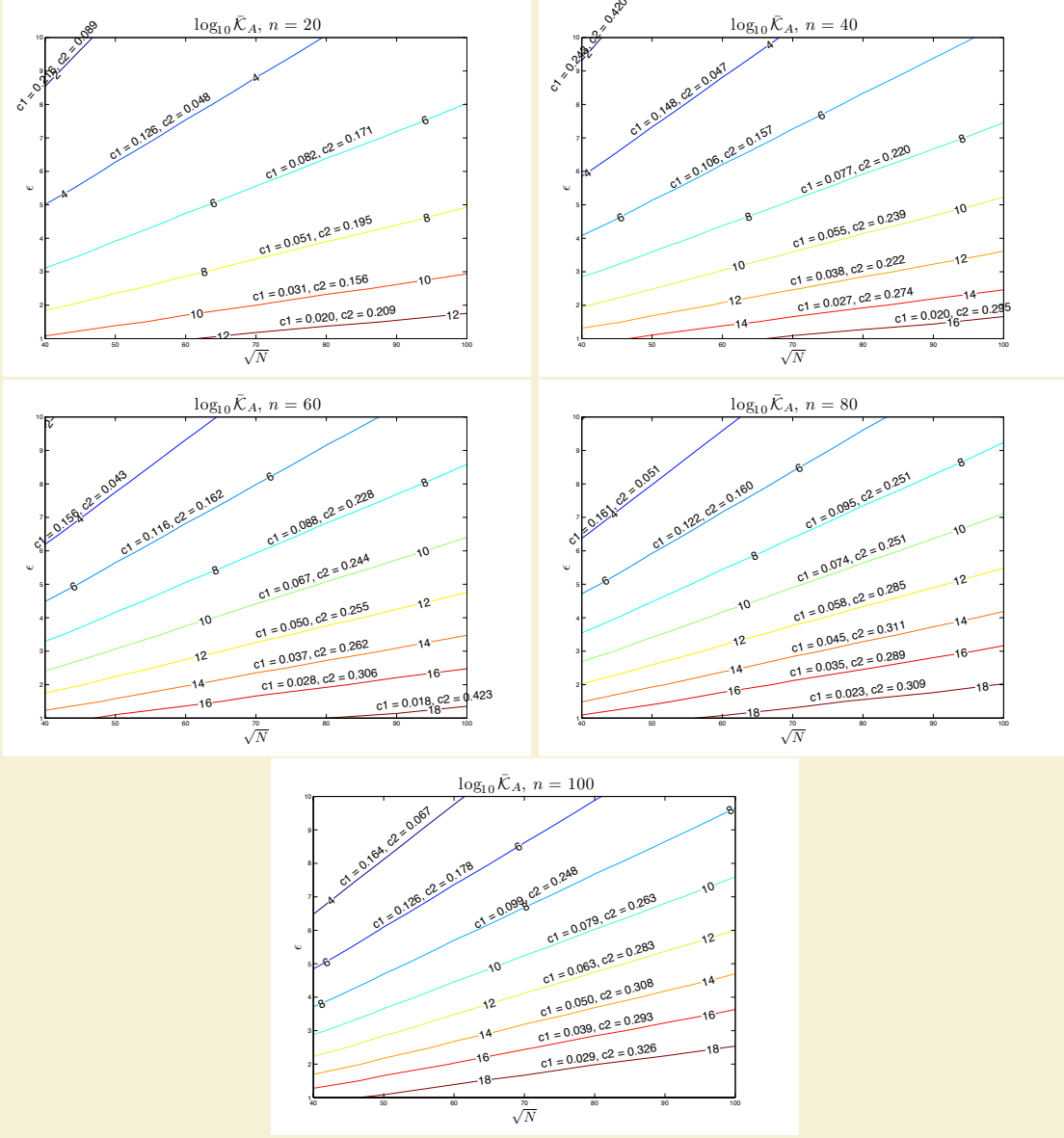


Figure 3.6: Contours for ϵ as a function of \sqrt{N} for stencil sizes $n = 20, 40, 60, 80$ and 100 on the unit sphere. Contours assume near uniform distribution of nodes (e.g., maximum determinant (MD) nodes). Parameters superimposed above each contour provide coefficients for function $\epsilon(\sqrt{N}) = c_1 \sqrt{N} - c_2$.

CHAPTER 4

AN ALTERNATIVE STENCIL GENERATION ALGORITHM FOR RBF-FD

Like all RBF methods, RBF-FD is designed to handle irregular node distributions, and the emphasis in literature focuses on how the method manages point clouds. While nothing prevents implementations of RBF-FD from utilizing existing meshes/lattices, most work in the field concentrates on simple geometries like the sphere [30, 31, 32, 33] and quadrilateral/prism [?] to better understand properties of the method and develop extensions.

Without mesh/lattice connectivity available, stencils are generated by choosing the n -nearest neighbors to each node, including the query node. This is known more formally as a *k-nearest neighbor (k-NN)* problem [85] (a.k.a. ℓ -nearest neighbor search [94]). Here “nearest” is defined with the Euclidean distance metric, although it is possible to generalize to other metrics (see e.g., [1]).

In comparison to the RBF-FD method, global RBF methods with infinite support connect all nodes to all other nodes, so there is no need for neighbor queries. On the other hand, compact RBF methods require all nodes—with no limit on the count—that lie within the support/radius of the RBF centered at each node. This type of neighbor query is referred to as a *ball query* (a.k.a. range query [94]) due to the closed ball created by the radius of support in Equation 2.1.

The *k*-NN and ball query share many similarities, but the former can be harder to solve. Consider, for example, the scenario in Figure 4.1. Two ball queries around a green stencil center are represented as dashed and dash-dot circles. The inner query returns four neighbors, and the outer returns six. If a stencil of size $n = 6$ is desired, then the outer query can be truncated to give the five required neighbors shown in blue. In this example the red node and the farthest blue node are equidistant from the center, and ties are broken arbitrarily. Although *k*-NN is simply a truncated ball query, the real challenge lies in finding the proper search radius to enclose at least the *k* desired neighbors. To find the radius in practice depends on the choice of data structure used to access node locations.

A naïve approach for neighbor queries would be a brute-force search that checks distances from all nodes to every other node. Obviously the cost of such a method is high: $O(N^2)$ for all stencils. Multi-dimensional data structures can limit the scope of searching and reduce the cost of stencil generation to $O(N \log N)$.

For the most part, investigations in RBF communities that delve into efficient neighbor queries are limited to ball queries. For example, the Partition of Unity method for approxi-

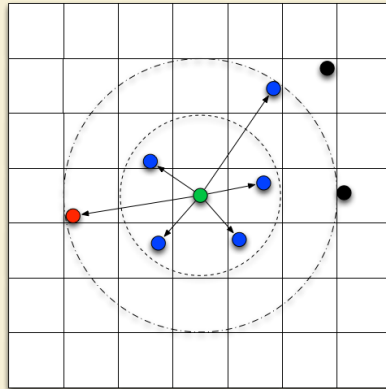


Figure 4.1: A stencil center in green finds neighboring stencil nodes in blue. Two ball queries are shown as dashed and dash-dot circles to demonstrate the added difficulty of finding the right query radius to obtain the k -nearest neighbors.

mation (e.g., [93, 94]), and particle methods like the Fast Multipole Method (e.g., [48, 104]) or Smoothed Particle Hydrodynamics (e.g., [58]). Examples of fast algorithms employed in these fields include the fixed-grid method [58, 94], k -D Trees [94], Range Trees [93, 94], and 2^d -Trees (i.e., Quad- and Octrees) [48, 104]. Surprisingly, while other communities continue the quest for fast neighbor queries, RBF collocation and RBF-FD communities have been slow on the uptake. For many years, the standard in the community has been to use k -D Trees (see e.g., [26, 31, 39]).

This chapter considers the use of an alternative neighbor query algorithm to generate RBF-FD stencils. It is based loosely on the fixed-grid method from [47, 54, 58]. [73] would classify the algorithm as a *fixed grid “bucket” method with one-dimensional spatial ordering*. The fixed-grid method loosens the requirements for finding the k -nearest neighbors (k -NN) stencils to accept k -“approximately nearest” neighbors (k -ANN). It also reorders nodes according to space-filling curves. In what follows, the fixed-grid method is compared to an efficient implementation of k -D Tree available for use in C++ and MATLAB ([85]). Benchmarks demonstrate that, with the proper choice of parameters for the fixed-grid, the method is up to 2x faster than k -D Tree, and it comes with a free bonus: up to 5x faster SpMV due to the impact of spatial reordering that occurs by default during stencil generation.

4.1 k -D Tree

A k -D Tree is a spatial data structure that generally decomposes a space/volume into a small number of cells. All k -D Trees are binary and iteratively subdivide volumes and sub-volumes at each level into two parts. The “ k ” in k -D Tree refers to the dimensionality of the data/volume partitioned—that is $k \equiv d$.

Given a set of points bounded by a d -dimensional volume, a k -D Tree applies a hierarchy of $(d - 1)$ -dimensional axis aligned *splitting planes* to cut the space. At each level of the hierarchy the splitting planes result in two new *half-planes* [80]. Consecutive splits intercept

one another at a *splitting value*. *k-D Trees* do not require that half-planes equally subdivide a volume; more often it is the data contained within the volume that is equally partitioned. The choice of dimension for the splitting plane, in conjunction with a variety of methods for choosing the splitting values allows for many flavors of *k-D Trees* (see e.g., [20, 73, 80] for comprehensive lists). *Point k-D Trees*, 2^d *Trees* (i.e., quad-/octrees), *BSP-Trees*, and *R-trees* are all members of the general *k-D Tree* class [80, 104].

This work considers *Point k-D Trees* [73], which partition a set of discrete points/nodes as outlined by the recursive procedure in Algorithm 4.1. Point *k-D Trees* assume that splitting planes intercept nodes rather than occur arbitrarily along the half-plane. The splitting value at each level of the tree is set to the *median coordinate* of the points in the half-plane, which ensures the tree is well balanced on initial construction. All nodes with coordinate (in the current dimension) less than or equal to the splitting value are contained by the left half-plane, and all nodes with coordinate greater than the splitting value are contained by the right. Half-planes containing only one element correspond to leaves of the tree. The median coordinate of a half-plane is found by sorting the n node coordinates contained by the partition and selecting the $\lceil \frac{n}{2} \rceil$ -th element [20].

Algorithm 4.1 BuildKDTree(P , $depth$)

```

1: Input: A set of  $d$ -dimensional points  $P$  and the current  $depth$ .
2: Output: The root of the k-D Tree for  $P$ .
3:
4: if  $size(P) = 1$  then
5:   return a new leaf storing  $P$ 
6: end if
7:  $L_i := median(coord(P, depth))$ 
8:  $v_l := \text{BuildKDTree}(coord(P, depth) \leq L_i, (depth + 1) \text{ modulo } d)$ 
9:  $v_r := \text{BuildKDTree}(coord(P, depth) > L_i, (depth + 1) \text{ modulo } d)$ 
10: return A new node  $v := \begin{pmatrix} \text{value} := L_i \\ \text{left} := v_l \\ \text{right} := v_r \end{pmatrix}$ 
```

The *k-D Tree* in Figure 4.2 is an example of a Point *k-D Tree*. Given a set of eight nodes in two dimensions, the tree is constructed by applying one-dimensional cuts along the x -dimension, then the y -dimension, then back to the x -dimension. This approach is referred to as *cyclic splitting*, as consecutive cuts are applied by iterating dimensions in a round-robin fashion [73]. The first cut, L_1 , shown in green, splits the nodes into two sets on either side of A . The corresponding tree in the center of Figure 4.2 shows L_1 as the tree root with all nodes having x -coordinates less than or equal to A to the left, and all nodes having x -coordinates greater than A to the right. The second level of the tree, L_2 and L_3 (in blue), splits the half-planes on either side of A at nodes B and C . The axis parallel splits for each half-plane intercept L_1 independently to partition half-planes along the y -dimension; once again, nodes with coordinates less than or equal (i.e., below the cut) to the splitting value branch left in the tree, and y -coordinates greater than (i.e., above) the value branch right. The third level (red) returns to splitting half-planes in the x -dimension. Nodes D and H are not intersected by a splitting plane; their half-planes contain only one

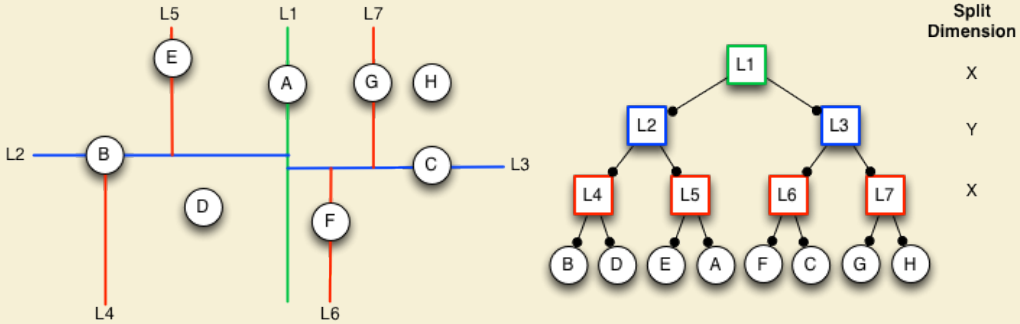


Figure 4.2: An example k -D Tree in 2-Dimensions. Nodes are partitioned with a cyclic dimension splitting rule (i.e., splits occur first in X , then Y , then X , etc.); all splits occur at the median node in each dimension.

node so they immediately become leaves of the tree. This process to build a Point k -D Tree has a complexity of $O(N \log N)$ with $O(N)$ storage required [20, 73].

Frequently, the terms *k -D Tree* and *Point k -D Tree* are used synonymously by the RBF community (see e.g., [26, 31, 39]); the same is convention adopted here.

Generating an RBF-FD stencil with a k -D Tree can be efficiently accomplished in $O(n \log N)$ time—where n is the stencil size—following an approach introduced in [45], and presented in Algorithm 4.2. The k -NN search starts a depth-first recursive search of the k -D Tree to find the nearest neighbor to a query point, X_q . Traversal of the tree occurs by following branches left or right based on comparison of X_q coordinates to the splitting value stored at each node of the tree, with the objective to find the smallest half-plane containing X_q . The search traverses the height of the tree in $O(\log N)$ steps to find the leaf that stores the nearest neighbor to X_q . The neighbor point and its distance from X_q are inserted into a global priority queue, pq . Points in the priority queue are sorted in descending order according to distance.

After finding the nearest neighbor the algorithm returns to the previous node in the tree and onto the opposing half-plane (i.e., down the far branch) to look for other leaves. So long as the size of pq is at less than capacity (n) the search automatically adds points to the priority queue. If pq reaches capacity the algorithm starts to pop off excess points with the understanding that the action removes those points farthest from X_q .

In order to prune branches from the search and reduce complexity, Algorithm 4.2 makes use of a routine called “BoundsOverlapBall”, which checks if any boundaries of the current level half-plane intersect/overlap with a closed ball centered at X_q . The ball is given a radius equal to the maximum distance in pq . Then, if the ball and a boundary intersect, the search will continue onto the half-plane on the opposite side of that boundary. This step handles the possibility that nearer nodes occur within the overlapped region in the other half-plane. If the ball and boundary do not intersect, the opposing half-plane and its related subtree are pruned from the search. Additional details on the implementation of “BoundsOverlapBall” can be found in [45, 86].

The authors of [45] find Algorithm 4.2 capable of efficiently querying the n -nearest neighbors with a complexity proportional to $O(\log N)$ (dominated by the cost of tree traversal).

Algorithm 4.2 KNNSearchKDTree($X_q, n, root, depth$)

- 1: **Input:** A query node X_q , number of desired neighbors (n), the current *root* of the k -D Tree, and the current *depth* of traversal.
- 2: **Output:** A global priority queue, pq , containing the n -nearest neighbors to X_q sorted by distance from X_q in descending order.
- 3: **Assume:** A routine named “BoundsOverlapBall” exists to determine if the boundaries of the current half-plane are intersected by the ball centered at X_q with radius equal to the maximum distance in pq . As long as $pq.size < n$, “BoundsOverlapBall” defaults to true.

- 4:
- 5: **if** *root* is leaf **then**
- 6: Insert $\{root, \text{dist}(X_q, root)\}$ into pq
- 7: **if** $pq.size > n$ **then**
- 8: $pq.pop$ ▷ Keep only n -nearest neighbors
- 9: **end if**
- 10: **return**
- 11: **end if**
- 12:
- 13: **if** $\text{coord}(X_q, depth) \leq root.value$ **then**
- 14: KNNSearchKDTree($X_q, n, root.left, (depth + 1) \% d$)
- 15: **else**
- 16: KNNSearchKDTree($X_q, n, root.right, (depth + 1) \% d$)
- 17: **end if**
- 18:
- 19: **if** $\text{coord}(X_q, depth) \leq root.value$ **then**
- 20: **if** BoundsOverlapBall(X_q) **then**
- 21: KNNSearchKDTree($X_q, n, root.right, (depth + 1) \% d$)
- 22: **end if**
- 23: **else**
- 24: **if** BoundsOverlapBall(X_q) **then**
- 25: KNNSearchKDTree($X_q, n, root.left, (depth + 1) \% d$)
- 26: **end if**
- 27: **end if**
- 28: **return**

The relationship between stencil size n , and grid size, N , is better expressed as $O(n \log N)$ for one stencil.

RBF-FD only needs to generate stencils once, so the overall time for the step subsumes the cost of tree construction and N queries. The resulting overall complexity is proportional to $O(N \log N)$.

4.2 A Fixed-Grid Algorithm

While a k -D Tree functions well for queries, the cost to build the tree structure is unnecessary overhead. Among the many data-structures that exist for nearest neighbor

queries, alternatives like fixed-grid methods [73, 93, 94] (a.k.a. uniform grid [47, 58]) bypass much of the cost in construction with an assumption that only lower spatial dimensions (e.g., 2-D or 3-D) are significant for choosing neighbors. This discards the need to build a tree and shifts focus onto querying neighbors.

Fixed-grid methods get their name from a coarse 2-D or 3-D regular grid that is overlaid on the domain. The d -dimensional grid divides the domain's axis aligned bounding box (AABB)—that is, the minimum bounding box containing the entire domain with edges parallel to axes—into $(h_n)^d$ cells. Subdivisions are uniform, so one can easily identify the cell containing any sample point, p , given the coordinates of the AABB and $(h_n)^d$. For example, let (c_x, c_y, c_z) be the desired containing cell in 3-D, and $(x_{min}, y_{min}, z_{min})$ and $(x_{max}, y_{max}, z_{max})$ be the minimum and maximum coordinates of the AABB (resp.). Then the cell coordinates are found by:

$$(dx, dy, dz) = \left(\frac{(x_{max} - x_{min})}{h_n}, \frac{(y_{max} - y_{min})}{h_n}, \frac{(z_{max} - z_{min})}{h_n} \right)$$

$$(c_x, c_y, c_z) = \left(\left\lfloor \frac{(p_x - x_{min})}{dx} \right\rfloor, \left\lfloor \frac{(p_y - y_{min})}{dy} \right\rfloor, \left\lfloor \frac{(p_z - z_{min})}{dz} \right\rfloor \right). \quad (4.1)$$

Cells neighboring (c_x, c_y, c_z) are trivial to find by adding positive and negative offsets to each coordinate.

Fixed grid methods also make use of *space filling curves*. Space filling curves pass through every point in d -dimensional space, and through each point only once. Equivalently, space filling curves map d -dimensional space down to 1-D, where every point is converted to a unique index or traversal order based on its spatial coordinates. These mapping properties make space filling curves ideal for use as hash functions. Traversing the d -dimensional points (i.e., playing “connect the dots”) draws the space filling curve. Figure 4.3 presents two common orderings of a 2-D fixed-grid. Note that one-dimensional orderings are not unique. On the left is a *Raster*-ordering (a.k.a. Scanline- or *ijk*-ordering): $f(c_x, c_y, c_z) = ((c_x * h_n) + c_y) * h_n + c_z$. The right half of Figure 4.3 shows an ordering known as Morton- or *Z*-ordering. *Z*-ordering construction is discussed later in this chapter. On both sides of Figure 4.3, the lower left corner of each cell indicates the mapped index. Traversing the cells in order produces the curves superimposed in red.

At a high level, fixed-grid methods have the following construction steps [58]:

1. Subdivide the domain with the overlay grid.
2. For each node, identify the containing cell coordinates.
3. For each node, use the cell coordinates as input to a spatial hash function (i.e., a space-filling curve).
4. Sort the nodes according to their spatial hash.

Particular details of how nodes are sorted, the choice of hashing function, the number of nodes allowed per cell, etc. determine the specific class of fixed-grid method and corresponding complexity. A comprehensive list of options and classifications can be found in [73].

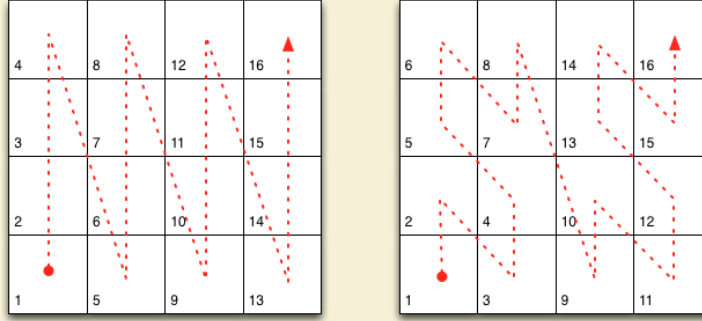


Figure 4.3: Two example space filling curves to linearize the same fixed-grid. Left: Raster-ordering (ijk); Right: Morton-/Z-ordering.

4.2.1 Fixed-grid Construction

The algorithm in this work is inspired by fixed-grid approaches for GPU particle simulations ([47, 54, 58]). Particle methods require a ball query at each time-step. With time-steps often dominated by the cost of querying neighbors, the community understandably devotes significant effort to seek out the most efficient solutions possible. The fixed-grid method is competitive for at least two reasons: a) by bypassing the need to build a tree, half the cost in querying neighbors is avoided; and b) nodes sorted according to a spatial hash reside closer in memory to nearby neighbors than in the case of unsorted nodes. The spatial locality results in a higher likelihood that data will be cached when required. Note that reordering by cell hash sorts nodes across cells but not within them—that is, nodes contained by the same cell are contiguous in memory, but remain arbitrarily ordered with respect one another. Fortunately, with contiguous groups of nodes, nearest neighbor queries can directly access all nodes per cell.

The authors of [47, 54, 58] assume a raster-ordering on cells, and that the uniform grid is sufficiently refined to ensure cells contain at most eight nodes. Particle interactions are limited to ball queries on the containing cell plus one valence of neighboring cells (i.e., 8 surrounding cells in 2-D and 26 cells in 3-D). Since the number of cells to check is fixed, the neighboring nodes can be obtained by direct access in constant time. As a point of difference in implementations, the authors of [47, 58] leverage a fast radix sort algorithm based on hash index to order nodes, while [54] utilizes a slower bitonic sort algorithm. The fixed-grid in [93, 94] forgoes logic to refine the grid and enforce a maximum limit on the number of nodes per cell. The author also avoids sorting nodes based on cell hashes. Instead, a list is maintained for each cell that has the indices of all contained nodes, which implies random memory access when operating on the nodes of a cell.

The implementation presented here is a hybrid of the related algorithms. For example, cells are sorted based on raster-ordering, but without the restriction on max number of nodes per cell. Rather than a radix- or bitonic sort to reorder nodes, the list of node indices for each cell ([93, 94]) is constructed as part of a single-pass bucket sort. Finally, in stark contrast to [47, 54, 58, 93, 94], querying neighbors is not restricted to a fixed number of cell valences. To satisfy the k -NN query, this implementation iteratively increases the query radius to include a new valence of cells at each iteration. This multi-pass ball-query was

demonstrated in Figure 4.1. The iteration terminates when the desired count of neighboring nodes is satisfied or exceeded.

Algorithm 4.3 BuildFixedGrid(P, h_n)

```

1: Input: A set points  $P$ , and the fixed-grid resolution,  $h_n$ .
2: Output: The reordered points in  $P$ , and corresponding cell buckets  $Q$ .
3:
4: Create  $Q$ : an  $(h_n)^d$  array of empty buckets.
5: for point  $p_i$  in  $P$  do
6:    $c := \text{CellCoords}(p_i)$ 
7:    $ind := \text{SpatialHash}(c)$ 
8:   Append index  $i$  onto  $Q[ind]$ 
9: end for
10: for  $j = 0, 1, \dots, (h_n)^d$  do
11:   if  $Q[j]$  is not empty then
12:     Append the set  $P[Q[j]]$  onto  $\hat{P}$ 
13:     Overwrite the set  $Q[j]$  with new indices of  $\hat{P}$ 
14:   end if
15: end for
16:  $P := \hat{P}$ 
17: return

```

Algorithm 4.3 presents the fixed-grid build process. The routine starts with the allocation an array of empty buckets, Q . Next Q is populated based on the spatially hashed cell coordinates. The second for-loop in Algorithm 4.3 iterates through Q , looking for non-empty buckets. When one is found, nodes referenced by that bucket are transcribed/appended onto the “sorted” list of nodes \hat{P} . This way the nodes in each cell are contiguous, but maintain the original ordering with respect to one another. Additionally, node indices in \hat{P} replace the old indices within Q .

The entire build process complexity is proportional to $O(N)$, and requires $O((h_n)^d + N)$ storage. Samet [73] would classify this approach as a *fixed-grid bucket method with one-dimensional ordering*. The term *bucket* refers to the allowance for each cell to contain an arbitrary number of nodes. *One-dimensional ordering* is indicative of attempts later in the chapter to employ alternative space-filling curves in place of raster-ordering.

A special note: the final step of Algorithm 4.3 overwrites the original list of nodes with the sorted equivalent. The spatially sorted list is included in the cost of stencil generation, but available for reuse elsewhere. Since the first step in RBF-FD applications is to generate stencils, overwriting the input node set can guarantee that the node values throughout the entire life-cycle of an RBF-FD application will benefit from the same spatial locality as stencil generation. This benefit is (almost) free.

Consider Figure 4.4, which shows two differentiation matrices generated based on the same $N = 6400$ MD-node set (unit sphere), with each row representing RBF-FD stencils of $n = 50$ non-zeros. The left matrix in Figure 4.4 is generated with stencils queried by a k -D Tree. The k -D Tree maintains the original ordering on P . The matrix on the right of Figure 4.4 is a permuted equivalent of the left matrix with stencils connecting the exact same nodes. In this case, the fixed-grid cells have a raster-based ordering with $h_n = 10$.

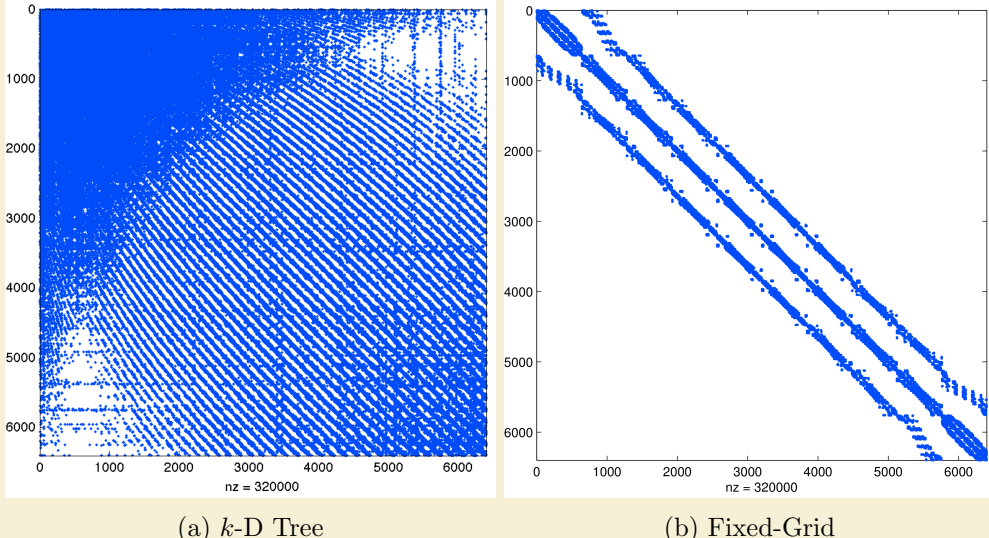


Figure 4.4: Example effects of node reordering for MD node set $N = 6400$ with $n = 50$. The differentiation matrices are permuted equivalents and roughly 0.78% full. a) Stencils generated based on k -D Tree maintain the original node ordering. b) The reordered node set generated using an $h_n = 10$ fixed-grid condenses non-zeros for improved cache effects.

Looking at Figure 4.4 it should be obvious that reordering the nodes can improve memory access patterns for SpMV. If each row is applied as a sparse dot-product with a dense vector, the more condensed non-zeros are in the row, the more likely values from the dense vector will be resident in cache when needed. Later in this chapter, the impact of spatial orderings are compared to determine how RBF-FD can benefit the most.

4.2.2 Fixed-Grid k -NN

Querying the k -nearest neighbors for a single query node X_q is the subject of Algorithm 4.4. The process begins by finding the containing cell, c , for X_q . The hash value of c is used to identify (in Q) the list of nodes contained within that cell, all of which are appended to a vector of neighbor candidates, pq .

It is possible for the number nodes in c to exceed n . However, the algorithm conservatively assumes that it is necessary to search at least one valence of cells around c . This ensures that nodes near the cell boundaries will find nearby neighbors outside of c , and the stencils will balanced.

The query process continues by

launches an iterative process to append the nodes contained within all cells in a valence surrounding the cell containing X_q .

Start at the center cell and add the 8 cells immediately surrounding it. Add to this the 16 cells in the second halo for a total of 25 cells.

So while a k -NN stencil of size $n = 8$ in Figure 4.1 would contain the black node in the right-most column of the grid. The k -ANN generated a stencil of size $n = 8$ would opt for the black node to the top right because it is in the second halo and accepted as “closer”

Algorithm 4.4 QueryFixedGrid(X_q, n, P, Q)

- 1: **Input:** A query point, X_q ; the desired number of neighbors, n ; a set of d -dimensional points P ; and the matching cell bucket list, Q .
- 2: **Output:** The n -nearest neighbors list pq .
- 3:
- 4: $valence := 1$
- 5: $c := \text{CellCoords}(X_q)$
- 6: $ind := \text{SpatialHash}(cells)$
- 7: Append $P[Q[ind]]$ onto pq
- 8: **while** $pq.size < n$ OR $valence < 2$ **do**
- 9: $cells := \text{NeighboringCellCoords}(c, valence)$
- 10: $inds := \text{SpatialHash}(cells)$
- 11: **for** each q in $Q[inds]$ **do**
- 12: **if** q is not empty **then**
- 13: Append node list $P[q]$ onto pq
- 14: **end if**
- 15: **end for**
- 16: increment $valence$
- 17: **end while**
- 18: $dists := \text{ComputeDistances}(pq)$
- 19: Sort pq by $dists$
- 20: **return** the first n nodes in pq

because the stencil can be satisfied without querying the extra 24 cells on the outermost halo.

Therefore, it is not essential that stencils contain only nearest neighbors. Instead, one can acquire the *approximate nearest neighbors*. Figure ?? demonstrates a case where a does not contain all nearest neighbors. As illustrated in the Figure, the ANN stencil and true nearest neighbor stencil differ by one node. THis is not dire

The query is approximate because nodes such as the white node in Figure 4.1 could be included in the stencil before

4.2.3 Orderings

The ideal differentiation matrix, corresponding to discretization of a line, would have all non-zeros on the first $\frac{n-1}{2}$ to each side of the diagonal. For 2- or 3-D domains the ideal case is not possible to achieve, but the nodes can be reordered with the goal to condense At the end of BuildFixedGrid the original set of nodes, P is overwritten by \hat{P} . While nothing requires that \hat{P} replace the usage of P

4.2.4 Performance

Although RBF-FD only requires neighbor queries once, the results that follow reveal a long lasting positive impact on memory with a fixed-grid method, which is sufficient to justify its use. Investigations into moving node coordinates and/or local refinements for RBF methods (e.g., [30]) would find the fixed-grid method significantly more beneficial. As

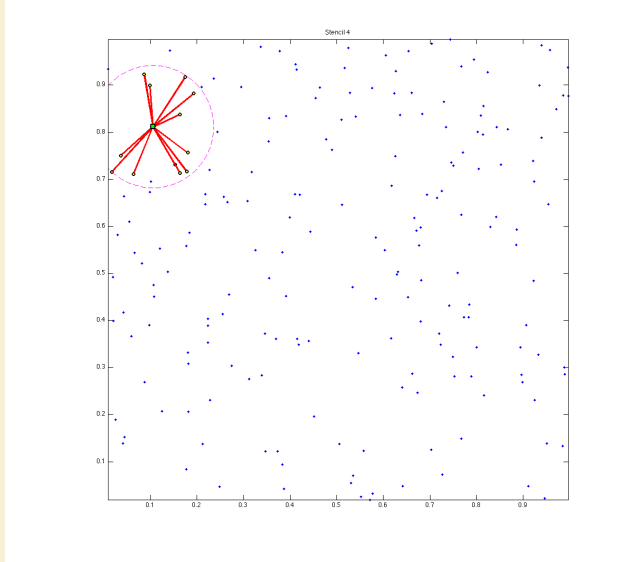


Figure 4.5: A stencil generated with k -ANN satisfies the required stencil size, but is not guaranteed to choose the true nearest neighbors.

of this writing no known applications of RBF-FD consider moving nodes

Due to the limited significance of stencil generation under RBF-FD, the overhead in implementing and debugging the fixed-grid method on the GPU is difficult to justify. The implementation tested here was developed as a pure CPU prototype with minimal attention to optimization. The added complexity in reproducing the efficient fixed-grid method on the GPU could be the subject of future work for moving nodes.

[58] assumes that at each time-step a new virtual fixed grid is generated

Implementations of fixed-grid often assume that no more than two nodes reside in any one cell.

This implementation is CPU only. Porting the one time stencil generation to the GPU was seen as

use of fixed-grid methods originated due to low overhead before performing queries. Although all three related works focus on offloading simulations to the GPU, the method is also popular for CPU implementations

In [93] and later [94], Wendland presents the fixed-grid method as a low-cost alternative for RBF methods based on Partition of Unity.

[70] adopt the a similar approach that incrementally grows the

Following [73], the method used in this work is classified as a fixed-grid *bucket* method with one dimensional ordering. The emphasis on bucket arises from the application of a coarse grid that allows

Examples include *Z*- or *Morton* ordering, *U*- or *Greycodes*-ordering, *X*-ordering, etc. Hilbert curves have been demonstrated to be the most efficient [?].

The algorithm chosen for this work is provided in Algorithm ???. The algorithm starts by creating a list of lists representing the $(h_n)^d$ cells. As nodes are matched with cell indices, the node index is appended to the

These tests assume $dx = dy = dz$ to ensure spherical stencils.

The implementation runs entirely on the CPU ([58] runs on the GPU).

The k -D tree implementation compared in this work is the *kd-Tree Matlab* library from Tagliasacchi [85, 86]. Originally posted to the Matlab FileExchange and now maintained as a Google Code project. Until the addition of *KNNsearcher* in Matlab

garnered attention due to its MEX compiled interface that allowed use as both a C++ and MATLAB library. The Matlab central k -D Tree is MEX compiled and efficient. We integrated the standalone C++ code into our library.

Tagliasacchi [86] uses the standard split by median in each dimension, with alternating chosen by incrementing the dimension by one, modulo the number of dimensions (e.g., in 2D the order is X, Y, X, Y, \dots). Wendland [94] suggests a number of more advanced median cuts such as

[85]. [1]

4.2.5 Integer Dilation and Node Reordering

[64] found that reordering nodes via RCM and space filling curves offer similar benefits in terms of reduced TLB misses and better cache coherency.

[73] labels this type of algorithm as a *fixed grid bucket algorithm* with the twist that it also has *one dimensional ordering*

4.3 Performance Comparison

At the start of this dissertation, the most widely used k -D Tree implementation in the RBF community was [85]. As a MEX-compiled

- Performance improvement
- SpMV impact
- impact from space filling curves

Many algorithms exist to query the k -nearest neighbors (equivalently all nodes in the minimum/smallest enclosing circle). Some algorithms overlay a grid similar to Locality Sensitive Hashing and query such as... [?].

For the purpose of generating RBF-FD stencils the k D-Tree is built and all queries are made once. There is no reuse of the tree so the build and query times are combined into one.

impact from ordering on matrix sparsity. Bandwidth impact. Bandwidth impact on condition considered in future chapter.

what is best overlay resolution? based on time to generate. choose resolution as $n/2$, $n/9$? etc?

perform neighbor queries on raster order because its easiest to jump cells. then each cell can be reordered according to z,x,u, etc. for better memory locality. Matlab script to do this (can be ported to C)

http://www.vincentgarcia.org/data/Garcia_2010_ICIP.pdf

GPU version of Locality Sensitive Hashing could reduce complexity further [69]

This can be done efficiently using neighbor query algorithms or spatial partitioning data-structures such as Locality Sensitive Hashing (LSH) and k D-Tree. Different query algorithms often have a profound impact on the DM structure and memory access patterns. We choose a Raster (ijk) ordering LSH algorithm [?] leading to the matrix structure in Figures ?? and ?. While querying neighbors for each stencil is an embarrassingly parallel operation, the node sets used here are stationary and require stencil generation only once. Efficiency and parallelism for this task has little impact on the overall run-time of tests, which is dominated by the time-stepping. We preprocess node sets and generate stencils serially, then load stencils and nodes from disk at run-time. In contrast to the RBF-FD view of a static grid, Lagrangian/particle based PDE algorithms promote efficient parallel variants of LSH in order to accelerate querying neighbors at each time-step [46, 69].

At the onset of our work on RBF-FD, the most commonly used KDTree implementation used by the RBF community was [?]. Recently, improvements were made to the KDTree algorithm to reduce the cost of building the KDTree to $O(N \log^2 N)$.

Figure ?? compares the total time to generate N stencils of size $n = 50$ with three methods: [?], our hash-based neighbor query, and the improved KDTree from [?]. Until the new release of KDTree, our algorithm was a major improvement to the performance of stencil generation. The hash-based approach achieved greater than

Our work in [7] leveraged an alternative to k -D tree, based loosely on space-filling curve orderings common in Lagrangian schemes like Smoothed Particle Hydrodynamics (e.g., [?], [?]).

4.3.1 Future Work

[?] introduce a minimal k -D Tree for the GPU which

The complexity of the method is still higher than the more efficient implementations used by Lagrangian methods, but as demonstrated in Figure ?? the savings are significant. Generating stencils for RBF-FD is a preprocessing cost, so we do not dedicate an excessive amount of attention to this algorithm. However, a few ideas that would improve: hilbert ordering, choose AABB resolution based on N not user parameters, faster sorting, GPU implementation

RBF-FD operates on general node distributions. Historically, stencils are uniform in size (n) and generated by selecting the $(n - 1)$ true nearest neighbors to a node x_c . This is a k -NN query.

Alternative queries are possible: ball query and approximate nearest neighbor. The approximate is of particular interest because nodes closest to the stencil will always be selected, whereas the nodes further away have minimal influence so swapping out cant hurt. The justification in altering the selection is for reduced complexity in neighbor queries.

4.3.2 Hashing

[14] provide a fast parallel

[?] is working on parallel generation. [?] has OpenCL neighbor queries

We started with a CPU implementation to test appropriateness.

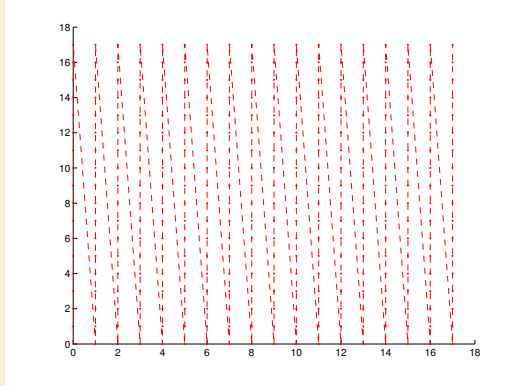


Figure 4.6: In order: a) node ordering test cases; b) original ordering of regular grid (raster); c) coarse grid overlay for hash functions ($hnx = 6$); d) example stencil ($n = 31$) spanning multiple Z's; e) spy of DM after orderings. **Author's Note:** [REGENERATE FIGURES WITH RANDOM/HALTON NODES](#)

Approximate nearest neighbors will be nearly balanced. We observe that RBF-FD functions as well on stencils of true nearest neighbors as it does on approximate nearest neighbors.

To demonstrate the savings in choice of stencil generation method, we provide Figure ??.

The impact of our neighbor query also extends influence on the structure of the RBF-FD DMs. has is to To quantify the sparsity of a Differentiation Matrix we consider the ratio of non-zeros ($N * n$) to total elements in the matrix (N^2). For example, a problem of size $N = 10,000$ with stencil size $n = 31$ has a ratio of 0.0031 and is 99.69% empty.

Querying neighbors requires searching at least the immediate cell one layer of neighbors. by including one extra layer we ensure that small stencils near the border of the immediate cell can pick up neighbors in adjacent cells.

A prototype implementation of this method allowed for a variety of space filling curves to reorder the cells. The curves are created through integer dilation [?]

The KDTree implementation used in this work is from

Original data showed our algorithm as wildly successful against a version

The Cuthill McKee algorithms can be equated to a breadth-first search. The algorithm queues nodes in order of degree at each level of the search and traverses the lowest degree priority. The Reverse variant of Cuthill-McKee inverts the node order so that the lowest degree and top level node are at the end of the matrix rather than the beginning. Aside from ordering, the Reverse and Standard Cuthill McKee algorithms are identical processes. RCM is the more popular of the variants though, due to storage savings and reduced fill-in for some decompositions [62]. .

Obviously, the ideal case for bandwidth is when all rows contain the $\frac{n}{2}$ nodes corresponding to solution value to either side of u_j . In 1-D this corresponds to every node containing the $\frac{n}{2}$ nodes to the left and right of x_j . In 2-D this is only possible if the nodes in the domain are properly indexed such that stencils contain the proper set of neighbors—a stringent requirement that will

The early implementation of k -D tree had an $O(n^2)$ growth in complexity. This algo-

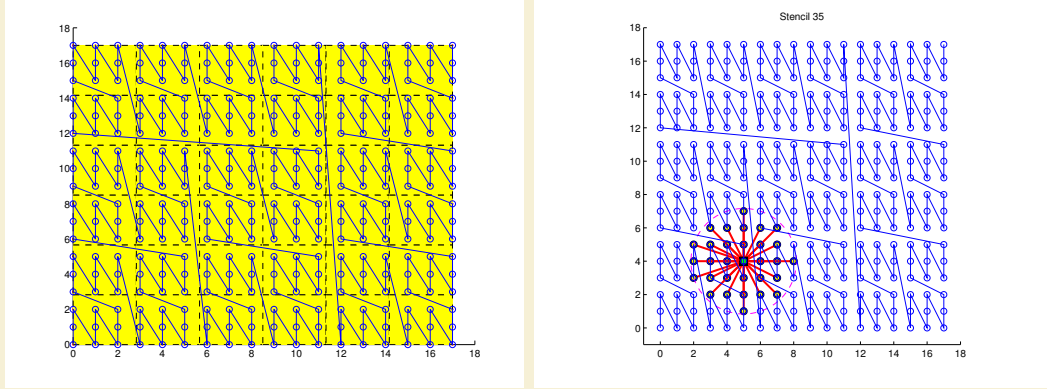


Figure 4.7: In order: a) node ordering test cases; b) original ordering of regular grid (raster); c) coarse grid overlay for hash functions ($hnx = 6$); d) example stencil ($n = 31$) spanning multiple Z's; e) spy of DM after orderings.

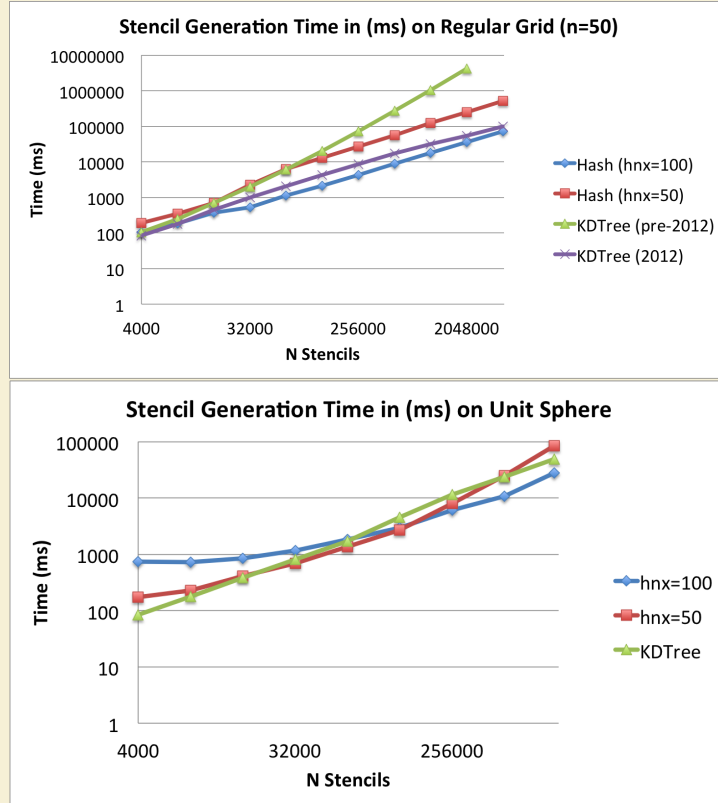


Figure 4.8: Querying the $n = 50$ nearest neighbors on a regular grid up to $N = 160^3$ demonstrates the significant gains achieved by our spatially binned neighbor query. While KDTTree queries grow as $O(N \log N)$

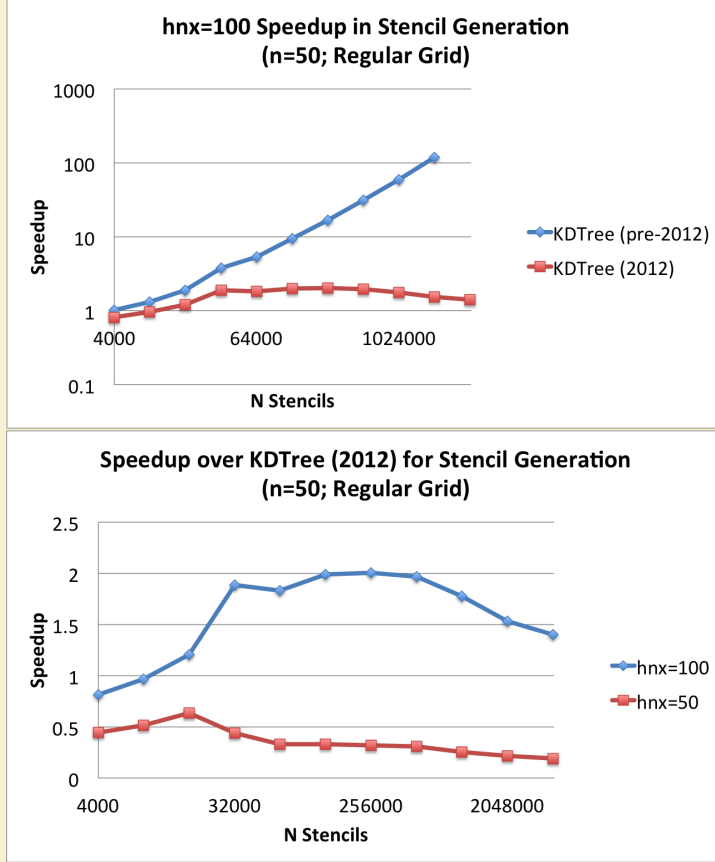


Figure 4.9: Querying the $n = 50$ nearest neighbors on a regular grid up to $N = 160^3$ demonstrates the significant gains achieved by our spatially binned neighbor query. While KDTTree queries grow as $O(N \log N)$

rithm was developed to alleviate that cost. It took a few hours to implement but has had some surprising impacts. Note that the complexity of k -D tree was reduced to $O(N \log^2 N)$ in 2012. On a regular grid (generated with raster/IJK ordering), the cost of k -D tree grows at the same rate as the hashing method.

At $N = 32000$ the cost of hashing drops below k -D Tree due to the decreasing number of empty hash cells. Likewise, at $N = 1000000$ and beyond, the gap between hashing and k -D Tree begins to close as cells contain more than one

Q: why does the curve drop for $hnx = 100$? Q: the complexity of the algorithm? Q: the sphere I understand: its localizing the search to small patches on the sphere, and

For every N there is an optimal hnx . This is depicted for $N = 500000$ CVT and $hnx = 100$.

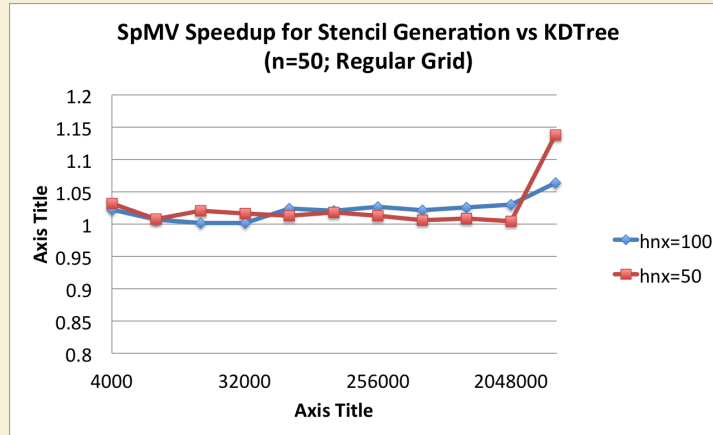


Figure 4.10: Querying the $n = 50$ nearest neighbors on a regular grid up to $N = 160^3$ demonstrates the significant gains achieved by our spatially binned neighbor query. While KDTree queries grow as $O(N \log N)$

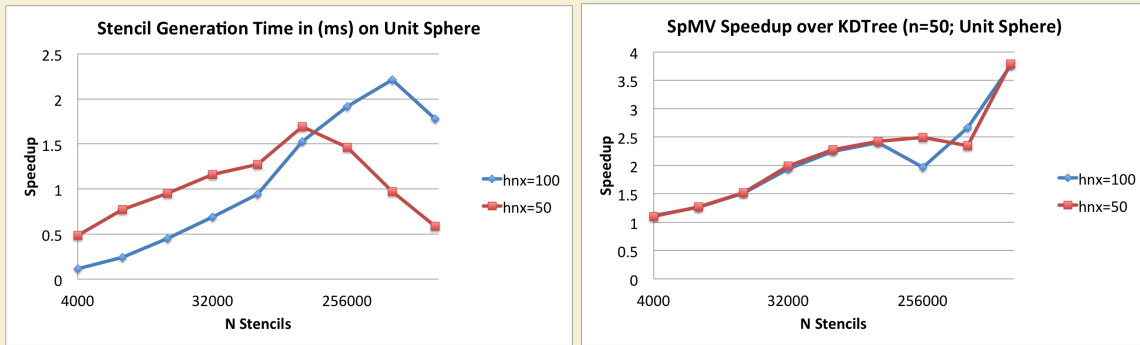


Figure 4.11: Generating stencils for increasing subsets of the $N = 1e6$ CVT nodes mesh.

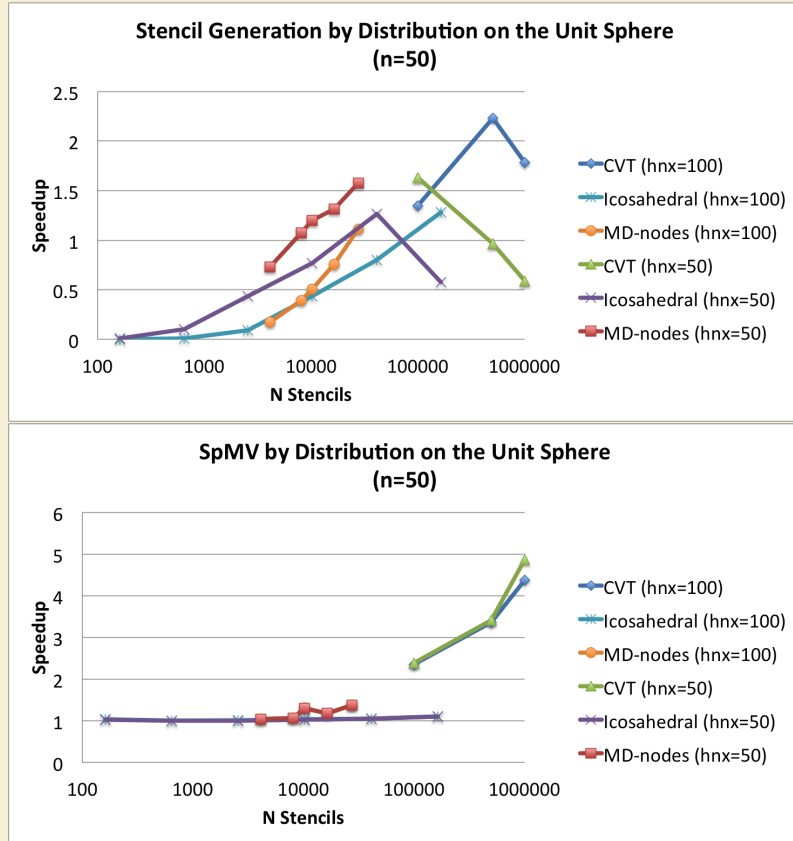


Figure 4.12: Based on the proper choice of overlay resolution, the hash stencil query can accelerate stencil generation, but the sophistication of the algorithm is low enough that negative impact is more likely. On the other hand, the impact on SpMV performance is always positive with the routine accelerated up to 4.9x faster.

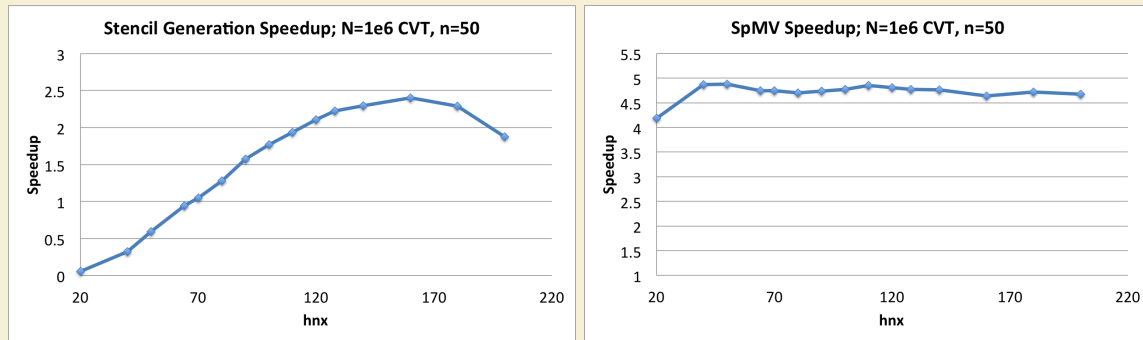


Figure 4.13: As the coarse grid resolution increases the hashing algorithm achieves both 2x faster than KDTree in stencil generation, with greater than 4x gain in SpMV performance (for free).

4.4 On Space Filling Curves and Other Orderings

4.4.1 Integer Dilation

One frequently hears that ordering via space filling curves like Morton Ordering and/or gray codes can benefit memory access patterns.

(Related? <http://publish.uwo.ca/~shaque4/presentationSONAD.pdf> <http://www.cs.duke.edu/~alvy/papers/sc98/> <http://www.cs.indiana.edu/~dswise/Arcee/Papers/medea06.pdf> <http://citeseerx.ist.psu.edu/viewdoc/download?doi=10.1.1.118.7720&rep=rep1&type=pdf> <http://stackoverflow.com/questions/4260002/benefits-of-nearest-neighbor-search>)

[72] mentions the impact of ordering on conditioning.

Algorithms like Reverse Cuthill McKee and Approximate Minimum Degree ordering allow general restructuring of matrices.

Author's Note: [NEed to compare conditioning of LSH and other algorithms in Matlab](#)

Q: what is an ideal ordering? Q: what is the best conditioning from ordering? Q: what is the relative cost of ordering?

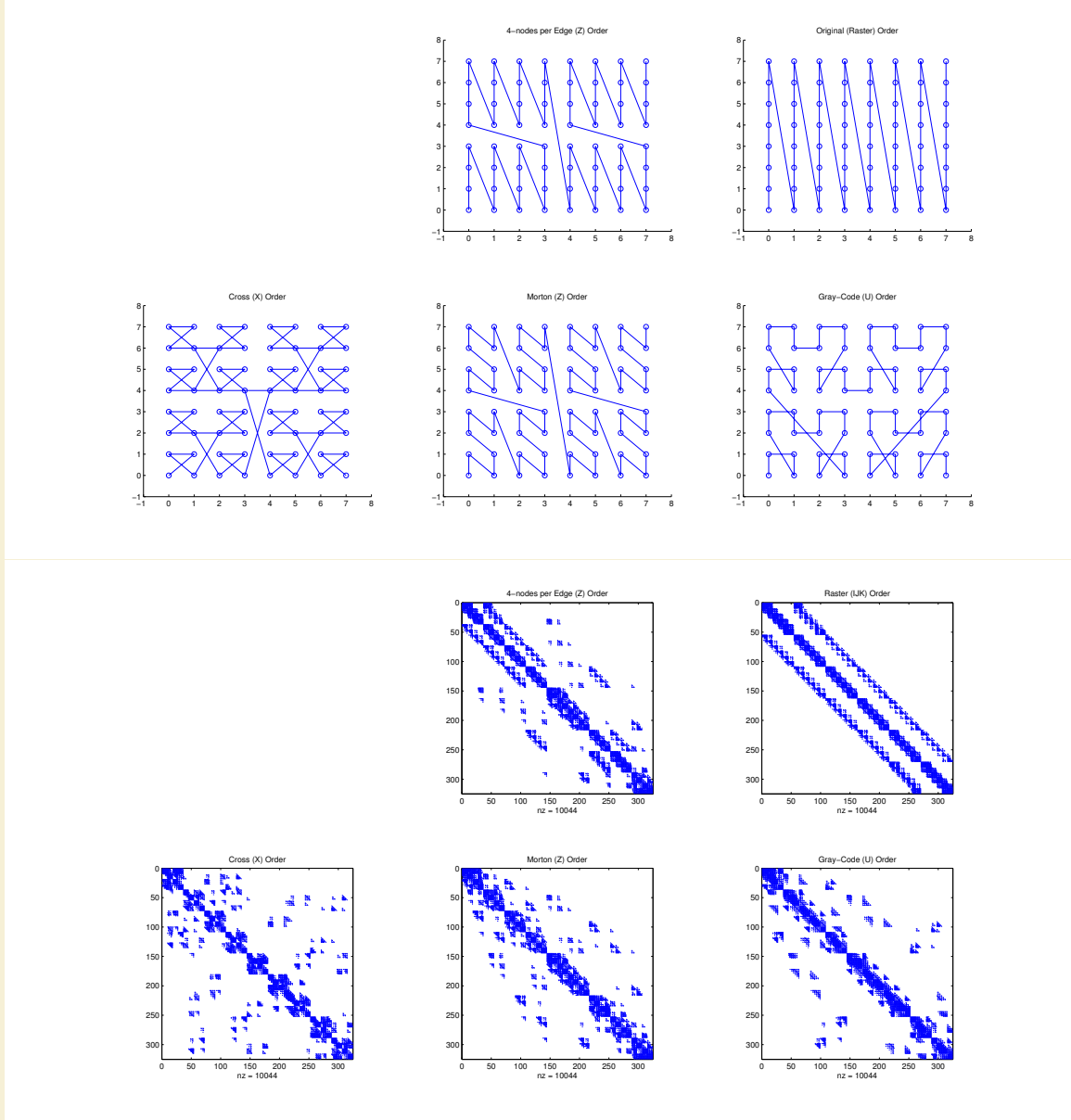


Figure 4.14: In order: a) node ordering test cases; b) original ordering of regular grid (raster); c) coarse grid overlay for hash functions ($hnz = 6$); d) example stencil ($n = 31$) spanning multiple Z's; e) spy of DM after orderings. Author's Note: [TODO: Raster on top left. Add RCM ordering to top right.](#)

4.5 Conclusions on Stencil Generation

For quasi-regular distributions and small to medium sized grids the k -D Tree performs well enough in comparison to the fixed-grid method. However, the difference in There is an ideal hn .

CHAPTER 5

NUMERICAL VALIDATION

with the goal of solving coupled fluid flows modelling the physics (?) in the interior of the earth. We require both advective terms and diffusive terms. The components of a good pressure fluid solver are explicit and implicit differentiation. Whether we solve a steady-state PDE implicitly or a hyperbolic PDE with an implicit time-scheme, we require an *implicit solver*. An implicit solver is nothing but a method of assembling a differentiation matrix, forcing terms on the RHS and then solving the linear system. A direct LU factorization would suffice if our system is dense, but with RBF-FD the system is sparse. Sparse systems can be efficiently solved under the right conditions through sparse iterative solvers. :

Here, we present the first results in the literature for parallelizing RBF-FDs on multi-CPU and multi-GPU architectures for solving PDEs. To verify our multi-CPU, single GPU and multi-GPU implementations, two hyperbolic PDEs on the surface of the sphere are tested: 1) vortex roll-up [67, 68] and 2) solid body rotation [53]. These tests were chosen since they are not only standard in the numerical literature, but also for the development of RBFs in solving PDEs on the sphere [30, 32, 38, 43]. Although any ‘approximately evenly’ distributed nodes on the sphere would suffice for our purposes, maximum determinant (MD) node distributions on the sphere are used (see [81] for details) in order to be consistent with previously published results (see e.g., [32] and [39]). Node sets from 1024 to 27,556 are considered with stencil sizes ranging from 17 to 101.

All results in this section are produced by the single-GPU implementation. Multi-CPU and multi-GPU implementations are verified to produce these same results. Synchronization of the solution at each time-step and the use of double precision on both the CPU and GPU ensure consistent results regardless of the number and/or choice of CPU vs GPU. Eigenvalues are computed on the CPU by the Armadillo library [74].

5.0.1 Vortex Rollup

The first test case demonstrates vortex roll-up of a fluid on the surface of a unit sphere. An angular velocity field causes the initial condition to spin into two diametrically opposed but stationary vortices.

The governing PDE in latitude-longitude coordinates, (θ, λ) , is

$$\frac{\partial h}{\partial t} + \frac{u}{\cos \theta} \frac{\partial h}{\partial \lambda} = 0 \quad (5.1)$$

where the velocity field, u , only depends on latitude and is given by

$$u = \omega(\theta) \cos \theta.$$

Note that the $\cos \theta$ in u and $1/\cos \theta$ in (5.1) cancel in the analytic formulation, so the discrete operator approximates $\omega(\theta) \frac{\partial}{\partial \lambda}$.

Here, $\omega(\theta)$ is the angular velocity component given by

$$\omega(\theta) = \begin{cases} \frac{3\sqrt{3}}{2\rho(\theta)} \operatorname{sech}^2(\rho(\theta)) \tanh(\rho(\theta)) & \rho(\theta) \neq 0 \\ 0 & \rho(\theta) = 0 \end{cases}$$

where $\rho(\theta) = \rho_0 \cos \theta$ is the radial distance of the vortex with $\rho_0 = 3$. The exact solution to (5.1) at non-dimensional time t is

$$h(\lambda, \theta, t) = 1 - \tanh\left(\frac{\rho(\theta)}{\gamma} \sin(\lambda - \omega(\theta)t)\right),$$

where γ defines the width of the frontal zone.

From a method of lines approach, the discretized version of (5.1) is

$$\frac{d\mathbf{h}}{dt} = -\operatorname{diag}(\omega(\theta)) D_\lambda \mathbf{h}. \quad (5.2)$$

where D_λ is the DM containing the RBF-FD weights that approximate $\frac{\partial}{\partial \lambda}$ at each node on the sphere.

For stability, hyperviscosity is added to the right hand side of (5.2) in the form given in (3.14). The scaling parameter γ_c and the order of hyperviscosity k are given in Table 5.1. The goal when choosing k is to damp the higher spurious eigenmodes of $\operatorname{diag}(\omega(\theta)) D_\lambda$ while leaving the lower physical modes that can be resolved by the stencil intact. In this process, the eigenvalues will be pushed into the left half of the complex plane. Then, γ_c is used to condense the eigenvalues as near to the imaginary axis as possible. Figure 5.1b shows the effect of hyperviscosity on the eigenvalues of the DM, $-\operatorname{diag}(\omega(\theta)) D_\lambda$, in (5.2).

In order to scale to large node sets, the RBF shape parameter, ϵ , is chosen such that the mean condition number of the local RBF interpolation matrices $\bar{\kappa}_A = \frac{1}{N} \sum_{j=1}^N (\kappa_A)_j$ is kept constant as N increases ($(\kappa_A)_j$ is the condition number of the interpolation matrix in (??), representing the j^{th} stencil). For a constant mean condition number, ϵ varies linearly with \sqrt{N} (see [31] Figure 4a and b). This is not surprising since the condition number strongly depends on the quantity ϵr , where $r \sim 1/\sqrt{N}$ on the sphere. Thus, to obtain a constant condition number, we let $\epsilon(N) = c_1 \sqrt{N} - c_2$, where c_1 and c_2 are constants based on [31].

Figure 5.2 shows the solution to Equation (5.1) at $t = 10$, on $N = 10201$ nodes, with stencil size $n = 50$. This resolution is sufficient to properly capture the vortices at $t = 10$, but lower resolutions would suffer approximation errors associated with insufficient grid resolution. For this reason, the solution at $t = 3$ is considered in the normalized ℓ_2 error convergence study presented in Figure 5.3. The time step $\Delta t = 0.05$ for all resolutions.

Author's Note: Include older figures of convergence without stabilization. Mention that CVT nodes require independent tuning of HV param. Its useful but not incredibly convenient at the moment.

Table 5.1: Values for hyperviscosity and the RBF shape parameter ϵ for vortex roll-up test.

Stencil Size (n)	$\epsilon = c_1\sqrt{N} - c_2$		$H = -\gamma_c N^{-k} \Delta^k$	
	c_1	c_2	k	γ_c
17	0.026	0.08	2	8
31	0.035	0.1	4	800
50	0.044	0.14	4	145
101	0.058	0.16	4	40

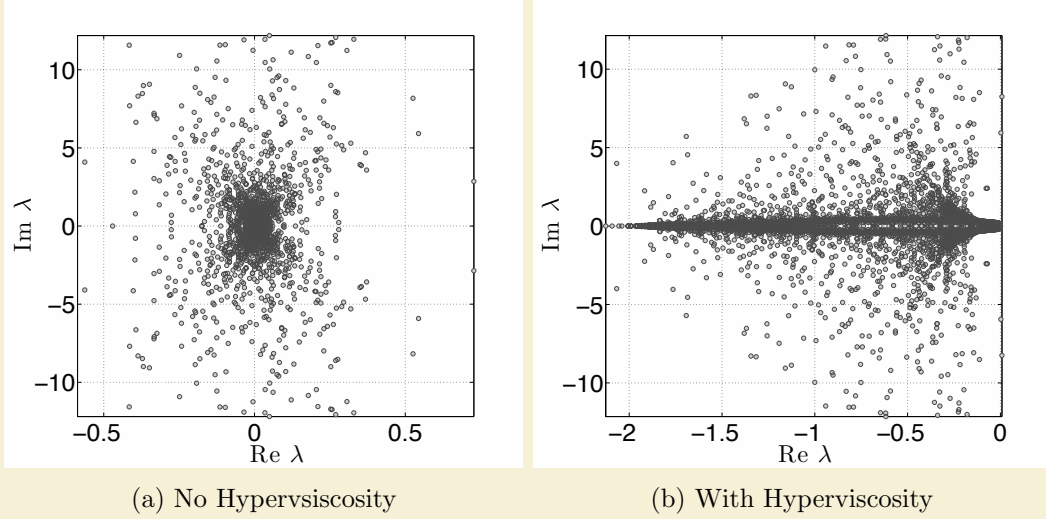


Figure 5.1: Eigenvalues of $\text{diag}(\omega(\theta))D_\lambda$ for the vortex roll-up test case for $N = 4096$ nodes, stencil size $n = 101$ and $\epsilon = 3.5$. Left: no hyperviscosity. Right: hyperviscosity enabled with $k = 4$ and $\gamma_c = 40$. [Author's Note: color](#)

5.0.2 Solid body rotation

The second test case simulates the advection of a cosine bell over the surface of a unit sphere at an angle α relative to the pole of a standard latitude-longitude grid. The governing PDE is

$$\frac{\partial h}{\partial t} + \frac{u}{\cos \theta} \frac{\partial h}{\partial \lambda} + v \frac{\partial h}{\partial \theta} = 0, \quad (5.3)$$

with velocity field,

$$\begin{cases} u = u_0(\cos \theta \cos \alpha + \sin \theta \cos \lambda \sin \alpha), \\ v = -u_0(\sin \lambda \sin \alpha) \end{cases} .$$

inclined at an angle α relative to the polar axis and velocity $u_0 = 2\pi/(1036800 \text{ seconds})$ to require 12 days per revolution of the bell as in [32, 68].

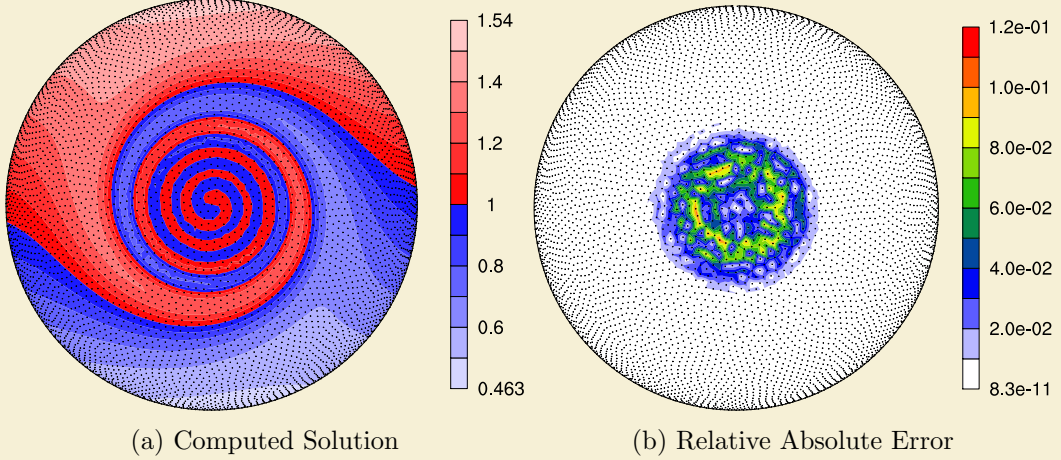


Figure 5.2: Vortex roll-up solution at time $t = 10$ using RBF-FD with $N = 10, 201$ and $n = 50$ point stencil. Normalized ℓ_2 error of solution at $t = 10$ is $1.25(10^{-2})$ [Author's Note: add initial condition figure](#)

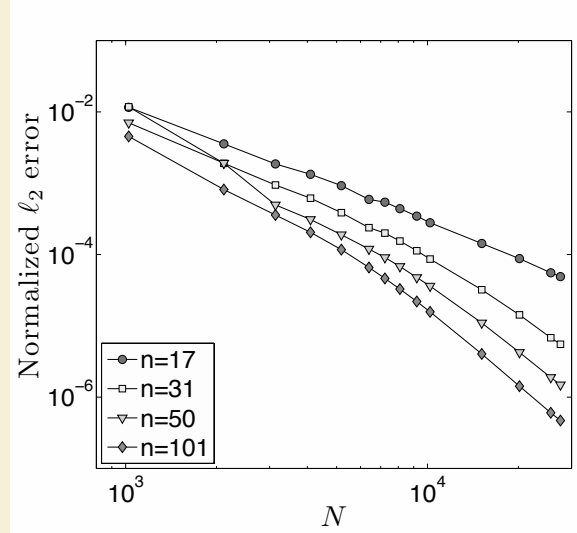


Figure 5.3: Convergence plot for vortex roll-up at $t = 3$. [Author's Note: color](#)

The discretized form of (5.3) is

$$\frac{d\mathbf{h}}{dt} = -\text{diag}\left(\frac{u}{\cos \theta}\right) D_\lambda \mathbf{h} - \text{diag}(v) D_\theta \mathbf{h} \quad (5.4)$$

where DMs D_λ and D_θ contain RBF-FD weights corresponding to all N stencils that approximate $\frac{\partial}{\partial \lambda}$ and $\frac{\partial}{\partial \theta}$ respectively. Rather than merge the differentiation matrices in (5.4) into one operator, our implementation evaluates them as two sparse matrix-vector multi-

plies. The separate matrix-vector multiplies are motivated by an effort to provide general and reusable GPU kernels. Additionally, they artificially increase the amount of computation compared to the vortex roll-up test case to simulate cases when operators cannot be merged into one DM (e.g., a non-linear PDE).

By splitting the DM, the singularities at the poles ($1/\cos\theta \rightarrow \infty$ as $\theta \rightarrow \pm\frac{\pi}{2}$) in (5.3) remain. However, in this case, the approach functions without amplification of errors because the MD node sets have nodes near, but not on, the poles. As noted in [32, 39], applying the entire spatial operator to the right hand side of Equation ?? generates a single DM that analytically removes the singularities at poles.

We will advect a C^1 cosine bell height-field given by

$$h = \begin{cases} \frac{h_0}{2}(1 + \cos(\frac{\pi\rho}{R})) & \rho \leq R \\ 0 & \rho \geq R \end{cases}$$

having a maximum height of $h_0 = 1$, a radius $R = \frac{1}{3}$ and centered at $(\lambda_c, \theta_c) = (\frac{3\pi}{2}, 0)$, with $\rho = \arccos(\sin\theta_c \sin\theta + \cos\theta_c \cos\theta \cos(\lambda - \lambda_c))$. The angle of rotation, $\alpha = \frac{\pi}{2}$, is chosen to transport the bell over the poles of the coordinate system.

Table 5.2: Values for hyperviscosity and RBF shape parameter for the cosine bell test.

	$\epsilon = c_1\sqrt{N} - c_2$		$H = -\gamma_c N^{-k} \Delta^k$	
Stencil Size (n)	c_1	c_2	k	γ_c
17	0.026	0.08	2	$8 * 10^{-4}$
31	0.035	0.1	4	$5 * 10^{-2}$
50	0.044	0.14	6	$5 * 10^{-1}$
101	0.058	0.16	8	$5 * 10^{-2}$

Figure 5.4 compares eigenvalues of the DM for $N = 4096$ nodes and stencil size $n = 101$ before and after hyperviscosity is applied. To avoid scaling effects of velocity on the eigenvalues, they have been scaled by $1/u_0$. The same approach as in the vortex roll-up case is used to determine the parameters for hyperviscosity and ϵ . Our tuned parameters are presented in Table 5.2.

Figure 5.5 shows the cosine bell transported ten full revolutions around the sphere. Without hyperviscosity, RBF-FD cannot complete a single revolution of the bell before instability takes over. However, adding hyperviscosity allows computation to extend to dozens or even thousands of revolutions and maintain stability (e.g., see [39]). After ten revolutions, the cosine bell is still intact. The majority of the absolute error (Figure 5.5b) appears at the base of the C^1 bell where the discontinuity appears in the derivative. At ten revolutions, Figure 5.6 illustrates the convergence of the RBF-FD method. All tests in Figure 5.6 assume 1000 time-steps per revolution (i.e., $\Delta t = 1036.8$ seconds).

Complete: 17.28 minutes was a conservative step that allowed the problem to scale up to $N = 27556$ nodes. Compare this to the conservative 30 minute time-step taken for $N = 4096$ nodes in [32], which was already half necessary for DG and 8x less than necessary for both Spherical Harmonics and Double Fourier methods. **Author's Note:** [It would be good](#)

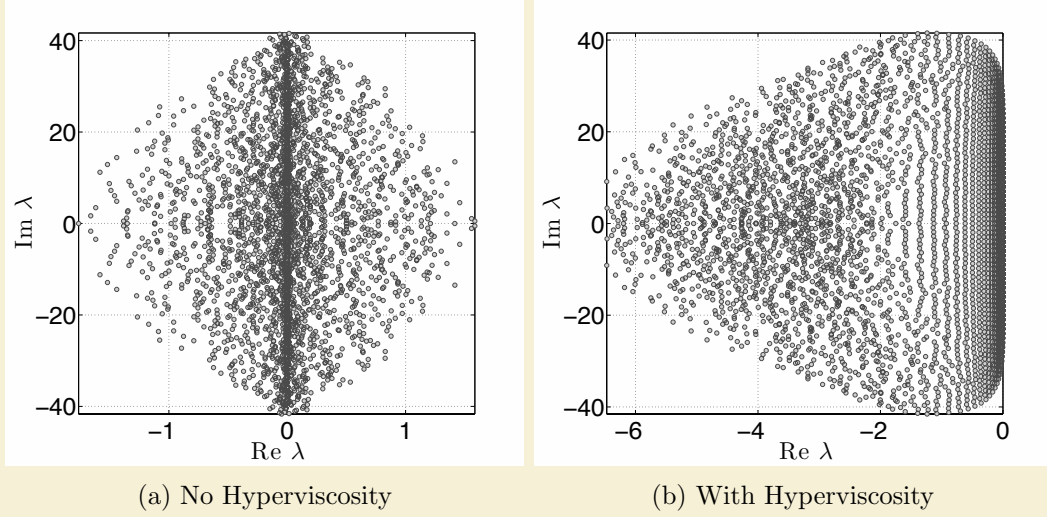


Figure 5.4: Eigenvalues of (5.4) for the cosine bell test case with $N = 4096$ nodes, stencil size $n = 101$, and $\epsilon = 3.5$. Left: no hyperviscosity. Right: hyperviscosity enabled with $k = 8$ and $\gamma_c = 5 * 10^{-2}$. Eigenvalues are divided by u_0 to remove scaling effects of velocity.

Author's Note: [color](#)

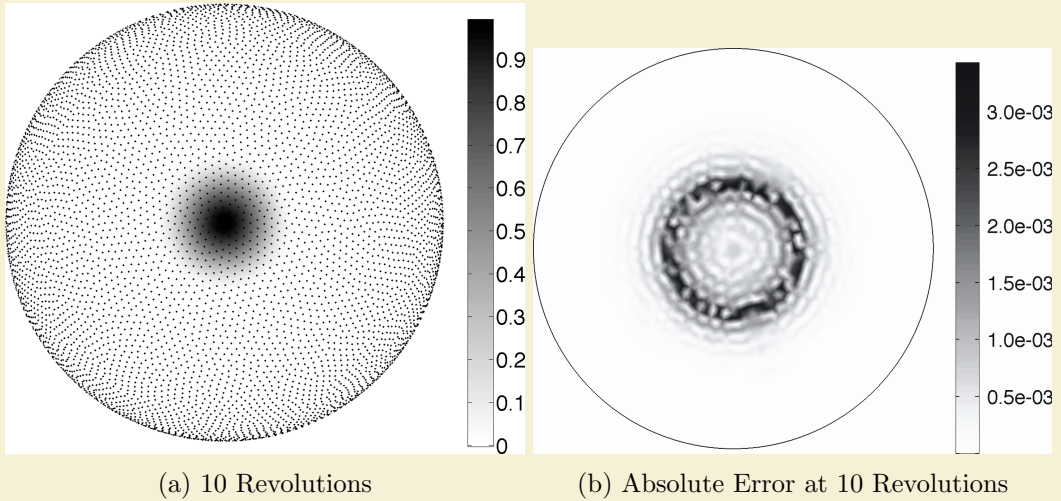


Figure 5.5: Cosine bell solution after 10 revolutions with $N = 10201$ nodes and stencil size $n = 101$. Hyperviscosity parameters are $k = 8$, $\gamma_c = 5(10^{-2})$.

Author's Note: [Insert color figures](#)

[to quantify the appropriate \$dt\$ that would compare RBF-FD to their \$N = 4096\$ case with global RBFs.](#)

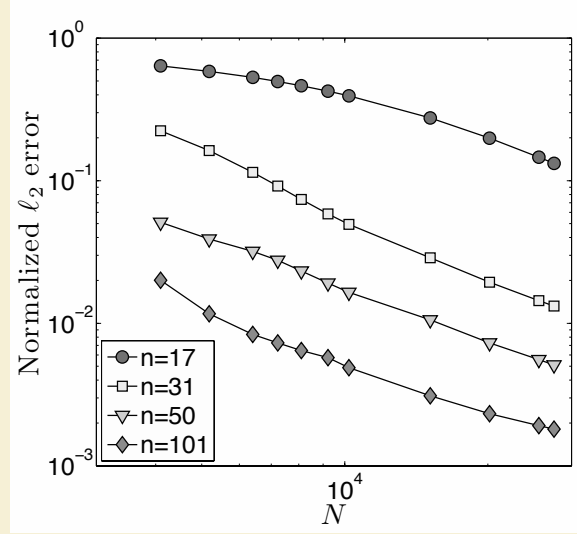


Figure 5.6: Convergence plot for cosine bell advection. Normalized ℓ_2 error at 10 revolutions with hyperviscosity enabled.

5.1 Fragments (integrate above)

To verify our multi-CPU and multi-CPU+GPU implementations, two hyperbolic PDEs on the surface of the sphere are tested. For both cases a spherical coordinate system is used in terms of latitude λ and longitude θ :

$$\begin{aligned} x &= \rho \cos \lambda \cos \theta, \\ y &= \rho \sin \lambda \cos \theta, \\ z &= \rho \sin \theta. \end{aligned}$$

Node sets are the Maximum Determinant point distributions on the sphere [81] consistent with previously published results (see e.g., [?] and [40]).

Hyperviscosity parameters γ_c and k depend on the RHS of the PDE. For this test case, hyperviscosity scaling parameters are listed in Table 5.1. Linear functions to choose the RBF support parameter ϵ are also provided. The parameters γ_c and k were obtained via trial-and-error parameter searching on $N = 4096$ nodes. The goal when choosing parameters is to push all eigenvalues to the left half-plane, and then tweak γ_c up or down to condense the eigenvalues as near to the imaginary axis as possible. We try to keep the range of filtered eigenvalue real parts within twice the width of the unfiltered range, so hyperviscosity does not cause too much diffusion in the solution.

For the cosine bell we use the initial conditions

$$h = \begin{cases} \frac{h_0}{2}(1 + \cos(\frac{\pi\rho}{R})) & \rho \leq R \\ 0 & \rho \geq R \end{cases}$$

where the bell of radius $R = \frac{a}{3}$ is centered at (λ_c, θ_c) and provided by the expression,

$$\rho = a \arccos(\sin \theta_c \sin \theta + \cos \theta_c \cos \theta \cos(\lambda - \lambda_c)).$$

We assume $a = 1$, $h_0 = 1$, and $(\lambda_c, \theta_c) = (3\pi/2, 0)$. The angle $\alpha = \pi/2$ is chosen to transport the bell over the poles of the coordinate system, and $u_0 = 2\pi a / 1036800$.

[Author's Note: State that we can split operator to test cases like nonlinear PDEs.](#)

[Author's Note: Include figures from NCL or Paraview](#)

5.1.1 CFL

We constrict our timesteps according to the Courant-Friedrich-Lowy (CFL) condition:

$$C_{\max} \frac{\Delta x_{\min}}{v_{\max}} < \Delta t$$

where Δx_{\min} is the minimum distance between any two nodes in the domain, and the v_{\max} is the maximum velocity

For the cosine bell test cases we use a conservative $C_{\max} = 0.4$ to ensure stable transport in all cases with $n = 101$. However, in testing it was found that $n = 17$ is capable of stably advecting with $C_{\max} > 1$ for $n = 17$; $n = 101$ can go up to $C_{\max} = 0.51$ for $N = 27556$ (e.g. 650 timesteps per revolution).

apparently, canceling the cosine analytically causes the conditioning of the system to change slightly. The hyperviscosity parameters I have in the paper are for the case with the cosine present. The parameters continue to function well for the other cases, but their impact on the eigenvalue distributions is noticeably higher (further span to the left).

BIBLIOGRAPHY

- [1] Kdtreesearcher class. MATLAB R2013a Documentation (<http://www.mathworks.com/help/stats/kdtreesearcherclass.html>), Aug 2013. 42, 53
- [2] AccelerEyes. *Jacket User Guide - The GPU Engine for MATLAB*, 1.2.1 edition, November 2009. 5, 6
- [3] E. Anderson, Z. Bai, C. Bischof, S. Blackford, J. Demmel, J. Dongarra, J. Du Croz, A. Greenbaum, S. Hammarling, A. McKenney, and D. Sorensen. *LAPACK Users' Guide*. Society for Industrial and Applied Mathematics, Philadelphia, PA, third edition, 1999. 6, 29
- [4] Sylvie Barak. Gpu technology key to exascale says nvidia. <http://www.eetimes.com/electronics-news/4230659/GPU-technology-key-to-exascale-says-Nvidia>, November 2011. 3, 5
- [5] R. K. Beatson, W. A. Light, and S. Billings. Fast Solution of the Radial Basis Function Interpolation Equations: Domain Decomposition Methods. *SIAM J. Sci. Comput.*, 22(5):1717–1740, 2000. 4
- [6] E. F. Bollig. Sphere grids. https://github.com/bollig/sphere_grids, Aug 2012. 37
- [7] Evan F. Bollig, Natasha Flyer, and Gordon Erlebacher. Solution to PDEs using radial basis function finite-differences (rbf-fd) on multiple GPUs. *Journal of Computational Physics*, 231(21):7133 – 7151, 2012. 34, 54
- [8] Andreas Brandstetter and Alessandro Artusi. Radial Basis Function Networks GPU Based Implementation. *IEEE Transaction on Neural Network*, 19(12):2150–2161, December 2008. 5
- [9] J. C. Carr, R. K. Beatson, J. B. Cherrie, T. J. Mitchell, W. R. Fright, B. C. McCallum, and T. R. Evans. Reconstruction and Representation of 3D Objects with Radial Basis Functions. In *SIGGRAPH '01: Proceedings of the 28th annual conference on Computer graphics and interactive techniques*, pages 67–76, New York, NY, USA, 2001. ACM. 18
- [10] J. C. Carr, R. K. Beatson, B. C. McCallum, W. R. Fright, T. J. McLennan, and T. J. Mitchell. Smooth Surface Reconstruction from Noisy Range Data. In *GRAPHITE '03: Proceedings of the 1st international conference on Computer graphics and interactive*

techniques in Australasia and South East Asia, pages 119–ff, New York, NY, USA, 2003. ACM. 5, 18

- [11] Tom Cecil, Jianliang Qian, and Stanley Osher. Numerical Methods for High Dimensional Hamilton-Jacobi Equations Using Radial Basis Functions. *JOURNAL OF COMPUTATIONAL PHYSICS*, 196:327–347, 2004. 3, 15, 26, 28
- [12] G Chandhini and Y Sanyasiraju. Local RBF-FD Solutions for Steady Convection-Diffusion Problems. *International Journal for Numerical Methods in Engineering*, 72(3), 2007. 1, 15, 28
- [13] P P Chinchapatnam, K Djidjeli, P B Nair, and M Tan. A compact RBF-FD based meshless method for the incompressible Navier–Stokes equations. *Proceedings of the Institution of Mechanical Engineers, Part M: Journal of Engineering for the Maritime Environment*, 223(3):275–290, March 2009. 28
- [14] Michael Connor and Piyush Kumar. Fast construction of k-nearest neighbor graphs for point clouds. *IEEE Transactions on Visualization and Computer Graphics*, 16:599–608, 2010. 54
- [15] CD Correa, D Silver, and M Chen. Volume Deformation via Scattered Data Interpolation. *Proceedings of Eurographics/IEEE VGTC Workshop on Volume Graphics*, pages 91–98, 2007. 16
- [16] A Corrigan and HQ Dinh. Computing and Rendering Implicit Surfaces Composed of Radial Basis Functions on the GPU. *International Workshop on Volume Graphics*, 2005. 5
- [17] N Cuntz, M Leidl, TU Darmstadt, GA Kolb, CR Salama, M Böttinger, D Klimarechenzentrum, and G Hamburg. GPU-based Dynamic Flow Visualization for Climate Research Applications. *Proc. SimVis*, pages 371–384, 2007. 5
- [18] Salvatore Cuomo, Ardelio Galletti, Giulio Giuntay, and Alfredo Starace. Surface reconstruction from scattered point via rbf interpolation on gpu. *CoRR*, abs/1305.5179, 2013. 6
- [19] Oleg Davydov and Dang Thi Oanh. On the optimal shape parameter for gaussian radial basis function finite difference approximation of the poisson equation. *Computers Mathematics with Applications*, 62(5):2143 – 2161, 2011. 15, 28, 40
- [20] Mark de Berg, Otfried Cheong, Marc van Kreveld, and Mark Overmars. *Computational Geometry: Algorithms and Applications*. Springer-Verlag, 3rd edition, 2008. 44, 45
- [21] E Divo and AJ Kassab. An Efficient Localized Radial Basis Function Meshless Method for Fluid Flow and Conjugate Heat Transfer. *Journal of Heat Transfer*, 129:124, 2007. 4, 15, 16, 22
- [22] Qiang Du, Vance Faber, and Max Gunzburger. Centroidal Voronoi Tessellations: Applications and Algorithms. *SIAM Rev.*, 41(4):637–676, 1999. 1

- [23] Qiang Du, Max D. Gunzburger, and Lili Ju. Voronoi-based Finite Volume Methods, Optimal Voronoi Meshes, and PDEs on the Sphere. *Computer Methods in Applied Mechanics and Engineering*, 192:3933–3957, August 2003. [38](#), [39](#)
- [24] G. E. Fasshauer. RBF Collocation Methods and Pseudospectral Methods. Technical report, 2006. [10](#), [14](#), [15](#), [21](#)
- [25] Gregory E. Fasshauer. Solving Partial Differential Equations by Collocation with Radial Basis Functions. In *In: Surface Fitting and Multiresolution Methods A. Le M'ehaut'e, C. Rabut and L.L. Schumaker (eds.)*, Vanderbilt, pages 131–138. University Press, 1997. [13](#), [14](#), [15](#), [20](#)
- [26] Gregory E. Fasshauer. *Meshfree Approximation Methods with MATLAB*, volume 6 of *Interdisciplinary Mathematical Sciences*. World Scientific Publishing Co. Pte. Ltd., 5 Toh Tuck Link, Singapore 596224, 2007. [vii](#), [1](#), [9](#), [10](#), [11](#), [14](#), [15](#), [16](#), [17](#), [19](#), [21](#), [28](#), [32](#), [43](#), [45](#)
- [27] Gregory E. Fasshauer and Jack G. Zhang. On choosing “optimal” shape parameters for rbf approximation. *Numerical Algorithms*, 45(1-4):345–368, 2007. [14](#)
- [28] A. I. Fedoseyev, M. J. Friedman, and E. J. Kansa. Improved Multiquadric Method for Elliptic Partial Differential Equations via PDE Collocation on the Boundary. *Computers & Mathematics with Applications*, 43(3-5):439 – 455, 2002. [13](#), [14](#), [15](#), [21](#)
- [29] Natasha Flyer and Bengt Fornberg. Radial basis functions: Developments and applications to planetary scale flows. *Computers & Fluids*, 46(1):23–32, July 2011. [2](#), [9](#), [14](#), [15](#)
- [30] Natasha Flyer and Erik Lehto. Rotational transport on a sphere: Local node refinement with radial basis functions. *Journal of Computational Physics*, 229(6):1954–1969, March 2010. [2](#), [9](#), [15](#), [42](#), [51](#), [62](#)
- [31] Natasha Flyer, Erik Lehto, Sebastien Blaise, Grady B. Wright, and Amik St-Cyr. Rbf-generated finite differences for nonlinear transport on a sphere: shallow water simulations. *Submitted to Elsevier*, pages 1–29, 2011. [15](#), [27](#), [28](#), [33](#), [34](#), [35](#), [39](#), [40](#), [42](#), [43](#), [45](#), [63](#)
- [32] Natasha Flyer and Grady B. Wright. Transport schemes on a sphere using radial basis functions. *Journal of Computational Physics*, 226(1):1059 – 1084, 2007. [2](#), [9](#), [14](#), [15](#), [28](#), [42](#), [62](#), [64](#), [66](#)
- [33] Natasha Flyer and Grady B. Wright. A Radial Basis Function Method for the Shallow Water Equations on a Sphere. In *Proc. R. Soc. A*, volume 465, pages 1949–1976, December 2009. [2](#), [9](#), [14](#), [15](#), [33](#), [42](#)
- [34] B Fornberg, T Driscoll, G Wright, and R Charles. Observations on the behavior of radial basis function approximations near boundaries. *Computers & Mathematics with Applications*, 43(3-5):473–490, February 2002. [27](#)

- [35] B Fornberg, N Flyer, and JM Russell. Comparisons Between Pseudospectral and Radial Basis Function Derivative Approximations. *IMA Journal of Numerical Analysis*, 2009. [37](#)
- [36] B. Fornberg and G. Wright. Stable computation of multiquadric interpolants for all values of the shape parameter. *Computers & Mathematics with Applications*, 48(5-6):853 – 867, 2004. [9](#), [11](#), [15](#), [23](#)
- [37] Bengt Fornberg and Natasha Flyer. Accuracy of Radial Basis Function Interpolation and Derivative Approximations on 1-D Infinite Grids. *Adv. Comput. Math.*, 23:5–20, 2005. [10](#)
- [38] Bengt Fornberg, Elisabeth Larsson, and Natasha Flyer. Stable Computations with Gaussian Radial Basis Functions. *SIAM J. on Scientific Computing*, 33(2):869—892, 2011. [9](#), [11](#), [15](#), [23](#), [28](#), [40](#), [62](#)
- [39] Bengt Fornberg and Erik Lehto. Stabilization of RBF-generated finite difference methods for convective PDEs. *Journal of Computational Physics*, 230(6):2270–2285, March 2011. [3](#), [11](#), [15](#), [26](#), [27](#), [28](#), [34](#), [35](#), [37](#), [43](#), [45](#), [62](#), [66](#)
- [40] Bengt Fornberg and Erik Lehto. Stabilization of rbf-generated finite difference methods for convective pdes. *J. Comput. Physics*, 230(6):2270–2285, 2011. [68](#)
- [41] Bengt Fornberg, Erik Lehto, and Collin Powell. Stable calculation of gaussian-based rbf-fd stencils. Technical Report 2012-018, Uppsala University, Numerical Analysis, 2012. [23](#), [24](#), [28](#), [40](#)
- [42] Bengt Fornberg and Cécile Piret. A Stable Algorithm for Flat Radial Basis Functions on a Sphere. *SIAM Journal on Scientific Computing*, 30(1):60–80, 2007. [9](#), [11](#), [23](#), [37](#), [40](#)
- [43] Bengt Fornberg and Cécile Piret. On Choosing a Radial Basis Function and a Shape Parameter when Solving a Convective PDE on a Sphere. *Journal of Computational Physics*, 227(5):2758 – 2780, 2008. [vii](#), [9](#), [11](#), [15](#), [62](#)
- [44] Richard Franke. Scattered Data Interpolation: Tests of Some Method. *Mathematics of Computation*, 38(157):181–200, 1982. [11](#), [15](#)
- [45] Jerome H. Friedman, Jon Louis Bentley, and Raphael Ari Finkel. An algorithm for finding best matches in logarithmic expected time. *ACM Trans. Math. Softw.*, 3(3):209–226, September 1977. [45](#)
- [46] Prashant Goswami, Philipp Schlegel, Barbara Solenthaler, and Renato Pajarola. Interactive sph simulation and rendering on the gpu. In *Proceedings of the 2010 ACM SIGGRAPH/Eurographics Symposium on Computer Animation*, SCA ’10, pages 55–64, Aire-la-Ville, Switzerland, 2010. Eurographics Association. [54](#)
- [47] S. Green. Cuda particles. NVidia Whitepaper, 2010. [43](#), [47](#), [48](#)

- [48] N. A. Gumerov, R. Duraiswami, and E. A. Borovikov. Data structures, optimal choice of parameters, and complexity results for generalized multilevel fast multipole methods in d dimensions. Technical Report UMIACS-TR-2003-28, University of Maryland (College Park, Md.), Apr 2003. 43
- [49] R Hardy. Multiquadric Equations of Topography and Other Irregular Surfaces. *J. Geophysical Research*, (76):1–905, 1971. 2, 9, 11
- [50] Y. C. Hon and R. Schaback. On unsymmetric collocation by radial basis functions. *Appl. Math. Comput.*, 119(2-3):177–186, 2001. 13, 14, 15, 17
- [51] Yiu-Chung Hon, Kwok Fai Cheung, Xian-Zhong Mao, and Edward J. Kansa. A Multiquadric Solution for the Shallow Water Equations. *ASCE J. Hydraulic Engineering*, 125:524–533, 1999. 14, 15
- [52] A. Iske. *Multiresolution Methods in Scattered Data Modeling*. Springer, 2004. 9, 10, 11, 16, 17
- [53] R. Jakob-Chien, J.J. Hack, and D.L. Williamson. Spectral transform solutions to the shallow water test set. *Journal of Computational Physics*, 119(1):164–187, 1995. 62
- [54] I. Johnson. Real-time particle systems in the blender game engine. Master’s thesis, Florida State University, November 2011. 43, 48
- [55] E J Kansa. Multiquadratics—A scattered data approximation scheme with applications to computational fluid-dynamics. I. Surface approximations and partial derivative estimates. *Computers Math. Applic.*, (19):127–145, 1990. 2, 9, 12, 13, 15, 19
- [56] E J Kansa. Multiquadratics—A scattered data approximation scheme with applications to computational fluid-dynamics. II. Solutions to parabolic, hyperbolic and elliptic partial differential equations. *Computers Math. Applic.*, (19):147–161, 1990. 2, 9, 12, 13, 15, 19
- [57] G Kosec and B Šarler. Solution of thermo-fluid problems by collocation with local pressure correction. *International Journal of Numerical Methods for Heat & Fluid Flow*, 18, 2008. 4, 15, 16
- [58] Øystein E. Krog. GPU-based Real-Time Snow Avalanche Simulations. Master’s thesis, Norwegian University of Science and Technology, June 2010. 43, 47, 48, 52, 53
- [59] Elisabeth Larsson and Bengt Fornberg. A Numerical Study of some Radial Basis Function based Solution Methods for Elliptic PDEs. *Comput. Math. Appl.*, 46:891–902, 2003. 9, 11, 13, 14, 15, 20, 21, 23
- [60] Shaofan Li and Wing K. Liu. *Meshfree Particle Methods*. Springer Publishing Company, Incorporated, 2007. 1, 2
- [61] Yuxu Lin, Chun Chen, Mingli Song, and Zicheng Liu. Dual-RBF based surface reconstruction. *Vis Comput*, 25(5-7):599–607, May 2009. 16

- [62] Wai-Hung Liu and Andrew H. Sherman. Comparative analysis of the cuthill-mckee and the reverse cuthill-mckee ordering algorithms for sparse matrices. *SIAM Journal on Numerical Analysis*, 13(2):pp. 198–213, Apr 1976. [55](#)
- [63] X. Liu, G.R. Liu, K. Tai, and K.Y. Lam. Radial point interpolation collocation method (RPICM) for partial differential equations. *Computers & Mathematics with Applications*, 50(8-9):1425 – 1442, 2005. [15](#), [16](#)
- [64] John Mellor-crummey, David Whalley, and Ken Kennedy. Improving memory hierarchy performance for irregular applications using data and computation reorderings. In *International Journal of Parallel Programming*, pages 425–433, 2001. [53](#)
- [65] Bryan S. Morse, Terry S. Yoo, Penny Rheingans, David T. Chen, and K. R. Subramanian. Interpolating implicit surfaces from scattered surface data using compactly supported radial basis functions. In *ACM SIGGRAPH 2005 Courses*, SIGGRAPH '05, New York, NY, USA, 2005. ACM. [14](#), [15](#)
- [66] C.T. Mouat and R.K. Beatson. RBF Collocation. Technical Report UCDMS2002/3, Department of Mathematics & Statistics, University of Canterbury, New Zealand, February 2002. [15](#), [16](#), [19](#)
- [67] Ramachandran D. Nair and Christiane Jablonowski. Moving Vortices on the Sphere: A Test Case for Horizontal Advection Problems. *Monthly Weather Review*, 136(2):699–711, February 2008. [62](#)
- [68] R.D. Nair, S.J. Thomas, and R.D. Loft. A discontinuous Galerkin transport scheme on the cubed sphere. *Monthly Weather Review*, 133(4):814–828, April 2005. [62](#), [64](#)
- [69] Jia Pan and Dinesh Manocha. Fast GPU-based Locality Sensitive Hashing for K-Nearest Neighbor Computation. *Proceedings of the 19th ACM SIGSPATIAL GIS '11*, 2011. [54](#)
- [70] Timothy J. Purcell, Craig Donner, Mike Cammarano, Henrik Wann Jensen, and Pat Hanrahan. Photon mapping on programmable graphics hardware. In *Proceedings of the ACM SIGGRAPH/EUROGRAPHICS Conference on Graphics Hardware*, pages 41–50. Eurographics Association, 2003. [52](#)
- [71] DA Randall, TD Ringler, and RP Heikes. Climate modeling with spherical geodesic grids. *Computing in Science & Engineering*, pages 32–41, 2002. [37](#)
- [72] Yousef Saad. *Iterative Methods for Sparse Linear Systems*. Society for Industrial Mathematics, second edition, 2003. [60](#)
- [73] Hanan Samet. *Foundations of Multidimensional and Metric Data Structures (The Morgan Kaufmann Series in Computer Graphics and Geometric Modeling)*. Morgan Kaufmann Publishers Inc., San Francisco, CA, USA, 2005. [43](#), [44](#), [45](#), [47](#), [49](#), [52](#), [53](#)
- [74] C. Sanderson. Armadillo: An open source c++ linear algebra library for fast prototyping and computationally intensive experiments. Technical report, NICTA, 2010. [62](#)

- [75] Robert Schaback. Multivariate Interpolation and Approximation by Translates of a Basis Function. In C.K. Chui and L.L. Schumaker, editors, *Approximation Theory VIII–Vol. 1: Approximation and Interpolation*, pages 491–514. World Scientific Publishing Co., Inc, 1995. 9, 11, 23
- [76] J. Schmidt, C. Piret, B.J. Kadlec, D.A. Yuen, E. Sevre, N. Zhang, and Y. Liu. Simulating Tsunami Shallow-Water Equations with Graphics Accelerated Hardware (GPU) and Radial Basis Functions (RBF). In *South China Sea Tsunami Workshop*, 2008. 6
- [77] J. Schmidt, C. Piret, N. Zhang, B.J. Kadlec, D.A. Yuen, Y. Liu, G.B. Wright, and E. Sevre. Modeling of Tsunami Waves and Atmospheric Swirling Flows with Graphics Processing Unit (GPU) and Radial Basis Functions (RBF). *Concurrency and Computat.: Pract. Exper.*, 2009. 5, 6, 15
- [78] C. Shu, H. Ding, and K. S. Yeo. Local radial basis function-based differential quadrature method and its application to solve two-dimensional incompressible Navier-Stokes equations. *Computer Methods in Applied Mechanics and Engineering*, 192(7-8):941 – 954, 2003. 3, 15, 26, 28
- [79] C Shu, H Ding, and N Zhao. Numerical Comparison of Least Square-Based Finite-Difference (LSFD) and Radial Basis Function-Based Finite-Difference (RBFFD) Methods. *Computers and Mathematics with Applications*, 51(8):1297–1310, 2006. 15, 28
- [80] Steven Skiena. *The Algorithm Design Manual (2. ed.)*. Springer, 2008. 43, 44
- [81] Ian H. Sloan and Robert S. Womersley. Extremal systems of points and numerical integration on the sphere. *Adv. Comput. Math*, 21:107–125, 2003. 37, 62, 68
- [82] D Stevens, H Power, M Lees, and H Morvan. The use of PDE centres in the local RBF Hermitian method for 3D convective-diffusion problems. *Journal of Computational Physics*, 2009. 14, 15, 16, 22, 28
- [83] David Stevens, Henry Power, Michael Lees, and Herve Morvan. A Meshless Solution Technique for the Solution of 3D Unsaturated Zone Problems, Based on Local Hermitian Interpolation with Radial Basis Functions. *Transp Porous Med*, 79(2):149–169, Sep 2008. 15, 16, 22
- [84] David Stevens, Henry Power, and Herve Morvan. An order-N complexity meshless algorithm for transport-type PDEs, based on local Hermitian interpolation. *Engineering Analysis with Boundary Elements*, 33(4):425 – 441, 2008. 4, 15, 16, 22
- [85] Andrea Tagliasacchi. kd-tree for matlab. <http://www.mathworks.com/matlabcentral/fileexchange/21512-kd-tree-for-matlab>, Sep 2010. 42, 43, 53
- [86] Andrea Tagliasacchi. kd-tree matlab. <https://code.google.com/p/kdtree-matlab>, Jun 2012. 45, 53

- [87] A. I. Tolstykh and D. A. Shirobokov. On using radial basis functions in a “finite difference mode” with applications to elasticity problems. In *Computational Mechanics*, volume 33, pages 68 – 79. Springer, December 2003. [3](#), [26](#)
- [88] A.I. Tolstykh. On using RBF-based differencing formulas for unstructured and mixed structured-unstructured grid calculations. In *Proceedings of the 16 IMACS World Congress, Lausanne*, pages 1–6, 2000. [3](#), [26](#)
- [89] Robert Vertnik and Božidar Šarler. Meshless local radial basis function collocation method for convective-diffusive solid-liquid phase change problems. *International Journal of Numerical Methods for Heat & Fluid Flow*, 16(5):617–640, 2006. [15](#), [16](#), [22](#)
- [90] B. Šarler and R. Vertnik. Meshfree Explicit Local Radial Basis Function Collocation Method for Diffusion Problems. *Computers and Mathematics with Applications*, 51(8):1269–1282, 2006. [15](#), [16](#), [22](#)
- [91] J. G. Wang and G. R. Liu. A point interpolation meshless method based on radial basis functions. *Int. J. Numer. Methods Eng.*, 54, 2002. [15](#), [16](#)
- [92] M Weiler, R Botchen, S Stegmaier, T Ertl, J Huang, Y Jang, DS Ebert, and KP Gaither. Hardware-Assisted Feature Analysis and Visualization of Procedurally Encoded Multifield Volumetric Data. *IEEE Computer Graphics and Applications*, 25(5):72–81, 2005. [5](#)
- [93] Holger Wendland. Fast evaluation of radial basis functions: Methods based on partition of unity. In *Approximation Theory X: Wavelets, Splines, and Applications*, pages 473–483. Vanderbilt University Press, 2002. [43](#), [47](#), [48](#), [52](#)
- [94] Holger Wendland. *Scattered Data Approximation*. Cambridge Monographs on Applied and Computational Mathematics. Cambridge University Press, 2005. [42](#), [43](#), [47](#), [48](#), [52](#), [53](#)
- [95] Geoffrey Womeldorf. Spherical Centroidal Voronoi Tessellations: Point Generation and Density Functions Via Images. Master’s thesis, Florida State University, 2008. [38](#), [39](#)
- [96] R. Womersley. Extremal (maximum determinant) points on the sphere S^2 . <http://web.maths.unsw.edu.au/~rsw/Sphere/Extremal/New/index.html>, Oct 2007. [37](#)
- [97] Robert S. Womersley and Ian H Sloan. How good can polynomial interpolation on the sphere be?, 2001. [37](#)
- [98] Grady Wright and Bengt Fornberg. Scattered node mehrstellenverfahren-type formulas generated from radial basis functions. In *The International Conference on Computational Methods*, December 15-17 2004. [15](#), [28](#)
- [99] Grady B. Wright. *Radial Basis Function Interpolation: Numerical and Analytical Developments*. PhD thesis, University of Colorado, 2003. [3](#), [15](#), [26](#), [28](#), [40](#)

- [100] Grady B. Wright, Natasha Flyer, and David A. Yuen. A hybrid radial basis function–pseudospectral method for thermal convection in a 3-d spherical shell. *Geochim. Geophys. Geosyst.*, 11(Q07003):18 pp., 2010. [2](#), [9](#), [15](#), [21](#), [33](#)
- [101] Grady B. Wright and Bengt Fornberg. Scattered node compact finite difference-type formulas generated from radial basis functions. *J. Comput. Phys.*, 212(1):99–123, 2006. [15](#), [16](#), [27](#)
- [102] Z M Wu. Hermite-Birkhoff interpolation of scattered data by radial basis functions. *Approx. Theory Appl.*, (8):1–10, 1992. [13](#)
- [103] Xuan Yang, Zhixiong Zhang, and Ping Zhou. Local Elastic Registration of Multimodal Medical Image Using Robust Point Matching and Compact Support RBF. In *BMEI '08: Proceedings of the 2008 International Conference on BioMedical Engineering and Informatics*, pages 113–117, Washington, DC, USA, 2008. IEEE Computer Society. [16](#)
- [104] Lexing Ying. A kernel independent fast multipole algorithm for radial basis functions. *Journal of Computational Physics*, 213(2):451 – 457, 2006. [43](#), [44](#)
- [105] Rio Yokota, L.A. Barba, and Matthew G. Knepley. PetRBF — A parallel O(N) algorithm for radial basis function interpolation with Gaussians. *Computer Methods in Applied Mechanics and Engineering*, 199(25-28):1793–1804, May 2010. [4](#), [6](#)
- [106] Hao Zhang and Marc G. Genton. Compactly supported radial basis function kernels, 2004. [15](#)

BIOGRAPHICAL SKETCH

Evan Bollig was born on the 6th of June, 1983, and grew up in the sleepy town of Sun Prairie, Wisconsin. He completed his Bachelor studies at the University of Minnesota–Twin Cities in 2006 with dual degrees in Computer Science and German Studies. In 2009, Evan earned a Master’s in Computational Science from the Department of Scientific Computing at Florida State University.

Evan currently lives in Saint Paul, Minnesota, and works as a consultant at the Minnesota Supercomputing Institute.